Numerical Simulations of Radiation and Heating from Non-thermal Electrons in Solar Flares

Jennifer A. Pollock

Presented for the degree of
Doctor of Philosophy
The University of Glasgow
2008

This thesis is my own composition except where indicated in the text.

March 5, 2008

Acknowledgements

First and foremost I would like to thank my supervisor, Dr. Lyndsay Fletcher, and my second supervisor, Dr. Declan Diver, for all their support, assistance and extensive knowledge over the three years. Secondly, I would like to acknowledge the support of the University of Glasgow Physical Sciences PhD Scholarship and the Department of Physics & Astronomy, which have funded my PhD.

I would also like to thank all my colleagues in Glasgow University Astronomy & Astrophysics Group (and colleagues at other institutions too), and of course the technical support staff of the department without whose assistance it would probably have taken a lot longer!

On a personal note, I would particularly like to thank Gordon Paton for listening even when he didn't understand and tolerating my work hours without complaint though he had a real job; Dr Ross Galloway for his much valued friendship, advice and extensive knowledge over the years; and my best friend Jennifer Toher for her constant friendship throughout uni, support and sympathetic ear when things weren't working, even though she prefers cosmology to solar! Thanks also to my family and all my other friends too.

Abstract

This thesis investigates heating and thermal and non-thermal X-ray emission from magnetic loops in active regions of the solar atmosphere using numerical simulations. The simulations also allow investigation of Type III radio emission. In our model we vary a number of physical parameters such as magnetic field configuration and density models, investigating the effect they have on emission and loop heating as a result of the propagation of a beam of fast electrons moving through the ambient coronal plasma.

Chapter 1 presents an overview of the Sun and the magnetic processes at work in the solar atmosphere. It also contains a summary of observations and current work corresponding to the phenomena discussed in later chapters, as well as current theories of particle acceleration and transport in an active region loop.

Chapter 2 describes the theory behind, and implementation of, the numerical simulations used, and initial tests of the accuracy of the simulations by comparing results with analytical results for simplified models. The simulations are built on a core which models the evolution of the electron distribution function through stochastic processes. We derive the Fokker-Plank equation from which we obtain the expressions describing the progress along a magnetic field of an electron undergoing Coulomb collisions with particles of a background plasma. We describe the field and density models used, and consider the effects of gradient and curvature drifts on particles.

In Chapter 3 we present results showing the non-thermal X-ray emission from magnetic loops with various density models and field configurations. We show results from a straightforward field model with no curvature as described in MacKinnon & Brown (1990), and then results from a more complex (and more realistic) X-point field model as described in Priest & Forbes (2000). These results illustrate the significant effects the field model and density of the background coronal plasma have on the loop emission, both in intensity and position (i.e. at which part of the loop the emission originates from). We also investigate the correlation

between loop footpoint size and X-ray intensity, theoretically verifying work done by Schmahl et al. (2006) in which they present observations showing that X-ray intensity increases with footpoint size.

In Chapter 4 we present results showing the evolution of the loop temperature profile over time. As the fast electrons collide with the particles of the ambient background plasma they lose energy, which is transferred to the plasma, increasing it's temperature. We include in these calculations the effects of radiative and conductive cooling of the loop, but we do not consider chromospheric evaporation (whereby heated plasma from the photosphere rises into the loop at the footpoints as a result of bombardment by the beam of fast electrons) or other bulk plasma effects. This would require a combination of stochastic and hydrodynamic simulations, which we do not cover in this work. Again, we show the effects of changing density and field models on the temperature profile.

In Chapter 5 we investigate the thermal X-ray emission from the particles of the background plasma in the heated loop. We then combine the thermal and non-thermal emission to produce X-ray spectra from photon energies 6 - 100 keV, similar to those observed by satellites such as the Reuven-Ramaty High Energy Solar Spectroscopic Imager (RHESSI), thus verifying that our simulations successfully model some of the processes present in active regions. We also consider the limitations of our simulations and models and discuss what parameters and changes would produce results close to observational data.

Chapter 6 is separate from the preceding chapters and is a brief study of the production of Reverse-Drift Type III radio bursts in a loop, specifically the position in the loop at which the condition for their development originates, given various plasma densities and particle injection profiles. In a beam of injected electrons, the faster (higher energy) electrons propagate along the loop more quickly than the slower particles, causing an instability to develop in the beam distribution. This instability leads to the growth of Langmuir waves, which in turn result in emission at radio wavelengths. We show the development of the condition leading to this emission from a loop as a function of time and position, with various field and density models and particle injection profiles.

Chapter 7 summarises the main body of work in this thesis and discusses possible further development of these methods in investigating the physical processes and parameters at work in active region magnetic loops.

Contents

Chapter 1

Introduction

1.1 Overview

Our star, the Sun, is a main sequence star of spectral type G2V. It has a radius of $\sim 7 \times 10^8$ m, a mass of $\sim 2 \times 10^{30}$ kg and a total luminosity of $\sim 3.8 \times 10^{26}$ W. The Sun generates energy through nuclear fusion (primarily hydrogen to helium via the proton-proton chain) in the core which is at a temperature of approximately 1.55×10^7 K . This energy is transferred outwards via radiation until the temperature gradient becomes too steep to support the plasma in static equilibrium and convection becomes the dominant transfer mechanism. Radiative heat transfer is far slower than convection in transferring energy from the core because of the "random-walk" nature of the movement of an emitted photon. A photon created at the core undergoes many absorptions and re-emissions and on average takes 10,000 years to reach the surface (Zirin (1988)). However, convection dominates after approximately 0.7 R_{sun} (Christensen-Dalsgaard et al. (1991)). In this region, the hot plasma of the interior is convected to the surface in many small, hot up-wellings, visible on the photosphere as a granulation pattern, in a process similar to that in boiling water. The bright centres of the granules (which are of the order 1000 km in width on average (Schwarzschild (1959))) contain upward flowing hot material from below the surface and the darker edges are material that has cooled and is flowing back down into the interior.

The photosphere is the visible surface of the Sun, below which the optical depth of the plasma is greater than one. It has a depth of approximately 100 km and a plasma number density of approximately 10^{16} - 10^{17} cm^{-3}. The temperature of the photosphere is approximately 5800 K, and is near black-body in form (Schmelz & Brown (1992), Zirin (1988)).

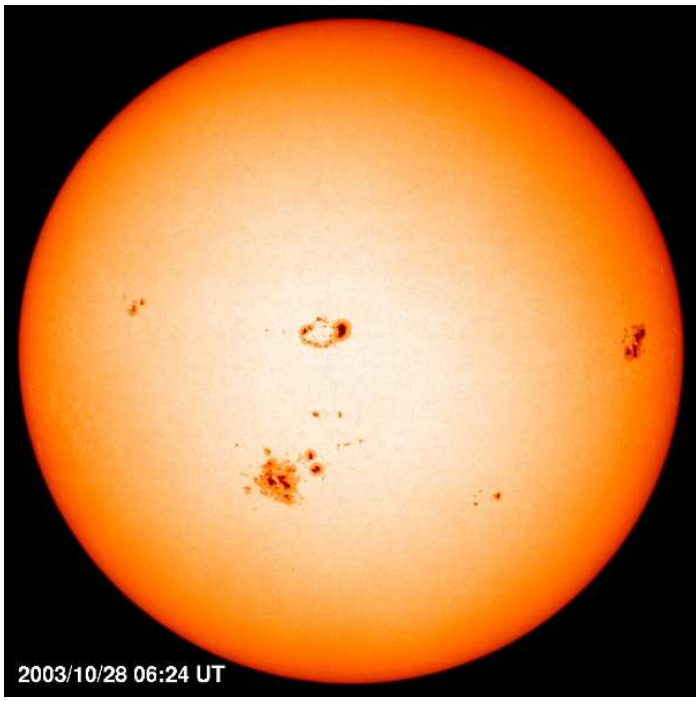

Figure 1.1: White light image of the Sun from the MDI instrument on the SOHO satellite, 28th Oct 2003. [SOHO (ESA & NASA)]

The solar magnetic field is believed to be caused by the differential rotation of the Sun and becomes highly distorted by this rotation, the rotation rate being faster at the equator than at the poles. This causes the field to become distorted around the equatorial regions, where it emerges in complex regions of loops and twisted field. These field lines and loops are anchored in the photosphere, and the field strength at the photosphere varies from $\sim$ 100 G in quiet regions, to $\sim$ 3000 G in active regions (Dulk & McLean (1978), Mathew et al. (2003)). Immediately above this is the chromosphere, which is $\sim$ 3000 km in depth. The density decreases across the chromosphere as a function of height, and the temperature increases gradually (after a slight dip) to reach $\sim$ 20,000 K at the base of the transition region (Fontenla et al. (1990)). The transition region is a very narrow region ($\sim$ 100 km wide) over which the temperature increases rapidly to several million Kelvin. Above this is the corona, the tenuous but extremely hot outer region of the solar atmosphere, visible in white light during solar eclipses as a halo of streamers and loops extending far beyond the surface of the Sun. The corona stretches as far as three solar radii from the Sun, and has temperatures of several

million Kelvin, and a number density of the order 10^9 cm^{-3} at a height of 5×10^8 cm above the photosphere (Gabriel (1976)). The mechanism of heat transfer to the corona which maintains these extreme temperatures is not yet understood, and is one of the most active areas of solar research.

The plasma beta (the ratio of the thermal to magnetic pressure) in the solar atmosphere is generally less than one (Gary (2001)), meaning the plasma must follow the path of the magnetic field. This allows us to observe the magnetic structure as the plasma contained by the magnetic loops is denser than the background plasma and emits radiation at various wavelengths, most prominently in extreme ultraviolet (Figure 1.2). This emission can been seen by orbiting telescopes, which provide excellent images of the magnetic structure in the solar atmosphere. Conversely, in the photosphere, the plasma beta is much greater than one and thus the magnetic field is constrained to follow the movement of the plasma (a situation known as "frozen-in field"). This means that the magnetic field, significantly the anchor points of magnetic loops, is distorted and pulled around by large- and small-scale motions of the plasma, causing the field to become twisted and distorted. This creates an increase in the magnetic tension, and if this becomes large enough, the field lines can reconfigure, releasing large amounts of matter and energy in the process. These events range from the smallest transient, short lived micro-flares, to the largest solar flare.

1.2 Observational Overview

Until relatively recently in history, it was only possible to observe the Sun in visible light, wavelengths detectable by the human eye. At these wavelengths, the disc of the Sun is relatively smooth, showing only sunspots as darker patches, and, when viewed through a telescope, much smaller scale granulation, likened to the speckled surface of an orange (Figure 1.1). Sunspots have been known and observed for millennia, the first systematic observations being made by Chinese astronomers as many as 4000 years ago. In more recent times, sunspots were regularly observed and studied by Galileo in the 1600s and daily observations were instigated in the mid 1700s at the Zurich Observatory. Observations of these continue today, and provide information on the long term evolution of the large scale solar magnetic field. Through sunspot observations it is known that the overall magnetic activity on the Sun waxes and wanes over an 11 year cycle in total, with the most recent maximum of activity occurring in the year 2000.

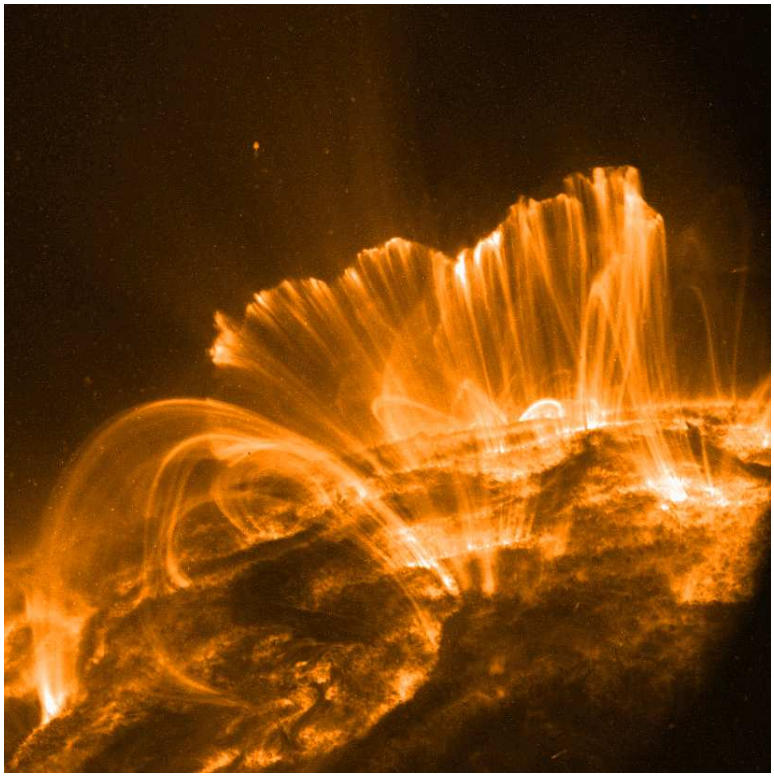

Figure 1.2: Hot coronal loop arcade as observed by the TRACE satellite at 171A on the 8th Nov 2000. [NASA / Stanford-Lockheed Institute for Space Research]

With the advance of time and technology, we are now able to observe emission from the Sun in other wavelengths across the electromagnetic spectrum. One of the first non-visible wavelengths to be detected was radio, when it was discovered that particularly strong solar flares (which had been first observed by Carrington, and independently by Hodgson (Carrington (1859))) caused interference in the early military radars of the mid-1940s (Hey et al. (1948)). Following this discovery, radio observations were regularly made and continue to this day, observing both the ambient radio emission from the quiet Sun and the large bursts produced during flare activity.

The advent of space-borne telescopes opened the window to new observational capabilities - without the absorption of our atmosphere to contend with, new wavelength ranges became detectable, including ultraviolet, X-ray and gamma ray wavelengths. Higher resolution optical images also became possible without the need to compensate for the distortion caused by the turbulent atmosphere.

Early X-ray emission had only been observable from high altitude balloons, with limited observation time, but with satellites such as the Japanese Yohkoh,

now inactive, (Ogawara et al. (1991), Masuda (2002)) and Hinode (Ichimoto & Solar-B Team (2005)), and the NASA satellite RHESSI (Reuven-Ramaty High Energy Solar Spectroscopic Imager) (Lin et al. (2002)), we are able to obtain detailed time and space resolved X-ray observations. The magnetic field strength on the surface of the Sun is measurable using the Zeeman splitting effect of absorption and emission lines, using instruments such as the Michaelson Doppler Imager on NASAs Solar and Heliospheric Observatory (SOHO) satellite (Domingo et al. (1995)). We are also able to infer the magnetic field structure in the solar atmosphere by examining extreme ultraviolet (EUV) emission with satellite such as Hinode and NASAs Transition Region and Coronal Explorer (TRACE) (Handy et al. (1999)), which provide us with high resolution images of magnetic loops as the heated plasma contained within them emits extreme ultraviolet radiation.

1.3 Solar Flares

Solar flares have been studied since they were first discovered by Carrington in 1859, both to further our understanding of the physics of the Sun, and to investigate the possible effects they may have on Earth. A solar flare is generally defined as a brightening across the full electromagnetic spectrum from an event on the Sun, and is often (but not always) accompanied by a coronal mass ejection (CME) whereby large quantities of matter are ejected from the Sun in a rapid expulsion.

Solar flares are labelled using the GOES (Geostationary Operational Environmental Satellites) classification system: A,B,C,M and X type, each class being 10 times stronger than the previous, from A to X. These are based on the peak soft X-ray flux as measured at Earth by NASAs GOES program. Each class is subdivided into further numerical classes, indicating multiples of that strength. For example, an X6 flare would have a peak soft X-ray flux of 6×10^{-4} Wm^{-2}. The largest flare yet observed (4th November 2003) was an X28 flare, which saturated the detectors, but it is believed it's true strength may have been as large as X40 (Brodrick et al. (2005)). Flares can release up to $\sim 10^{32}$ ergs of energy in the largest observed events (Emslie et al. (2005)). Different wavelengths of emission peak at different times, and originate from different areas of the flaring region (Figure 1.3). In the pre-flare phase, we may see a gradual increase in EUV and soft X-ray emission as the loops begin to heat. This is followed by the short-lived impulsive phase where we see sharp spikes in hard X-ray and microwave emission

Figure 1.3: Evolution of flare emission at various wavelengths. [Benz (2002), Figure 1.5]

as fast particles are accelerated onto the loops and propagate into the denser photosphere, the beginning of radio and Hα emission, and continued increase in EUV and soft X-rays and the loops continue to increase in temperature. There is then the main phase, where we see a peak in EUV and soft X-rays, and a continuing increase in Hα and metric radio, but there is no longer hard X-ray or microwave emission. The soft X-ray emission lags behind the hard X-ray emission because of the Neupert effect: as hard X-rays propagate into the denser chromosphere and photosphere, they heat plasma which moves up into the loop and emits soft X-ray radiation. The soft X-ray emission time integral has been observed to be closely related to the hard X-ray time integral but delayed. Once the Hα emission peaks, we reach the decay phase of the flare, where only EUV emission continues to increase for a time.

1.3.1 Particle Acceleration & Transport Theories

It is thought that magnetic reconnection allows the release of energy stored in the pre-flare magnetic field. A simple field configuration thought to result in this

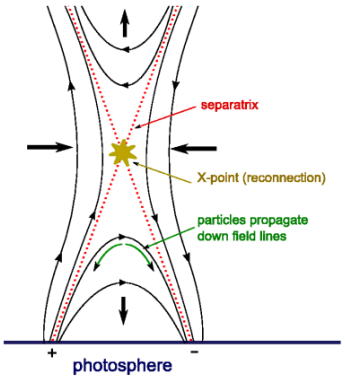

Figure 1.4: 2-D representation of an X-type neutral point where magnetic reconnection is believed to occur.

[Image Copyright]

Figure 1.5: 3-D representation of a magnetic reconnection region [Priest & Forbes (2002), Figure 23b]

phenomena is the X-type neutral point, which can be simplified to two dimensions (Figure 1.4), although a complete treatment would consider the full three dimensions (Figure 1.5). The theory of magnetic reconnection and the underlying field configuration is an ongoing area of research. One of the earliest models was developed by Sweet & Parker in the late 1950s and early '60s (Sweet (1958), Parker (1963)), a basic two-dimensional reconnection model where magnetic field merges at a current sheet of defined size, unlike the null point postulated for X-point reconnection. A variation on this was proposed by Petschek (1964), where the current sheet is reduced in size, enabling faster reconnection. Theories continue to be studied in detail - see Priest & Forbes (2002), Aschwanden (2002).

Field lines on either side of the X-point push toward each other due to magnetic forces and eventually break open from their current configuration and recombine to make a new loop, which rapidly contracts downward. When the field reconfigures in this way, large amounts of energy are released and particles present in the ambient plasma and reconnecting field lines (both electrons and ions) are believed to be accelerated onto the newly formed loop with very high energies, from 50 - 100 keV in an average flare (Fletcher & Petkaki (1997)), to as much as 70 MeV (for electrons, 2 GeV for ions) in large (but brief) γ-ray emitting flares (Sakai (1992)). These accelerated particles are thought to propagate along the new loop in both directions from the looptop, and as they do so they undergo Coulomb collisions with the ambient background plasma particles in the loop. It is thought that these collisions result in non-thermal hard X-ray emission and an increase in the temperature of the background plasma in the loop, which in turn emits thermal X-rays.

Exactly how these particles are accelerated onto the newly formed loops re-

mains a hotly debated topic. Possible theories include stochastic acceleration as a result of magnetohydrodynamic turbulence in the plasma (e.g. Hamilton & Petrosian (1992), Miller & Ramaty (1992)), direct acceleration from electric fields formed in the reconnection region (e.g. Litvinenko (1996), Holman (1995)), and secondary acceleration from shock waves formed in the plasma during the reconnection event (e.g. Tsuneta & Naito (1998), Cargill et al. (1988)). However, the work presented in this thesis does not concern the mechanism of acceleration, only the propagation of the accelerated particles, and effects of that propagation, along the loop.

1.3.2 Loop Heating

It has been observed that during a flare, the plasma in the newly formed magnetic loops is heated to high temperatures as energy is released when the field reconfigures (e.g. Warren & Reeves (2001)). In the early stages of the flare, loops are heated to 10 - 30 MK, at which point emission is dominated by soft X-rays, and at later stages they cool to a few million Kelvin, where the primary emission is in the extreme ultraviolet range.

Several heating mechanisms are proposed to explain the temperature increase in magnetic loops during flares. There is the theory of resistive heating, whereby electric fields created during reconnection are dissipated by Joule heating of the plasma (e.g. Holman et al. (1989)); the theory of shock heating, whereby the shock waves generated in the plasma at the reconnection point heat the plasma as they propagate (e.g. Cargill & Priest (1983)); the theory of inductive current heating, whereby a loop with a specific resistivity and voltage dissipates current according to Ohm's Law ($P = RI^2$) which is converted to heat (e.g. Melrose (1995)); and the theories of electron and proton beam heating, where electrons and protons accelerated at the reconnection point propagate down the loop and cause the temperature of the background plasma to increase through Coulomb collisions (e.g. Brown (1973), Fletcher & Martens (1998), Voitenko (1996)). No single theory has proven sufficient in itself to account for the observed temperatures in loops and thus finding out what exact physical processes are at work is an ongoing topic of investigation. In this thesis, we investigate the propagating electron beam model.

Electrons that are accelerated onto the newly formed loops propagate along the magnetic field and undergo Coulomb collisions with the ambient background

particles - the energy lost by the propagating particles through these collisions is deposited into the background plasma, increasing its temperature. When the propagating particles reach the photosphere, they impact with the denser plasma there and cause it also to increase in temperature. This hotter plasma then expands up into the loop in a process known as "chromospheric evaporation" (or more correctly, "chromospheric ablation"), which in turn increases the temperature of the loop further (Bornmann (1999), Fisher et al. (1985)). In the work presented here, we do not consider the process of chromospheric evaporation, only the temperature increase as a result of the interaction of the propagating accelerated particles with the background plasma through stochastic processes.

1.3.3 X-Ray Emission

X-ray emission is produced by the collisions between the accelerated fast electrons and the effectively stationary (by comparison) ions of the background plasma through which they propagate, and also between particles within a heated plasma. These two types of X-ray emission are described as "non-thermal" and "thermal" emission respectively. Non-thermal emission is generally in the range $\sim$ 10 - 100 keV (hard X-rays) and thermal emission in the range $\sim$ 1 - 10 keV (soft X-rays). By observing the X-ray radiation incident at Earth, we are able to work backwards to infer the particle populations that resulted in the emission (e.g. Brown (1971), Brown et al. (2003)), and hence learn more of the particle acceleration and propagation processes present in flaring loops.

The earliest X-ray observations of the Sun were taken by NASAs Orbiting Solar Observatory (OSO) satellites in the late 1960s and early 70s, although there was not a dedicated X-ray telescope, and there was no spatial resolution at X-ray wavelengths. These satellites were succeeded over the years by missions such as the Solar Maximum Mission (SMM) which was operational throughout the 80s, and was specifically dedicated to observing solar flares. It was capable of imaging X-ray emission and had a maximum spatial resolutions of 8" depending on the energy band. The Japanese mission Yohkoh succeeded SMM, and provided higher resolution images up to 5" throughout the 90s, but was unfortunately lost due to a technical error. It has been replaced with the joint JAXA (Japanese Aerospace Exploration Agency) / ESA / NASA mission, Hinode, which was launched in September 2006, and which is now running concurrently with the NASA satellite RHESSI which has already been in operation for 5 years. Hinode carries a grazing

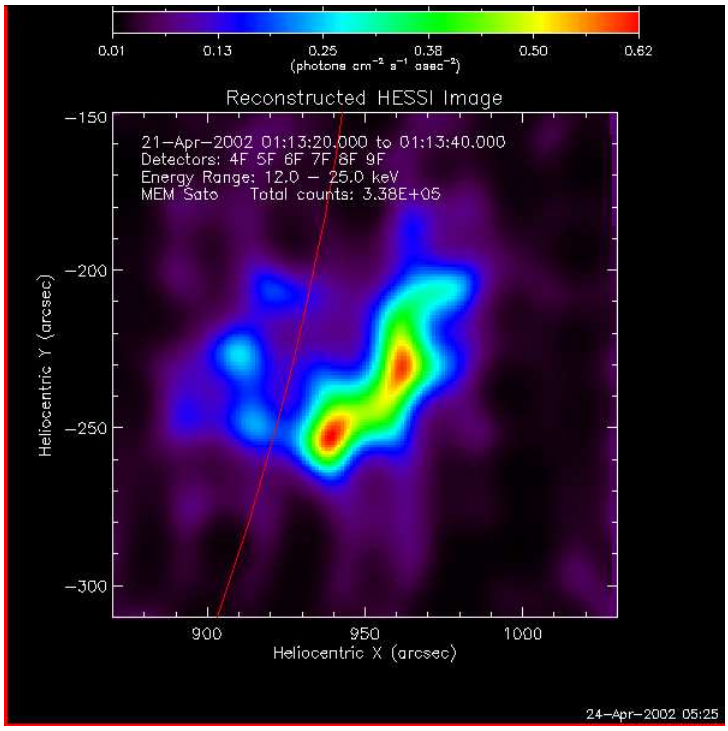

Figure 1.6: First X-class flare detected by RHESSI, 21st April 2002, shown in the energy band 12-25 keV. [Sato (2002) / NASA]

incidence X-ray telescope with a maximum spatial resolution of 2", as well as high resolution optical and EUV telescopes. RHESSI on the other hand, uses a rotation-modulated collimator - different Fourier components of the incident X-ray flux are measured as the telescope rotates, and these are then combined and an image reconstructed using various algorithms (see Hurford et al. (2002)). This provides a spatial resolution of up to 2.3", and the energy resolution of the telescope is 3 keV to 17 MeV, allowing observations of γ-ray emission as well as X-ray. Current observational capabilities do not provide highly detailed spatial resolution, but they do provide high energy resolution and temporal resolution down to 2 seconds for the most detailed images (both Hinode and RHESSI).

RHESSI images X-rays in several energy bands - in the hard X-ray range, these are 6-12 keV, 12-25 keV, 25-50 keV and 50-100 keV. Figure 1.6 shows the first X-class flare detected by RHESSI. This image shows the emission in the energy band 12-25 keV and is summed over 20 seconds. RHESSI also produces X-ray photon flux spectra (c.f. Figure 1.7), a plot of the number of photons incident on the detector per cm^2 per second per unit photon energy. From these

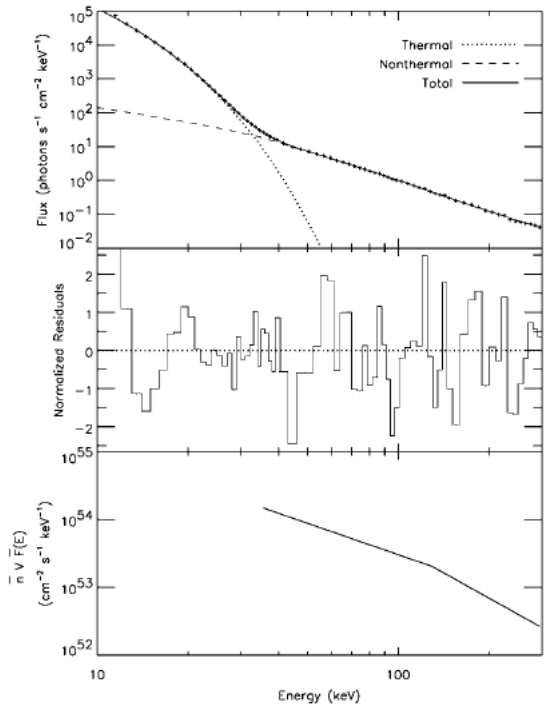

Figure 1.7: RHESSI X-ray photon flux, residuals and mean electron flux, $F(E)$ $(= f(E)nV)$, for the July 23rd 2002 flare, using forward fitting techniques. Holman et al. (2003), reproduced by permission of the AAS.

spectra, it is possible to work backwards to determine the effective mean electron flux spectrum, $F(E)$ (which is $f(E)$, the electron energy distribution function, integrated over volume and weighted with respect to the density) (Brown (1971), Brown et al. (2003), Piana et al. (2003)).

One of the key discoveries from X-ray observations in the past decade has been that of looptop hard X-ray sources (Masuda (1994)), which supports the theory that electrons are accelerated at the point of magnetic reconnection. Since non-thermal X-ray bremsstrahlung emission is linearly dependent on density, it would be expected that most of this type of emission would originate at loop footpoints, since the density increases sharply across the chromosphere and into the photosphere. However, high energy sources have also been observed on and above the loop apex in several flares (Figure 1.8). Some of this emission is at the lower energy range of hard X-rays, and is consistant with thermal emission from a hot plasma of temperatures up to 30 MK, but there is also a higher energy component which it is proposed results from non-thermal electrons accelerated

Figure 1.8: Yohkoh hard X-ray (top) and soft X-ray (bottom) images of the flare on the 13th of January 1992, showing a hard X-ray source located above the looptop of the soft X-ray emitting loop. [Masuda (1994)), Figure 1]

onto the loop at the reconnection point. Furthermore, these looptop sources appear concurrently with the footpoints sources and last for roughly the same length of time.

Possible explanations for this hard X-ray looptop source are a high loop density, up to 10^{11} cm^{-3} (Holman (1996)) (as opposed to the more usual accepted value of $\sim 10^9$ cm^{-3}, Fletcher & Martens (1998)), particle trapping in the loop as a result of the converging field at the footpoints (the "magnetic bottle" effect) (e.g. Fletcher & Martens (1998)) and very high loop temperature at the apex (Masuda (1994)). Particles trapped by the field will mirror back and forth across the loop apex, producing non-thermal X-ray emission until they are scattered into the loss cone, or until they run out of energy - this will increase the looptop hard X-ray intensity with respect to the foopoint intensity depending on how long the particles remain trapped, which in turn is a property of the field configuration, initial particle energy and loop density. If the density is higher, the particles will emit more non-thermal bremsstrahlung X-rays, but they will also be scattered into the loss cone more quickly, meaning they remain trapped in the loop for less time. Thermal X-rays would require a very high temperature to be significant in this process - for X-rays of energy 20 keV, the plasma temperature would have to reach approximately 100 MK, for which there is no observational evidence so

far.

The work presented in this thesis includes simulations of non-thermal electron populations injected into various magnetic loop configurations and shows the resultant hard X-ray emission as a function of both time and position in various energy bands. We also present X-ray spectra from these simulations similar in form to that seen in the top panel of Figure 1.7, by combing thermal and non-thermal X-ray emission from the heated plasma in the loop and the interactions of the injected non-thermal electron population.

1.3.4 Radio Emission

Radio emission from the Sun was first detected as interference in World War II radar detectors (Hey et al. (1948)), and has been observed extensively ever since. Since radio passes easily through the Earth's atmosphere in the range 1 cm to 10 m (30 GHz to 10 MHz), it is one of the most studied wavelength ranges along with visible light. Early observations were not able to produce images, only spectra, from metric to millimetre wavelengths, but with the development of radio interferometers, imaging became possible using Fourier transforms to construct images from the received signal. Current radio telescopes include the Very Large Array (VLA) in New Mexico, which uses synthesised aperture techniques to create high resolution images, the Nancay Radioheliograph in France, and the Phoenix 2 radio spectrometer at ETH Zurich.

There are two main types of radio emission observed from the Sun - coherent emission and incoherent emission. Incoherent emission arises from continuum processes such as bremsstrahlung emission from thermal plasma and gyrosynchrotron emission from fast electrons. Coherent emission occurs when a particle distribution becomes unstable and develops a positive slope (i.e. $\frac{\partial f}{\partial v} > 0$) in either the parallel (plasma emission) or perpendicular (electron-cyclotron maser emission) direction to the magnetic field.

Electron beams propagating along a magnetic field line produce coherent plasma radio emission known as Type III emission - upward propagating beams produce regular (normal-drift) Type III bursts and downward propagating beams produce reverse-drift Type III bursts, so named because their frequency decreases with time (Figure 1.9). Emission can also be described as U-bursts, caused by an electron beam crossing the apex of a loop and changing direction (frequency increases then decreases over time) and J-type bursts (a partial U-type burst),

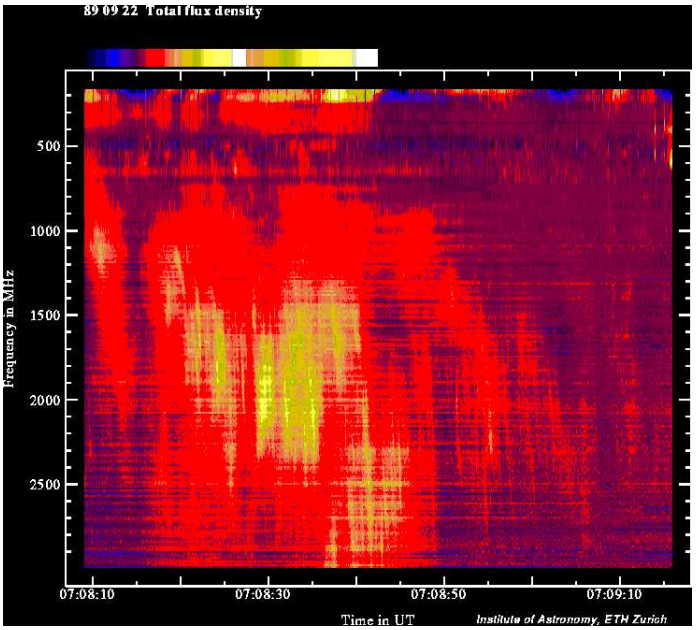

Figure 1.9: Reverse-drift Type-III radio bursts for an event on 22nd Sept 1989, from the Phoenix radio spectrometer of ETH Zurich. [ETH Zurich]

both named from their shape in a dynamic spectrum plot. In this thesis, we consider only reverse-drift Type III emission in the radio band.

The fastest electrons in an injected distribution propagate more quickly along the loop, reaching a given position before the lower energy electrons. Pitch angle distribution also plays a part in that angles with smaller initial pitch angles with respect to the direction of the field undergo a smaller number of collisions and are slowed less quickly, and hence propagate along the loop faster. This creates a "bump" in plots of the combined velocity distribution of the thermal (background) and non-thermal (beam) electrons, which has a positive slope for a small range of positions. This creates an unstable electron distribution (the "bump-in-tail instability"), which causes Langmuir waves to develop in the plasma. These undergo non-linear wave interactions which in turn produce electromagnetic emission at the electron plasma frequency, which is dependent on the plasma density, and for coronal densities of $\sim 10^8$ - 10^{10} cm^{-3} this corresponds to radio wavelengths.

The unstable electron distribution resulting in Type III bursts has been measured by the International Sun Earth Explorer 3 (ISEE-3) satellite located at the Sun-Earth Lagrange point, for example during the flare of Feb 17th 1979 (Lin

et al. (1981), Lin et al. (1986)), showing clearly the positive slope in the electron velocity distribution of a beam propagating outwards from the Sun along an open field line. Other observations show a correlation between both normal-drift and reverse-drift Type III bursts and hard X-ray emission in a magnetic loop topology, indicating that the beams that cause both phenomenon are one and the same, although the radio emission is observed to be delayed by $\Delta t = 270 \pm 150$ ms with respect to the hard X-ray emission as a result of the growth time of Langmuir waves in the plasma and the different energies of the particles resulting in hard X-ray and radio emission (Aschwanden et al. (1993)). Our results appear to confirm this observation, as discussed in Chapter 6.

Chapter 2

Methods & Testing

2.1 Stochastic Simulations

2.1.1 Introduction

A stochastic simulation is a form of numerical simulation which models the movement of test particles which are influenced by random effects. It involves step-wise modelling of random physical processes, such as diffusion and scattering of particles via Coulomb collisions, without having to explicitly solve the equations of motion of the test particles under the influence of surrounding particles. Instead, we treat the effects of surrounding particles in a statistical manner by looking at the evolution of the distribution function as a whole. The accuracy of this method depends on the process being modelled, the degree of complexity of the equations describing said process, and the way in which the equations are implemented within the simulation.

We use stochastic simulations to model the evolution of the electron distribution function. The equation describing this distribution function can be written in the form of a set of stochastic partial differential equations (see Section 2.1.2 below). These equations can be used to numerically calculate the movement of electrons along a magnetic field line over time in a step-wise fashion and hence model the resultant effects associated with this process, such as X-ray emission, radio emission, and heating of the background plasma through particle collisions.

2.1.2 Theory

The distribution of a beam of fast electrons (the electron distribution function, f) can be described by the conservation equation[Parks (2004)]:

$$\frac{\mathrm{d}f}{\mathrm{d}t} = \frac{\partial f}{\partial t} + \mathbf{v} \cdot \frac{\partial f}{\partial \mathbf{r}} + \mathbf{a} \cdot \frac{\partial f}{\partial \mathbf{v}} \tag{2.1}$$

(where $f = f(\mathbf{r}, \mathbf{v}, t)$. In the absence of collisions, the distribution function obeys the continuity (Liouville) equation:

$$\frac{\partial f}{\partial t} + \nabla_{\mathbf{r},\mathbf{v}} \cdot [\, (\dot{\mathbf{r}}, \dot{\mathbf{v}}) f \,] = 0 \tag{2.2}$$

where the second term represents a divergence in phase space of the function f, and the particles move in continuous curves. In Cartesian co-ordinates, this is written:

$$\frac{\partial f}{\partial t} + \frac{\partial}{\partial x_i}(f\dot{x_i}) + \frac{\partial}{\partial v_i}(f\dot{v_i}) = 0$$

$$\text{i.e.} \quad \frac{\partial f}{\partial t} + \left(\frac{\partial \dot{x_i}}{\partial x_i} + \frac{\partial \dot{v_i}}{\partial v_i}\right) + \frac{\partial f}{\partial x_i}\dot{x_i} + \frac{\partial f}{\partial v_i}\dot{v_i} = 0 \tag{2.3}$$

It can be shown that $\frac{\partial \dot{\mathbf{v}}_\mathbf{i}}{\partial v_i} = 0$ and $\frac{\partial \dot{x_i}}{\partial x_i} = 0$, since v_i and $\dot{v_i}$ are independent variables, x_i and $\dot{x_i}$ are also independent variables. Thus Eq. 2.3 can be written:

$$\frac{\partial f}{\partial t} + \frac{\partial f}{\partial x_i}\dot{x_i} + \frac{\partial f}{\partial v_i}\dot{v_i} = 0 \tag{2.4}$$

This is the Boltzmann Equation and is the same as Eq. 2.2 if $\frac{df}{dt} = 0$, which is true for a collisionless plasma. Thus the Boltzmann equation is a continuity equation in this situation. When electromagnetic forces are introduced, the Boltzmann Equation becomes:

$$\frac{\partial f}{\partial t} + \mathbf{v} \cdot \frac{\partial f}{\partial \mathbf{r}} + \frac{q}{m}(\mathbf{E} + \mathbf{v} \wedge \mathbf{B}) \cdot \frac{\partial f}{\partial \mathbf{v}} = 0 \tag{2.5}$$

which is the Vlasov Equation. The Vlasov equation, when collisions are introduced and the magnetic field is zero, provides the basis of the evolution of the electron distribution function. This is described by the following where the first two terms describe the temporal and spatial variations respectively, and the last two terms describe the effects of collisions[MacKinnon & Craig (1991)]:

$$\frac{\partial f}{\partial t} + \mu v \frac{\partial f}{\partial s} - D\frac{\partial}{\partial v}\left(\frac{f}{v^2}\right) - \frac{D}{v^3}\frac{\partial}{\partial \mu}\left((1-\mu^2)\frac{\partial f}{\partial \mu}\right) = 0 \tag{2.6}$$

where s is the distance along the field line, $\mu = \cos\theta$, the angle of the particle with respect to the magnetic field (B) (i.e. the particles pitch angle), and $D = \frac{4\pi e^4 \Lambda n}{m_e^2}$,

the diffusion coefficient in pitch angle for an electron. In using this equation, we assume that the gradient and curvature drifts are insignificant (see Section 2.2.3) and that no electric fields are generated by the movement of the particles. $n \simeq 10^9\,\mathrm{cm}^{-3}$ is the coronal number density and Λ is the Coulomb logarithm. The Coulomb logarithm is the logarithm of the ratio of the upper and lower cut-offs of the impact parameter of the particle undergoing collisions, and, for electron-electron collisions, can be approximated by[Baumjohann & Treumann (1996)]:

$$\Lambda = 4\pi n \lambda_D^3 \tag{2.7}$$

where the Debye length is given by $\lambda_D = \sqrt{\frac{k_B T}{4\pi n e^2}}$ cm. We consider a background plasma of ambient temperature 10^6 K ($\sim$ 86 eV), which yields a value of $\Lambda \simeq 20$. Now, with the inclusion of a variable magnetic field, Equation 2.6 becomes[Fletcher (1995)]:

$$\frac{\partial f}{\partial t} + \mu v \frac{\partial f}{\partial s} - D\frac{\partial}{\partial v}\left(\frac{f}{v^2}\right) - \frac{v}{2}\frac{\partial}{\partial \mu}\left((1-\mu^2)\frac{dlnB}{ds}f\right) - \frac{D}{v^3}\frac{\partial}{\partial \mu}\left((1-\mu^2)\frac{\partial f}{\partial \mu}\right) = 0 \tag{2.8}$$

This is a **Fokker-Plank type equation**, and a Fokker-Plank equation can be shown to be equivalent to a set of stochastic differential equations (Gardiner, 1985). The equations in this particular case are:

$$\begin{aligned} \mathrm{d}s &= \mu v\,\mathrm{d}t \\ \mathrm{d}v &= -\frac{D}{v^2}\,\mathrm{d}t \\ \mathrm{d}\mu &= \left[-\frac{2D\mu}{v^3}\right]\mathrm{d}t + \left[-\frac{v}{2}(1-\mu^2)\frac{\partial lnB}{\partial s}\right]\mathrm{d}t + \left[\frac{2D}{v^3}(1-\mu^2)\right]^{1/2} dW(t) \end{aligned} \tag{2.9}$$

where $dW(t)$ is a Gaussian random noise process of mean 0 and variance 2 (essentially a number chosen at random from a Gaussian distribution, since the random walk nature of the pitch angle scatterings is described by a Gaussian of variance $2\sqrt{\Delta t}$), and includes a scaling factor of $\sqrt{\mathrm{d}t}$. We note here that the use of a Gaussian function does not represent the physical process of scattering completely accurately, since it has limits of $\pm\infty$, whereas the cosine of the pitch angle has limits of ± 1. However, it does effectively represent small angle scattering, which is the most common scattering interaction.

These last three equations describe the behaviour of a test particle (in our case, an electron) moving along a magnetic field and undergoing random collisions with the background particles. These equations can be incremented over time to

simulate the movement of the test particle. Repeating this process for many particles allows us to track the movements of electrons along magnetic field lines over time and build up a picture of the electron distribution function. In this work, we consider only non-relativistic electrons - this is suitable for particles in the energy ranges we are considering. Our upper cut-off for particle energy gives a ratio of $\frac{v}{c} \simeq 0.6$ (the highest energy particles are ~ 113 keV), however, the majority of particles are at a much lower energy, since the injection profile is a power law distribution. Particles below $\simeq 150$ keV are considered to be non-relativistic [Bai & Ramaty (1976)].

2.1.3 Basic Simulations

We use stochastic simulations to model the movement of fast electrons propagating along magnetic field lines in the solar atmosphere. These electrons (our test particles) are injected onto the apex of a magnetic loop and propagate along it in both directions, emitting bremsstrahlung radiation as they lose energy, and heating the background coronal plasma through Coulomb collisions. By simulating the distribution function of this population of electrons we are able to investigate the hard X-ray emission produced in loops with various physical characteristics. The simulations also allow us to calculate the energy deposited by the electrons through collisions with the ambient particles of the coronal background plasma (see Chapter 4).

Our simulations are written using the Java programming language (with the results output using the IDL language), and are based on earlier work by MacKinnon & Craig (1991). In these simulations we take Equations 2.9 and use these to calculate the movements of test particles (electrons) along magnetic field lines with various geometries (see Section 2.2) and physical parameters (see Section 2.1.5). These test particles are injected onto the apex of the loop (i.e. at $s = 0$ cm) with specified initial pitch angles and velocities. The programs increment step by step over small time intervals, calculating the small changes in s, v and μ for a particle over each timestep using Equations 2.9. By binning the velocity of each particle at each position along a magnetic loop at frequent time intervals we are able to build up histograms of the electron distribution function evolving over time.

This is the core of our simulations, to which we add routines to calculate X-ray emission (see Section 3.1) and to calculate heating (as well as cooling through

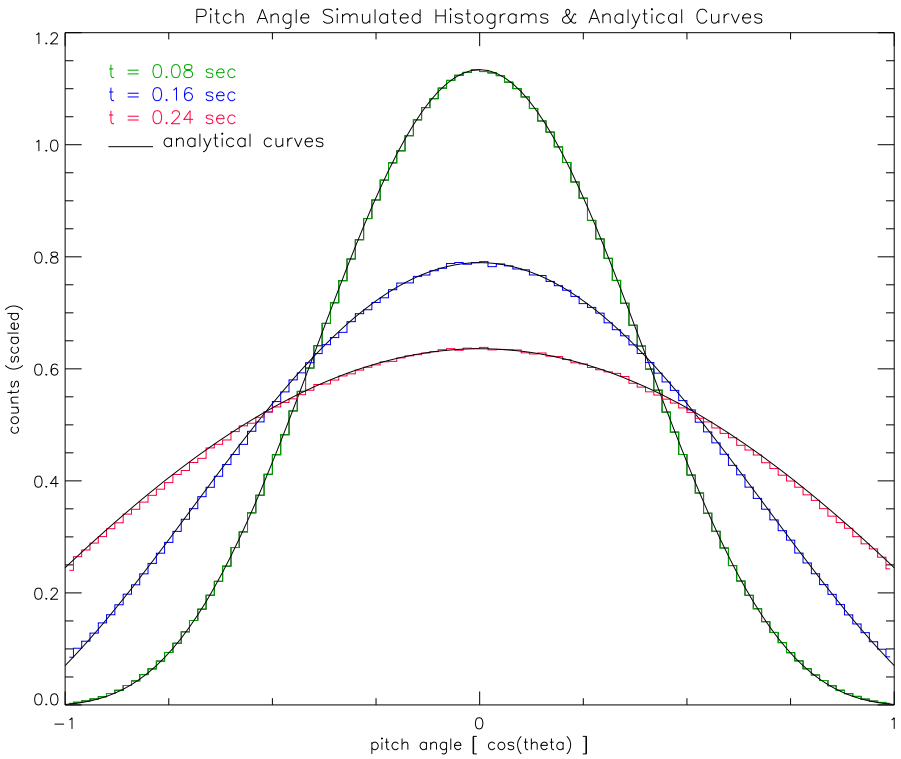

Figure 2.1: Simulated histograms of the electron pitch angle distribution over time (coloured histogram plots) overplotted with the analytical solution (solid black curves), for uniform magnetic field and density. Run for 0.24 sec, with 10^7 particles and 100 bins in pitch angle. The match is excellent at each time, showing the reliability of the simulations in modeling the evolution of the pitch angle scattering of the electrons over time, and hence the evolution of the distribution function.

radiation and conduction) of the background plasma as a result of collisions (see Section 4.1).

The distribution function histograms need to be scaled up to represent realistic loop parameters - limitations in processing power and data storage prevent us from running simulations to scale because of the large timescales and numbers of particles involved. Thus, we simulate a smaller number of particles than is expected in a real loop and apply a scaling factor when using the histograms to calculate X-ray emission, and when calculating temperatures - see Sections 3.1.1 and 4.2 for details of this scaling.

2.1.4 Testing Basic Simulations

We initially tested the accuracy of the most basic implementation of the simulations - one that calculates and records the movements of a number of test particles over time in a uniform magnetic field and uniform density, and does

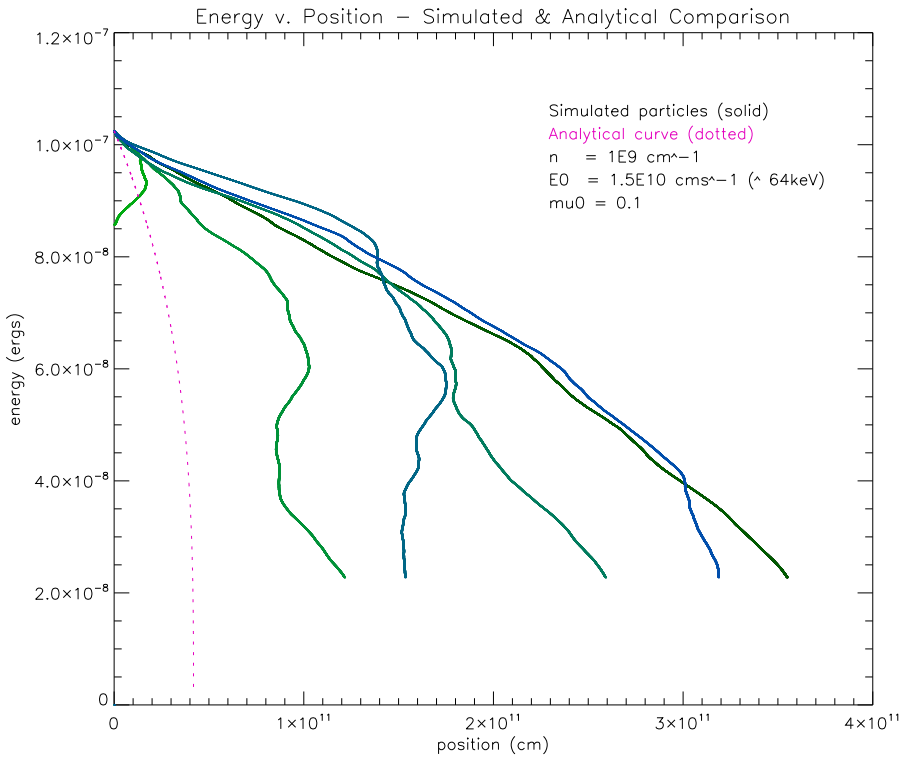

Figure 2.2: Plot of a selection of particles' energies as a function of position, with initial angles of injection $\mu = 0.1$ ($\sim 84°$) and initial velocity $1.5 \times 10^{10}\text{cms}^{-1}$ ($\sim$64keV). The expected theoretical energy (neglecting scattering) as a function of position for particles with these initial parameters is plotted as a dotted line.

not include any calculations of heating, cooling and emissions. It does, however, include the effects of diffusion through Coulomb collisions with the ambient background particles (which we assume to be protons in a fully ionised plasma) which are implicitly included in Equation 2.6. The first simulation here uses a simplified form of Equations 2.9 in which the magnetic field is constant (meaning it has no effect on the movements of the test particles) and hence the term containing the derivative of the magnetic field ($\left[-\frac{v}{2}(1-\mu^2)\frac{\partial lnB}{\partial s}\right] \mathrm{d}t$) disappears.

By plotting spatially integrated histograms of the pitch angle distribution over time, with the expected analytical distribution plotted on top, we can check the accuracy of our simulations.

To calculate the analytical solution, we cannot solve the equation for the electron distribution function (Eq. 2.1) directly, but a spatially integrated solution can be arrived at (see MacKinnon & Craig (1991), Lu & Petrosian (1988) and Kel'ner & Skrynnikov (1985) for details) which can be described in terms of

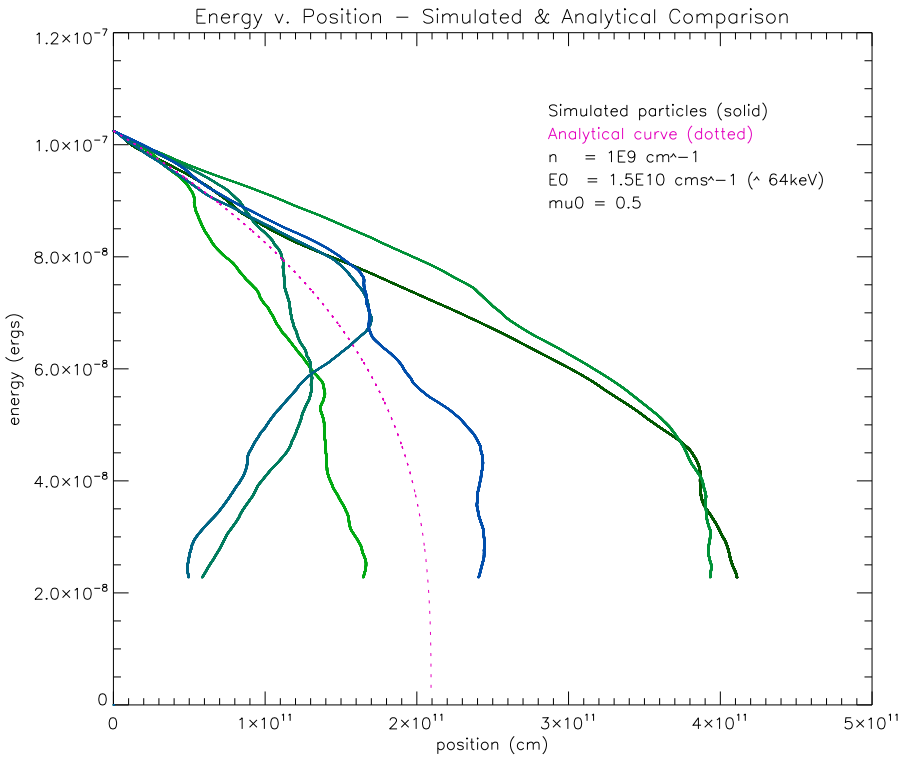

Figure 2.3: Plot of a selection of particles' energies as a function of position, with initial angles of injection $\mu = 0.5$ (60°) and initial velocity $1.5 \times 10^{10}\text{cms}^{-1}$ (∼64keV). The expected theoretical energy (neglecting scattering) as a function of position for particles with these initial parameters is plotted as a dotted line.

Legendre polynomials:

$$F(v,\mu,t) = \delta(v - (1-3t)^{\frac{1}{3}}) \sum_{n=0}^{\infty} (1-3t)^{n(n+1)/3} a_n P_n(\mu) \tag{2.10}$$

where n is an integer, t is time and $P_n(\mu)$ is a Legendre polynomial (a solution of the Legendre differential equation, which is calculated using existing functions in the programming language).

The analytical solution (dimensionless) for the velocity of a particle is given by $v(t) = (1-3t)^{\frac{1}{3}}$, from integrating the dimensionless form of the differential equation for v, $\mathrm{d}v = -\frac{1}{v^2}\,\mathrm{d}t$ (MacKinnon & Craig (1991)), therefore:

$$F(v,\mu,t) = \sum_{n=0}^{\infty} (1-3t)^{n(n+1)/3} a_n P_n(\mu) \tag{2.11}$$

where

$$a_n = (n+\frac{1}{2}) \int_{-1}^{1} M(\mu) P_n(\mu) d\mu \tag{2.12}$$

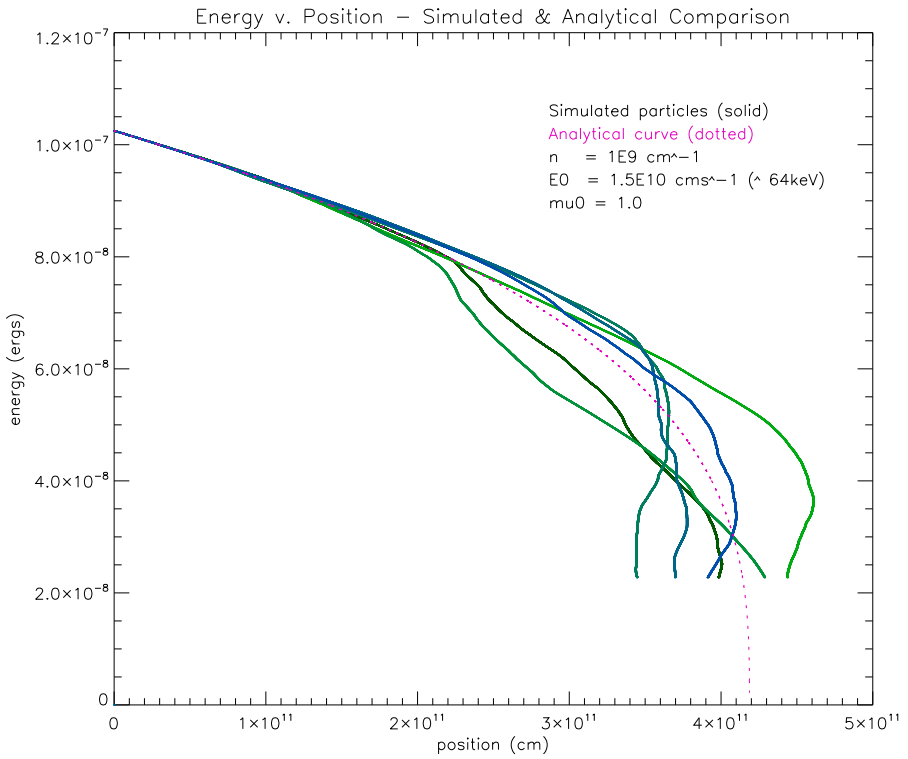

Figure 2.4: Plot of a selection of particles' energies as a function of position, with initial angles of injection $\mu = 1.0$ (0°, i.e. parallel) and initial velocity $1.5 \times 10^{10}\text{cms}^{-1}$ (∼64keV). The expected theoretical energy (neglecting scattering) as a function of position for particles with these initial parameters is plotted as a dotted line.

The initial condition is such that $M(\mu) = \delta(\mu - \mu_0)$, i.e all particles are injected with initial pitch angle $\mu = \mu_0$. The integral of a delta function is zero everywhere except at its condition, therefore:

$$a_n = (n + \frac{1}{2})P_n(\mu_0) \tag{2.13}$$

Thus the analytical solution (describing the evolution of the pitch angle distribution over time) is given by:

$$F(\mu, t) = \sum_{n=0}^{\infty}(1 - 3t)^{n(n+1)/3}(n + \frac{1}{2})P_n(\mu_0)P_n(\mu) \tag{2.14}$$

where μ_0 is the initial angle of injection of a particle.

Plotting this analytical solution for the electron pitch angle distribution over time on top of the simulated pitch angle histograms (Figure 2.1) we can see that the output from the simulations is in excellent agreement with that predicted by the analytical solution. The number of counts in the simulated pitch angle

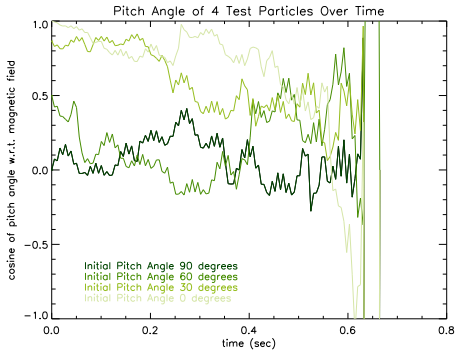

Figure 2.5: Plot of pitch angle of four test particles over time, with various initial angles of injection.

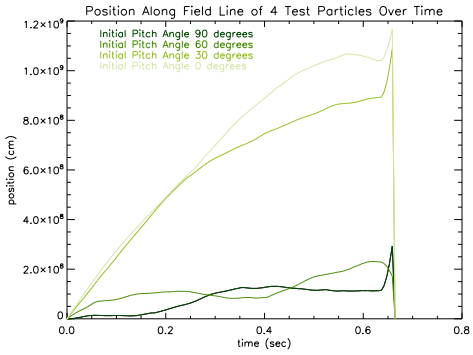

Figure 2.6: Plot of position of four test particles over time, with various initial angles of injection.

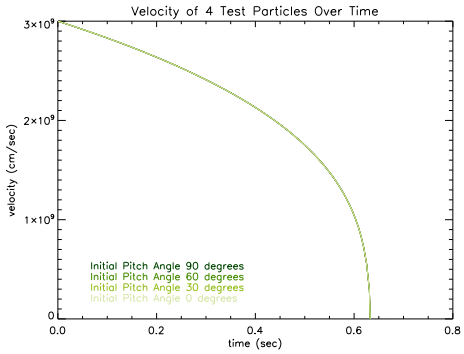

Figure 2.7: Plot of velocity of four test particles over time, with various initial angles of injection. This is the same for each, since overall velocity decreases steadily with time.

histograms have been normalised in order to compare with the analytical solution, which is dimensionless.

The process described above tests the accuracy of the simulations directly, by comparing the pitch angle distribution over time with the analytical solution. We can also compare the rate of energy lost by a particle in the simulation with the expected energy loss predicted by theory.

The energy a particle would be expected to have after a given distance, using a mean scattering treatment (which describes the behaviour of a particle with a scattering angle that is the average of the distribution), is described by[Emslie (1978)]:

$$E = E_0 \left[1 - \frac{3\Lambda K N}{\mu_0 E_0^2} \right]^{\frac{1}{3}} \tag{2.15}$$

where E is the energy of the particle at a given position, E_0 is the initial energy of the particle and μ_0 is the initial pitch angle of the particle. $K = 2\pi e^4$, and

N is the column density, which is $\int_{-\infty}^{s} n(s)ds$, which in this case equals ns since we are considering a constant magnetic field (loop) with only one dimension (the direction along the field line, s), and where n is the density of the background plasma in the loop and is also constant. Λ is the Coulomb Logarithm, for which we use the value ~ 20 (see Section 2.1.2).

In Figures 2.2, 2.3 and 2.4 we plot the energies of a number of test particles, each with the same initial energy but with various pitch angles, as a function of position along with the analytical values for each pitch angle. We can see from these Figures that the larger the angle of injection to the field line, the less the particles' energy loss over position follows the predicted values. This is because particles that are injected at larger angles to the field line (i.e. more perpendicular), take longer to travel the same distance along the field line as ones injected closer to parallel, and as a result have undergone more scattering in the intervening time. This results in larger discrepancies between the analytical and simulated results, since the equation for the analytical solution (Eq. 2.15) does not take dispersion into account, only the average scattering, whereas the equations on which the simulations are based, do include dispersion. In Figure 2.4, where particles were injected parallel to the field, we can see that the resultant energy as a function of position matches the predicted values closely at early times, but begins to diverge as the test particles undergo more and more scattering with the background particles. This result is as we expect, and verifies that the energy loss as calculated by the simulation is physically valid.

Finally, as a further test of the simulations, we can plot the various parameters of a number of test particles (such as pitch angle, velocity and position over time) to check that they behave as we would expect. In Figure 2.5 we plot the changes in pitch angle of four particles with different initial angles of injection over time. We can see that the particles undergo random scattering in pitch angle over time as expected, through collisions with ambient particles. We can also see that after approximately 0.64 sec the particles run out of energy and stop. This is particularly clearly illustrated in Figure 2.7, which plots the same particles' velocities over time. We can calculate the expected time for the particles to run out of energy using the following equation for the energy loss rate of a particle with initial energy $\lesssim 160$ keV[Bai & Ramaty (1979)]:

$$-\frac{dE}{dt} = 4.9 \times 10^{-9} n E^{-1/2} \tag{2.16}$$

where energy is measured in keV and density in cm^{-3}. For a particle of initial

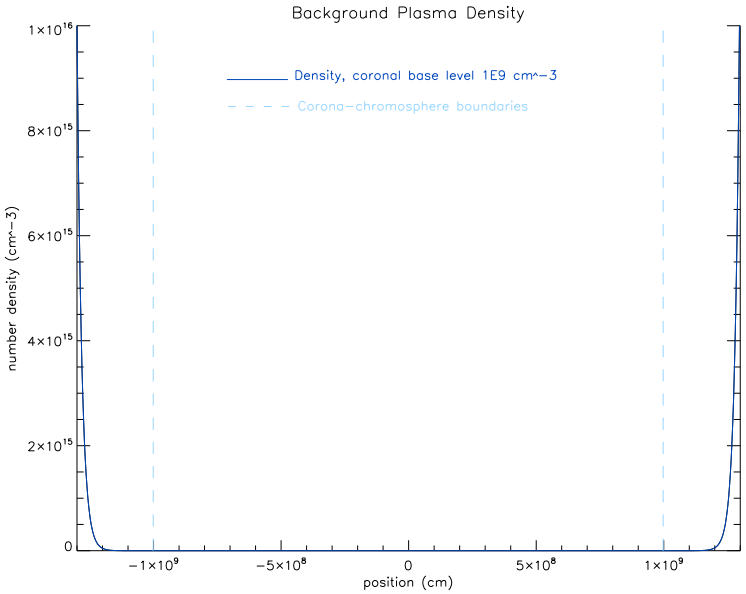

Figure 2.8: Plot of density as a function of position along a magnetic loop of length 1.3×10^9cm from looptop to the photosphere. Vertical dotted lines indicate the start of the chromosphere, at which point the density increases rapidly towards the photosphere. The base level throughout the corona is $1 \times 10^9 \text{cm}^{-3}$ in this graph (not resolved due to scaling). The form of the density model is described by Equation 2.17.

energy 2.56 keV (3×10^9 cms^{-1}, as in Figure 2.7) this gives a stopping time of approximately 0.56 sec. Given that particles also lose energy via other mechanisms (for example gyrosynchrotron radiation) and thus would be expected to stop slightly more quickly than predicted by our simulations (which only consider collisional energy losses), we believe this to be acceptably close to the simulated value. The absolute velocity of the particles decreases steadily with time, and is the same for each particle when the initial velocities are the same (as they are here). The velocity along the field line (which is not plotted here) varies with pitch angle. In Figure 2.6 we plot the position of these four particles over time, which increases as expected, with scattering resulting in non-uniform curves.

Taking all the above tests into account, we are confident that the simulations are acceptably accurate given the underlying equations, their limitations and the assumptions we have made in simplifying the physical model. The tests produce results in accordance with physical expectations.

2.1.5 Model Parameters

Our simulations are designed such that certain parameters can be easily modified in order to investigate their effect. The closest of our simulations to realis-

tic parameters have initial angles of injection chosen randomly from a uniform distribution of pitch angles between 0° and 180°, with $0° < \theta < 90°$ corresponding to particles travelling forward (the positive direction along the loop) and $90° < \theta < 180°$ corresponding to particles travelling backwards (the negative direction along the loop). 50% of the particles are injected in the positive direction and 50% in the negative direction from the point of origin at the looptop. Other injection profiles could be used in future work, but are not considered here due to time limitations.

The initial velocities of particles are chosen randomly from a power law distribution, for example, between 1×10^{10}cms^{-1} and 2×10^{10}cms^{-1}. We treat particles as non-relativistic throughout, an assumption which is adequate for our purposes, provided we do not increase the upper limit on initial velocity.

The magnetic loop length used in our simulations is 10,000 km long as measured from the looptop to the start of the chromosphere, and the chromosphere has a depth of 3000 km. We also include a variable background density model - the density is assumed to be constant throughout the corona (10^9 cm^{-3} unless stated otherwise), and increases rapidly across the chromosphere to a value of 10^{16} cm^{-3} at the photosphere (see Figure 2.8). The increase across the chromosphere is described by:

$$n = n_1 e^{\frac{-(s_1 - abs(s))}{h_0}} \tag{2.17}$$

where n_1 is the photospheric density (10^{16} cm^{-3}), s_1 is the photospheric boundary (end of the chromosphere), s is position and h_0 is the scale height ($\simeq 1.86 \times 10^7$ cm). See Section 2.2 for discussion of the magnetic field models used.

2.1.6 Limitations

Our simulations are test particle simulations, and therefore do not directly model large scale effects as can be done using hydrodynamic simulations, which treat the plasma as a whole, rather than looking at the cumulative effects of single particles. As a result, we are not able to include effects such as chromospheric evaporation, where photospheric and chromospheric plasma ablates and moves back up the loop as it is hit by fast electrons; nor can we model the propagation of waves in the plasma and their effects. Teriaca et al. (2003) observe the velocities of upward moving plasma as a result of chromospheric evaporation to be between 100 kms^{-1} and 160 kms^{-1} in chromospheric and coronal parts of a small pre-flare loop. Taking an average velocity of 130 kms^{-1} gives an evaporation timescale of

~ 100 sec for a loop of length 1.3×10^9 cm from footpoint to apex. This timescale is large enough that we are justified in not considering chromospheric evaporation - our test particles are all injected at time t = 0 sec, and all but a tiny fraction run out of energy well before 100 sec (from $\sim$78 sec for particles of initial velocity 1×10^{10} cms^{-1} to ~ 0.64 sec for low energy particles of initial velocity 1×10^9 cms^{-1}).

Due to limitations in computational power and storage space, we cannot run the simulations with as many particles for as long timescales as we would like, and running with smaller numbers can introduce statistical noise. We run simulations with as many particles and timesteps as is feasible, and we believe distortion from such statistical noise to be within acceptable limits. We must then, as a result, scale certain values up to represent realistic loop parameters (see Sections 3.1.1 and 4.1.1).

This limitation in the number of particles can also cause problems when it comes to increasing the background density. In certain situations, we wish to see the effect of higher background densities in order to test various physical scenarios, but increasing the density generally results in all the test particles running out of energy very quickly due to increased collisions. Using a continuous injection model where particles are injected steadily over time, as opposed to all at once (at $t = 0$), counteracts this problem.

2.2 Magnetic Field Models

In our simulations we have used two distinct types of magnetic field models. The first is a static field which converges across the chromosphere at either end, and a variation on this in which the field strength varies across the entire loop length. The second is an X-point magnetic field configuration, a more realistic model.

2.2.1 Basic Field Model

We consider a static magnetic field where the field strength is constant across the corona and increasing across the chromosphere to a maximum at the photosphere. The form of this field is as given in MacKinnon & Brown (1990):

$$B_s(s) = B_0 + \frac{(B_1 - B_0)}{(p_2 - p_1)} \cdot [p_2 x^{p_1} - p_1 x^{p_2}] \tag{2.18}$$

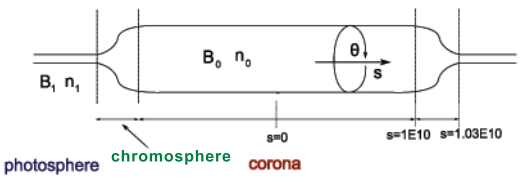

Figure 2.9: Basic magnetic field configuration. We assume symmetry in θ (particles can travel in both directions).

where $x = \frac{(|s|-s_0)}{(s_1-s_0)}$, B is the magnetic field strength in gauss, s is the distance along the field line from the origin (the looptop), s_0 is the position where the field strength begins to increase, s_1 is the position where the field strength reaches a maximum, and p_1 and p_2 determine the position at which the majority of the field strengthening occurs and how suddenly this happens, respectively. For this work, we consider the field to be constant in r (across the radius of the loop), so the magnetic field strength depends only on s. When dependence on both s and r are considered, this field satisfies the condition that $\nabla B = 0$.

We choose as our basic default configuration a constant coronal field strength of 100 G and a photospheric strength of 1000 G, with the increase occurring across the chromosphere (see Figure 2.10). A more realistic variation on this, created by varying the parameters s_0 and s_1, has a field strength which varies across the entire loop length (see Figure 2.11). This field model is a compromise between the simplicity of implementation that the basic model with constant coronal field strength provides, with the more physically accurate but also more difficult to implement X-point field model (see below).

The field convergence at either end creates a magnetic bottle, causing particles to be reflected and trapped in the loop. Magnetic mirroring occurs as a result of conservation of the magnetic moment:

$$\mu_m = \frac{\frac{1}{2}mv_\perp^2(s)}{B(s)} = const. \tag{2.19}$$

where $v_\perp$ is the component of the particle velocity perpendicular to the magnetic field. As the field strength increases, the perpendicular velocity increases, and correspondingly the parallel velocity decreases. When the field strength reaches a critical value, the parallel velocity is reversed and the particle is reflected.

Whether a particle escapes or is trapped by the magnetic mirror depends on its pitch angle. A particle will be trapped by the magnetic bottle if its pitch angle (μ) is greater than the loss-cone angle (α_0). The loss-cone angle is defined by the magnetic mirror ratio, R:

$$\alpha_0 = sin^{-1}\sqrt{\frac{1}{R}} \tag{2.20}$$

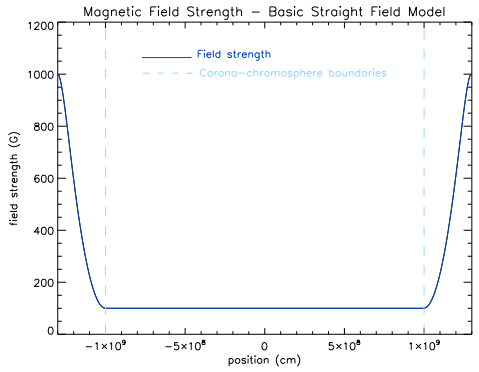

Figure 2.10: Magnetic field strength along the length of a loop with constant field in the corona (100G) increasing across the chromosphere to the a maximum at the photosphere (1000G), according to Equation 2.18 where $s_0 = 1 \times 10^9$ cm (the start of the chromosphere) and $s_1 = 1.3 \times 10^9$cm (the photosphere).

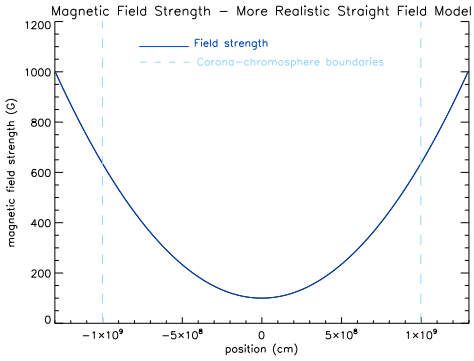

Figure 2.11: Magnetic field strength throughout the length of a loop, varying across the loop according to Equation 2.18 where $s_0 = 0$ cm (i.e. the looptop) and $s_1 = 1.3 \times 10^9$cm (the photosphere).

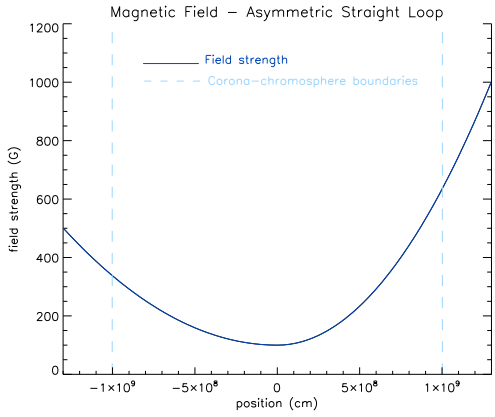

Figure 2.12: Magnetic field strength throughout the length of a loop, varying across the loop according to Equation 2.18 where $s_0 = 0$ cm (i.e. the looptop) and $s_1 = 1.3 \times 10^9$cm (the photosphere), and the photospheric field strength is different at each end (in this case, 500 G at the left 1000 G at the right).

where $R = \frac{B_M}{B_0}$, B_M being the maximum field strength (i.e. at the footpoint) and B_0 the field strength at the point of origin of the particle.

Thus, depending on the pitch angle of a particle at a given time, it can be trapped by the magnetic bottle, or it can escape and propagate down towards the photosphere. The ratio of trapped and precipitating particles has an effect on the resultant X-ray emission and loop heating, since trapped particles generally do not reach the chromosphere where significant hard X-ray emission can occur due to the increasing density.

2.2.2 X-Point Field

An X-point is a neutral point in a 2D magnetic field produced by two positive and two negative sources, symmetrical such that the field cancels in the middle creating a null point, i.e. a point of zero magnetic field. It is believed that magnetic reconnection can occur at an X-point. Considered in the field line description, this means that separate field lines of opposing polarity join and reform to create a new field line in a different configuration (see Figure 2.13). An X-point region can be taken as a simple model for the pre-flare field configuration. The magnetic field in an X-type neutral point region is described by[Priest & Forbes (2000)]:

$$\begin{aligned} B_x &= \frac{B_0}{L_0} y \\ B_y &= \frac{B_0}{L_0} \bar{\alpha}^2 x \end{aligned} \tag{2.21}$$

and the field lines are hyperbolic, described by

$$y^2 - \bar{\alpha}^2 x^2 = \frac{2L_0}{B_0} C \tag{2.22}$$

where B_0 is the magnetic field at the photosphere (the base of the loop), L_0 is the length scale over which the field is varying (i.e. the loop length), and C is a constant which determines the curvature of the line (we choose a default value of 2.25×10^{17}). $\bar{\alpha}^2$ determines the shape of the field: for $\bar{\alpha}^2 < 0$ the field lines are elliptical and the configuration is an O-type neutral point, for $\bar{\alpha}^2 > 0$ the field lines are hyperbolic and the configuration is that of an X-type neutral point, an X-point. For this work we consider only the case where $\bar{\alpha}^2 = 1$, which is an equilibrium, current-free X-point (since $\mathbf{j} = \frac{1}{4\pi}(\nabla \wedge \mathbf{B})$).

In our simulations we need to calculate the magnetic field strength at a given position along the magnetic loop. Figure 2.14 shows the field strength along the loop using this field model. Compare this to Figure 2.11 where the field strength also varies throughout the loop - the X-point field model produces a similar but slightly different field geometry. Note that the loop apex is no longer at the specified coronal field strength of 100G.

Within our simulations, the term for the calculation of μ (see Equations 2.9) includes the derivative of the magnetic field with respect to s, however for the X-point field configuration the equations describing the magnetic field strength (Equations 2.21) are in two dimensional Cartesian co-ordinates. The algebraic

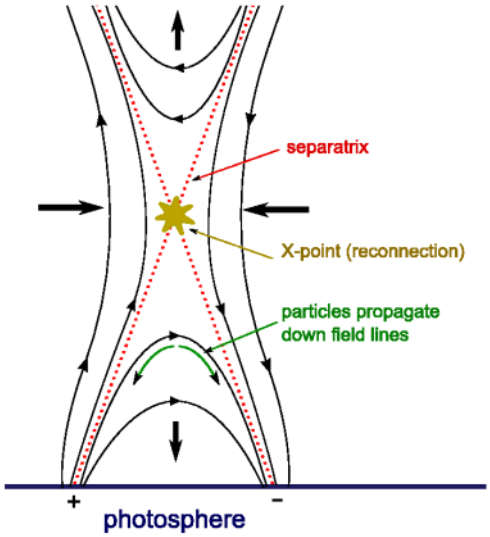

Figure 2.13: A simplified diagram of a basic X-point magnetic field configuration.

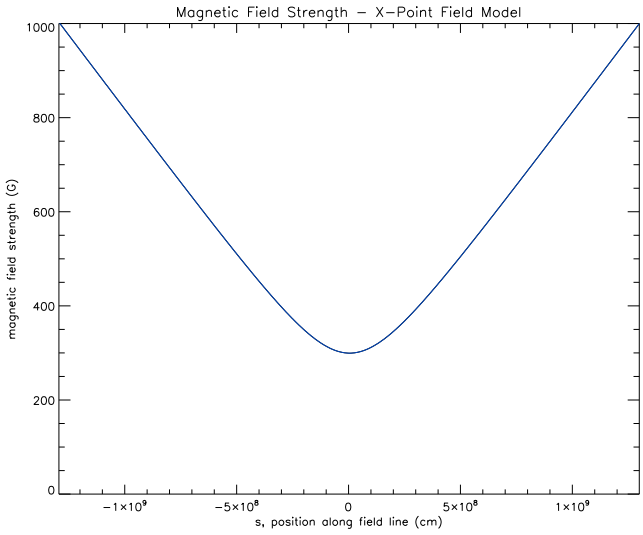

Figure 2.14: Magnetic field strength along a magnetic loop in an X-point configuration, as described by Equations 2.21. The x-axis of the graph is s, the axis of the field line, not x or y.

conversion from s to x, y is described by:

$$s = -\int_a^b \left(\frac{\left(\frac{2}{C}\right)^2 + t^2}{\left(\frac{1}{C}\right)^2 + t^2} \right)^{\frac{1}{2}} \frac{\mathrm{d}t}{t^2} \tag{2.23}$$

where $t = \frac{1}{x}$ and C is constant, as in Equation 2.22. This has the solution:

$$s = -\frac{1}{\left(\sqrt{\frac{2}{C}}\right)} G(\beta, q) + \frac{\sqrt{\frac{2}{C}}}{\frac{1}{C}} H(\beta, q) - \frac{\frac{2}{C}}{\left(\frac{1}{C}\right) a} \sqrt{\frac{\frac{1}{C} + a^2}{\frac{2}{C} + a^2}} \tag{2.24}$$

where $\beta = \arctan\left(\frac{\sqrt{\frac{2}{C}}}{a}\right)$, $q = \frac{\sqrt{\left(\frac{2}{C}\right) - \left(\frac{1}{C}\right)}}{\sqrt{\left(\frac{2}{C}\right)}}$ and $\sqrt{\left(\frac{2}{C}\right)} > \sqrt{\left(\frac{1}{C}\right)}$, $a > 0$. H is an elliptical integral of the second kind and G is a generalised hypergeometric series. This is a complex solution which would be difficult to implement within our programs, and would also significantly increase the run time required for calculations, therefore we decided it would be more feasible to calculate $\frac{\partial B}{\partial s}$ numerically throughout the program. To do this however, we require to first convert s (which is calculated by the program) into x, y and then numerically calculate the magnetic field derivative.

To calculate x, y from s we approximate the curved field line as many small straight segments. This approximation is acceptable as long as the segments are suitably small. We can then calculate Δx from Δs using the gradient, $\left(\frac{\partial x}{\partial y} = \frac{x}{y}\right)$, at some point x, y with the following trigonometrical relation:

$$\Delta x_1 = \Delta s_1 \cos\left[\tan^{-1}\left(\frac{x_1}{y_1}\right)\right] \tag{2.25}$$

This method requires a suitable choice of initial x and y since the gradient at the top of the loop is zero. Once x is determined, the corresponding y value can be calculated via the hyperbolic field line equation (Equation 2.22). Using these transformations and the fact that

$$\frac{\partial B}{\partial s} \simeq \frac{B(s+a) - B(s)}{a} \quad \text{(for } a \text{ very small)} \tag{2.26}$$

$\frac{\partial B}{\partial s}$ can be calculated using the following formula:

$$\frac{\partial B}{\partial s} \simeq \frac{\sqrt{(y - a_y)^2 + (x + a_x)^2} - \sqrt{y^2 + x^2}}{a} \tag{2.27}$$

where $a_x = a\cos\left[\tan^{-1}\left(\frac{x}{y}\right)\right]$ and $a_y = -a\sin\left[\tan^{-1}\left(\frac{x}{y}\right)\right]$.

2.2.3 Gradient and Curvature Drift

Charged particles in a magnetic field can be considered to be following a circular orbit around a point known as the 'guiding centre' of the particle. This guiding

centre drifts as the particle experiences forces from the magnetic field and other influences. If this drift is significant, it is possible for the particle to move away from the magnetic field line which we consider test particles to be moving along in our simulations, thus we must determine whether the effect is significant under the conditions we are considering.

Curvature drift results from the centrifugal force on a particle due to the curvature of the field line along which it is travelling, and is given by[Chen (1984)]:

$$\begin{aligned} \mathbf{v}_R &= \frac{1}{q}\left(\frac{\mathbf{F}_{cf} \wedge \mathbf{B}}{B^2}\right) \\ &= \frac{mv_{//}^2}{q}\frac{\mathbf{R}_c \wedge \mathbf{B}}{R_c^2 B^2} \end{aligned} \tag{2.28}$$

in SI units, where q is the charge on the test particle, $v_{//}$ is the component of velocity of the test particle parallel to the magnetic field, and $\mathbf{R}_c$ is the radius of curvature of the field line. Curvature drift is always accompanied by a gradient drift, since the field strength decreases with radius (as the field lines get further apart). The gradient drift is the result of changing magnetic field strength and is given by[Chen (1984)]:

$$\mathbf{v}_{\nabla B} = \frac{1}{2}\frac{mv_\perp^2}{q}\frac{\mathbf{R}_c \wedge \mathbf{B}}{R_c^2 B^2} \tag{2.29}$$

in SI units, where $v_\perp$ is the component of the particle's velocity perpendicular to the magnetic field. Combining these, we get a combined expression for gradient and curvature drifts:

$$\mathbf{v}_R + \mathbf{v}_{\nabla B} = \frac{m}{q}\frac{\mathbf{R}_c \wedge \mathbf{B}}{R_c^2 B^2}(v_{//}^2 + \frac{1}{2}v_\perp^2) \tag{2.30}$$

We would consider these effects to be significant if $|\mathbf{v}_R + \mathbf{v}_{\nabla B}| \gtrsim 0.1 v_p$ (v_p being the velocity of the test particle).

Let us consider an average particle of velocity 1×10^{10} cms^{-1} (1×10^8 ms^{-1}). Let us also consider it to have a pitch angle of 30°. This gives $v_{//} = 5 \times 10^7$ ms^{-1} and $v_\perp = 8.66 \times 10^7$ ms^{-1}. Setting $|\mathbf{v}_R + \mathbf{v}_{\nabla B}| = 0.1 v_p$, we then have:

$$\frac{\mathbf{R}_c \wedge \mathbf{B}}{R_c^2 B^2} \simeq 281.3 \quad \mathrm{m}^{-1}\mathrm{T}^{-1} \tag{2.31}$$

In the basic situation we consider, $\mathbf{B}$ has only a θ component in cylindrical coordinates, and $\mathbf{R}_c$ has only an r component. Therefore, $\mathbf{R}_c \wedge \mathbf{B} = \frac{1}{r}[r R_{cr} B_\theta \, . \, \hat{\mathbf{z}}]$ and hence we can write the condition for which curvature and gradient drift become significant as:

$$\frac{1}{R_c B} \gtrsim 281.3 \quad \mathrm{m}^{-1}\mathrm{T}^{-1} \tag{2.32}$$

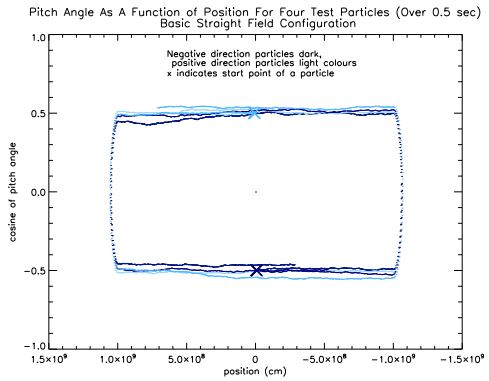

Figure 2.15: Plot of pitch angle against position for a 0.5 sec run for four test particles, all injected with initial velocity $2 \times 10^{10}\text{cms}^{-1}$. Two have an injection of 60^o (positive direction) and the other two 120^o (negative direction). The field model is a basic field converging at each end as shown in Figure 2.10, and the density is constant throughout at $1 \times 10^9\text{cm}^{-3}$.

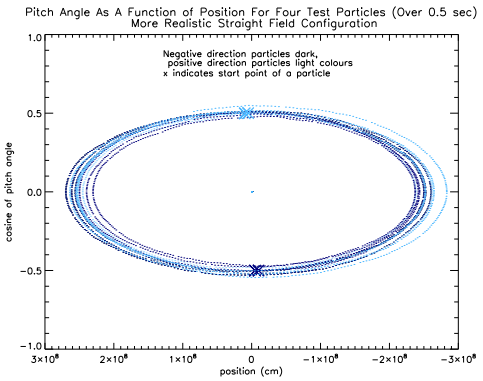

Figure 2.16: Plot of pitch angle against position for a 0.5 sec run for four test particles, all injected with initial velocity $2 \times 10^{10}\text{cms}^{-1}$. Two have an injection of 60^o (positive direction) and the other two 120^o (negative direction). The field model is a field varying throughout the length of the loop as shown in Figure 2.11, and the density is constant throughout at $1 \times 10^9\text{cm}^{-3}$.

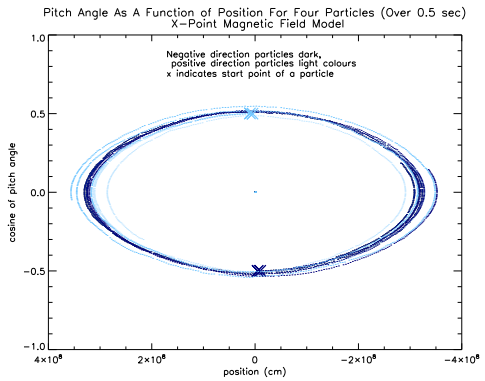

Figure 2.17: Plot of pitch angle against position for a 0.5 sec run for four test particles, all injected with initial velocity $2 \times 10^{10}\text{cms}^{-1}$. Two have an injection of 60^o (positive direction) and the other two 120^o (negative direction). The field model is an X-point configuration, as shown in Figure 2.14, and the density is constant throughout at $1 \times 10^9\text{cm}^{-3}$.

(in SI units). For a radius of curvature of 1×10^9 cm (1×10^7 m) a magnetic field of $\lesssim 3.6 \times 10^{-6}$ G ($\lesssim 3.6 \times 10^{-10}$ T) would be required. This is far smaller than any fields we consider, therefore we can safely disregard the gradient and curvature drifts of the particles.

2.2.4 Testing and the Effects of Field Models

We can show the effects of the different field configurations on the test particles

by plotting graphs of pitch angle as a function of position along the field for a number of test particles. Each of the fields described above includes a magnetic mirror effect, whereby the increasing magnetic field strength causes the test particles' parallel velocities to decrease and perpendicular velocity to increase, until the parallel velocity is reversed and the particle moves back along the loop. In Figures 2.15, 2.16 and 2.17, we plot the pitch angle of four test particles using our three standard field models as a function of position over a 0.5 sec run, keeping the density constant along the length of the loop in order to illustrate only the effect of the magnetic field in reflecting particles back along the loop. In normal situations, the density also increases across the chromosphere at the ends of the loop, resulting in further slowing and stopping of the particles.

We can see that in each case the four test particles are reflected at each end of the loop as a result of magnetic mirroring. The geometry of the magnetic field strength along the loop determines at what point a particle is reflected. In these graphs, all particles were injected at a cosine angle of ± 0.5 (60^o (forward direction) or 120^o (backward direction)) to the field line. Where the field strength is constant throughout the coronal section of the loop (Figure 2.15), the particles' pitch angles are only affected by random scattering (Coulomb collisions) with the background plasma until they reach the chromosphere, at which point the field strength increases rapidly, resulting in mirroring. In the two models where the field strength increases in throughout the loop (Figures 2.16 and 2.17) the particles are reflected before reaching the chromosphere. This means that particles with parameters the same as the ones shown in these tests are reflected before the density begins to increase, resulting in less pronounced emission and heating at the footpoints, and a lower particle loss rate from collisions (note, however, that other particles with different angles of injection will still reach the chromosphere). The position at which a particle is reflected depends on its initial pitch angle and velocity, and indirectly, Coulomb collisions, which alter the pitch angle and velocity.

Chapter 3

Hard X-Ray Emission

In this chapter we investigate the non-thermal hard X-ray emission produced by a beam of fast electrons moving along a magnetic loop and interacting with the background plasma. We look at the positions on the loop at which the strongest emission is produced for various physical parameters, and we also investigate the correlation between footpoint area and hard X-ray intensity.

3.1 Theory

Non-thermal hard X-ray emission is produced when fast electrons undergo collisions with ambient particles in the background plasma and are accelerated. The primary emission mechanism is large angle deflections between beam electrons and the lower energy electrons of the ionised background plasma. The energy lost by the fast electron in the collision is emitted as an X-ray photon of energy $\sim$ 20-100 keV. We note that there is also a component of the non-thermal emission produced by free-bound interactions between the beam electrons and ions such as iron in the background plasma (more so in the corona than the chromosphere, since the iron abundance in particular is higher in the corona), but in this work we treat the background plasma as fully ionised and do not consider free-bound emission. If it were included, we would expect to see higher photon emission levels at higher energies, above 10keV, for a given initial electron distribution. See Brown & Mallik (2007) for more work on this subject.

The X-ray intensity produced via non-thermal bremsstrahlung from a beam of fast electrons passing through a cold background plasma of constant density is given by[Brown (1971)]:

$$I(\epsilon) = n_p \int_{\epsilon}^{\infty} \sigma_{\epsilon}(E) v(E) f(E) \mathrm{d}E \tag{3.1}$$

in photons/sec/cm^2/unit ϵ, where n_p is the background plasma number density, $\sigma_\epsilon(E)$ is the electron-proton bremsstrahlung cross-section, $v(E)$ is the electron velocity corresponding to energy E, $f(E)$ is the electron distribution function, and ϵ is the X-ray photon energy. We use the Bethe-Heitler cross-section, given (in cgs units) by:

$$\sigma_\epsilon(E) = \frac{8}{3}\frac{r_0^2}{137}\frac{mc^2}{\epsilon E}\log\left[\frac{1+\sqrt{1-\frac{\epsilon}{E}}}{1-\sqrt{1-\frac{\epsilon}{E}}}\right] \tag{3.2}$$

where r_0 is the classical electron radius, m is the mass of the electron and c is the speed of light. We also divide this by $4\pi R^2$ (where R is the distance from the Earth to the Sun) in order to get the intensity per square centimetre at Earth. Thus, in our simulations (given also that for non-relativistic electrons, $v = \sqrt{\frac{2E}{m}}$, and we consider only the non-relativistic regime), the X-ray intensity (Equation 3.1) can be approximated by the sum:

$$I(\epsilon) \simeq \beta\frac{1}{\epsilon}\sum_{i=\epsilon}^{\infty}\frac{f(E_i)}{\sqrt{E_i}}\log\left[\frac{1+\sqrt{1-\frac{\epsilon}{E}}}{1-\sqrt{1-\frac{\epsilon}{E}}}\right]\Delta E \tag{3.3}$$

where $\beta = \frac{n_p}{137}\frac{2}{3}\frac{r_0^2}{R^2}\frac{\sqrt{2m}}{\pi}c^2$. Units are photons s^{-1} cm^{-2} (at Earth) erg^{-1}.

Our simulations record the electron distribution function (an energy histogram) at a number of positions over time along a magnetic field line, therefore we can calculate the intensity, $I(\epsilon)$, for a given ϵ throughout the length of a loop, and its evolution over time.

3.1.1 Scaling

Our programs are unable to run realistic numbers of particles due to computing power and storage limitations, therefore we must scale up results from the programs to represent realistic loop parameters. Specifically, we must apply a scaling factor to the number of counts in each histogram bin in the electron distribution, $f(E_i)$, as we sum over energy in Equation 3.3.

We assume an average realistic loop to have a flux of 10^{36} electrons per second (Holman et al. (2003)), which is a typical value found in a large flare, as calculated from observed chromospheric hard X-rays in the collisional thick-target model, and a maximum cross-sectional area, A_0, of 10^{18} cm^2 (Fletcher (2007)) at the apex. Thus we assume a value of 10^{18} electrons injected per second per square centimetre in an average loop. Thus the actual loop flux, F, can be written as:

$$F = 10^{18}A_0 \qquad \text{electrons s}^{-1} \tag{3.4}$$

Let the number of particles (electrons) in the simulation be denoted by P, and the length of time between counts be τ. Thus the simulated flux is $\frac{P}{\tau}$. Let the scaling factor be denoted by f. Then:

$$\begin{aligned} 10^{18} A_0 &= \frac{fP}{\tau} \\ \text{i.e.} \qquad f &= \frac{10^{18} A_0 \tau}{P} \end{aligned} \tag{3.5}$$

However, we must also multiply by an additional factor $\frac{A_s}{A_0}$ (where A_s is the area at position s), which arises because, as the field strength increases along the loop, the area decreases (since we assume B has no radial dependence - see Section 2.2.1 and also below). This factor compensates for the difference in area between the loop apex and position s. Thus the final scaling factor applied to each histogram bin is:

$$f = \frac{10^{18} \tau A_0 (\frac{A_s}{A_0})}{P} \tag{3.6}$$

The area A_s is calculated within the simulations by assuming the magnetic field strength is dependant only on s, the position along the field line, and has no radial dependence. This means that $A_i B_i = constant$ and thus:

$$A_s = \frac{A_{looptop} B_{looptop}}{B_s} \tag{3.7}$$

B_s is calculated as described in Section 2.2. The assumption that B has no radial dependence is not physically correct but is adequate for our purposes, since our simulations effectively model a particle moving along a single field line, then artificially scale this up to represent a loop of a specific cross-sectional area.

3.2 X-Ray Emission Throughout The Loop

Calculating the non-thermal X-ray emission as described above, we are able to investigate the emission over time from loops with various field and density configurations. We can plot the emission as a function of position along the loop or we can sum over a section of the loop as required. Thus we can investigate the emission from both looptop and footpoint sources as a function of time. By considering asymmetric loops, we can also investigate foopoint emission as a function of footpoint area, since field strength corresponds to loop area in our model.

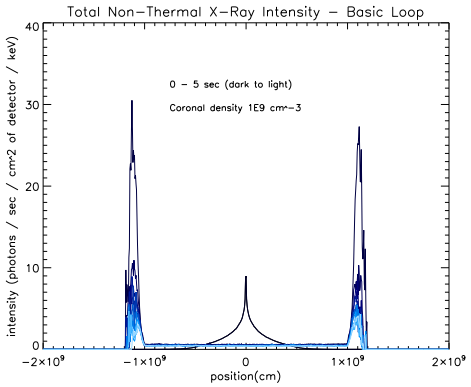

Figure 3.1: Non-thermal X-ray emission from a loop with a constant coronal magnetic field as depicted in Figure 2.10 over a time of 5 seconds (dark to light plots). Emission is from the loop cross-sectional area at each position, as seen by a detector at Earth, assuming a loop apex area of $1 \times 10^{18}\text{cm}^2$. The density model is that described by Equation 2.17, with a coronal density of 10^9 cm^{-3}. All particles are injected at $t = 0$, with pitch angles chosen from a uniform distribution between 0° and 90° to the field line in both directions, and initial velocities chosen from a power law distribution between 1×10^{10} cms^{-1} and 2×10^{10} cms^{-1}.

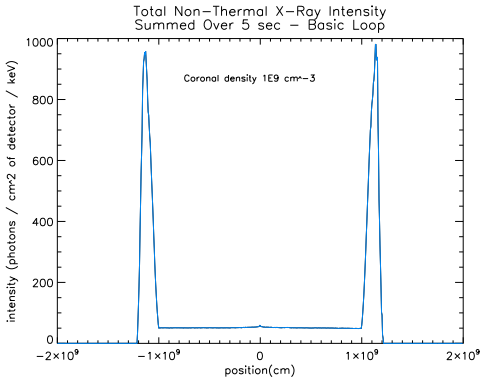

Figure 3.2: As Figure 3.1 but showing emission summed over 5 sec.

3.2.1 Basic Magnetic Loop Results

Uniform Coronal Magnetic Field

In Figures 3.1 and 3.2 we plot the hard X-ray intensity produced along a basic loop with magnetic field strength and density increasing only across the chromosphere at each end. We can clearly see that in this situation, the majority of emission occurs at the footpoints because there is no field convergence in the corona and hence almost all particles propagate at least as far as the chromosphere where higher densities result in higher emission. At these positions, the combination of increasing density (more Coulomb collisions) and, to a lesser extent, increasing magnetic field (slower parallel velocities) results in an increase in the instantaneous numbers of particles at the footpoints compared to the coronal regions of the loop and hence higher X-ray emission, since the intensity is strongly dependant on the electron distribution function. The intensity decreases over time as particles are scattered into the loss cone and lost, or run out of energy. The central peak seen at the earliest time in Figure 3.1 appears because at that early time the majority of the particles are still near the point of injection - they haven't had time to propagate to the footpoints.

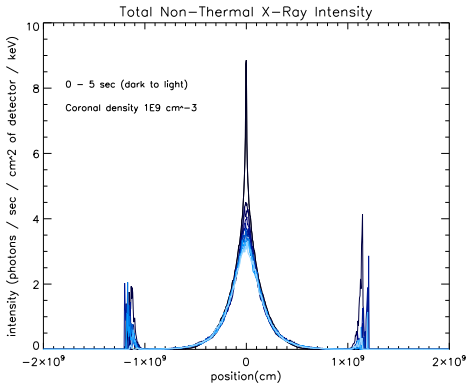

Figure 3.3: As Figure 3.1 but with a varying coronal magnetic field as depicted in Figure 2.11.

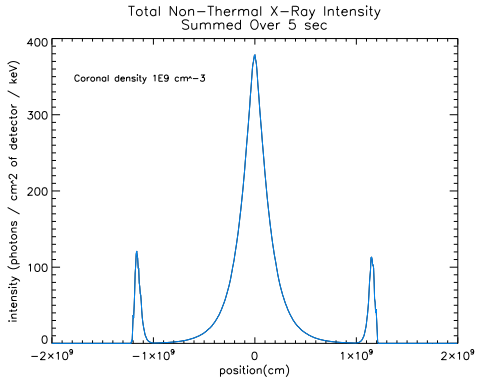

Figure 3.4: As Figure 3.3 but showing emission summed over 5 sec.

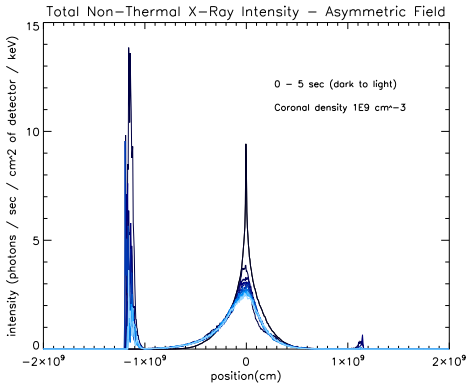

Figure 3.5: As Figure 3.3 but with an asymmetric magnetic field with minimum coronal field strength 100 G, left hand photospheric strength of 500 G and a right hand photospheric strength of 1000 G.

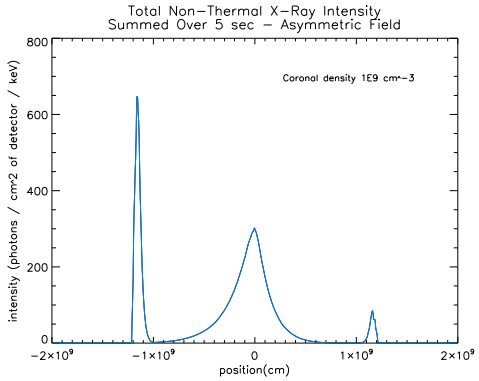

Figure 3.6: As Figure 3.5 but showing emission summed over 5 sec.

Variable Magnetic Field

In Figures 3.3 and 3.4, the magnetic field varies throughout the loop length. In this configuration, the peak position for X-ray emission is the looptop, in contrast to Figures 3.1 and 3.2. This is because the gradually increasing magnetic field results in particles being reflected over a wide range of positions in the corona as well as in the chromosphere. The position at which particles are reflected depends on their initial energy and pitch angle, and scattering. This magnetic bottle effect also traps particles for a longer period of time than the previous field model because large numbers do not reach the high density chromosphere as quickly. Although particles remain in the loop for longer, the peak intensities are smaller than in Figures 3.1 and 3.2 because in these, the majority of particles emit energy at the footpoints, where the density (and hence emitted intensity) is higher.

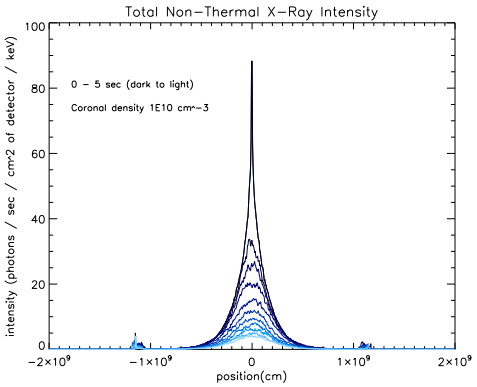

Figure 3.7: As Figure 3.3 but with a higher coronal density of 10^{10} cm^{-3}.

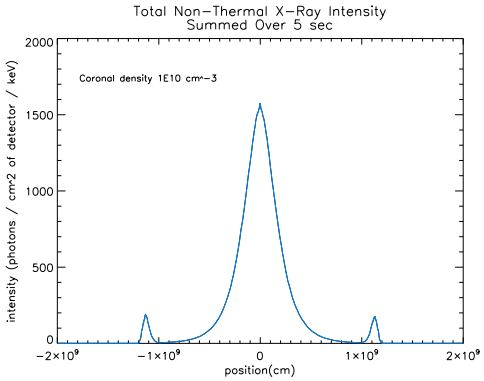

Figure 3.8: As Figure 3.7 but showing emission summed over 5 sec.

In Figures 3.5 and 3.6 we see the X-ray emission resulting from an asymmetric magnetic loop. This loop has a photospheric field strength of 500 G at the weak-field footpoint and 1000 G at the strong-field footpoint, with a minimum coronal strength of 100 G. This results in stronger emission at the weak-field footpoint as particles are able to propagate further in that direction before being reflected by the increasing field.

Increased Coronal Density

In Figures 3.7 and 3.8 we return to a symmetric loop with the field strength varying across the full loop length (shown in Figure 2.11) but with a higher coronal density of 10^{10} cm^{-3}. This increased density results in higher peak coronal intensity, but also changes the distribution of the emission slightly compared to the lower density case in Figures 3.3 and 3.4. The footpoint emission is less, relative to the central peak, because particles undergo more collisions in the increased density with the result that fewer particles reach the footpoints while at the same time increasing the intensity of the emission at other points thoughout the loop. Intensity decreases over time as particles are lost from the loop (see also Figures 3.19 and 3.20).

Continuous Particle Injection

In each case with all particles injected at $t = 0$ sec, particles are gradually lost from the loop as they run out of energy or are scattered into the loss cone. To compensate for this, we can simulate continuous particle injection, which we show in Figures 3.9 and 3.10 with parameters equivalent to those in Figures 3.7 and 3.8. In contrast to that case, the intensity continuous to increase with time as

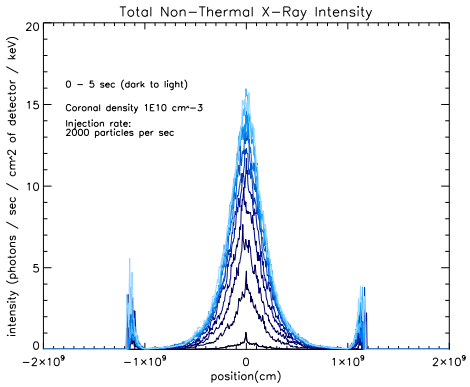

Figure 3.9: As Figure 3.7 but with continuous particle injection. Particle injection rate is 2000 particles per second.

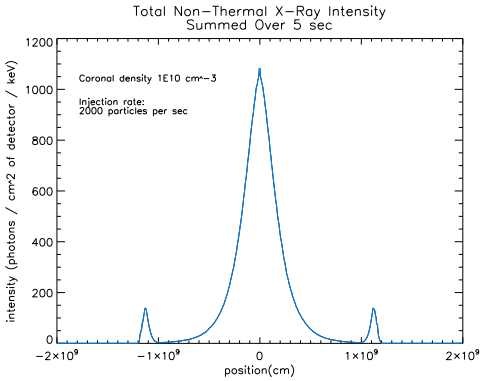

Figure 3.10: As Figure 3.9 but showing emission summed over 5 sec.

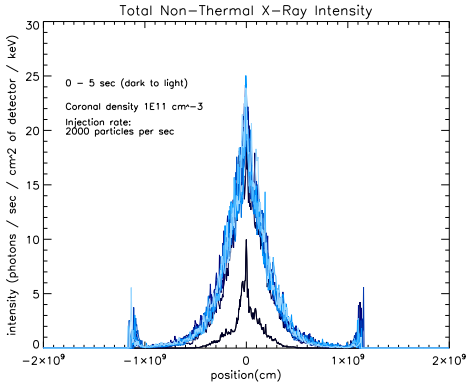

Figure 3.11: As Figure 3.9 but with a higher coronal density of 10^{11} cm^{-3}.

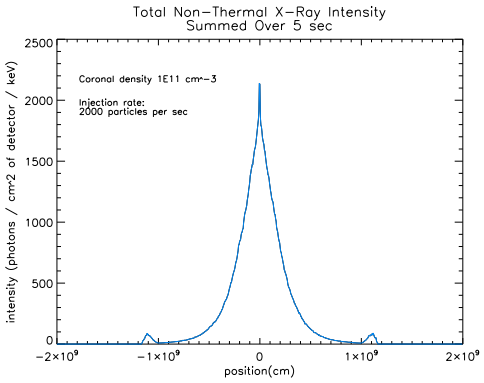

Figure 3.12: As Figure 3.11 but showing emission summed over 5 sec.

the number of particles in the loop increases.

If we increase the coronal density further to 10^{11} cm^{-3} (Figures 3.11 and 3.12), a steady-state solution is reached after approximately 1.5 seconds, at which point the particle injection rate equals the particle loss rate, as shown in Figure 3.14 where we plot the number of particles in the simulation over time. Once this steady-state is reached, the rate of hard X-ray intensity emission remains constant over time (Figure 3.13).

Intensity at Loop Apex and Footpoints As A Function of Time

In two of the simulations where particles are all injected at once, we see an early peak in intensity at one or both footpoints (depending on whether the loop is asymmetric or symmetric respectively), which rapidly decays. This is most pronounced in the basic model where the field and density increase only across the chromosphere (Figure 3.1). In this model, the footpoint intensity dominates

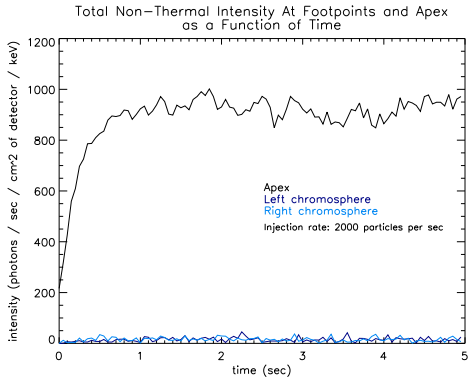

Figure 3.13: Plot of the intensities from the loop apex and chromosphere at each end as a function of time corresponding to Figure 3.11 showing the steady-state situation reached after approximately 1.5 sec.

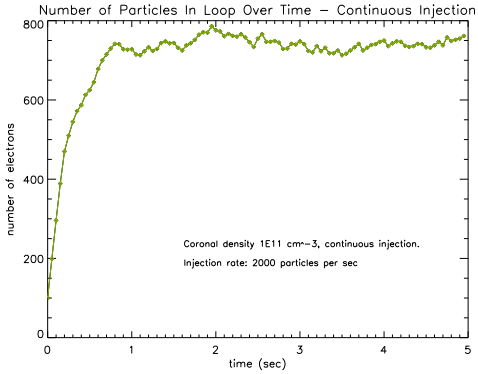

Figure 3.14: Plot of the number of particles in the loop over time corresponding to Figure 3.11.

the apex intensity at all times - we show the evolution of the intensities at the apex and footpoints in Figure 3.15, where the apex intensity is summed over 3000 km of loop centred on the apex, for a direct intensity comparison with the 3000 km width of the chromospheric regions. The other simulation where we see this effect is that with the asymmetric loop model where the field strength varies across the loop length, with a weaker photospheric value at the left footpoint. In this case, the early peak at the left (weaker field) footpoint initially dominates the central peak (and right footpoint), but it quickly decays and the central peak becomes the dominant source (see Figure 3.17). We do not see early foopoint peaks in any simulations with continuous injection, because the particles which cause the peaks are injected gradually over time in these simulations, rather than all at once. This footpoint peak effect is a result of all particles being injected at the same time. Initially we see "packets" of electrons moving back and forth along the loop but after a short time diffusion and Coulomb collisions spread the particles out along the loop.

These early bursts of footpoint intensity are caused by those particles whose initial pitch angles are within the loss cone, causing them to precipitate directly to the footpoints, where they are stopped by the increasing density. These particles still have high energies when they reach the footpoints, and release most of this energy as hard X-rays. We also see a secondary peak at the footpoints shortly after this which is caused by those particles which were initially reflected at the opposite footpoint and had pitch angles just outwith the loss cone. If we look at the number of particles left in the simulations over time (Figures 3.16 and 3.18), we see a sudden drop over approximately the first 0.15 seconds, which corresponds

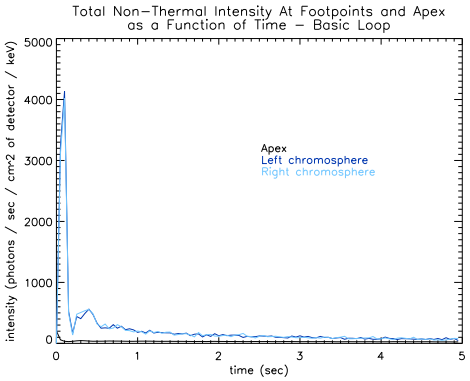

Figure 3.15: Plot of the intensities from the loop apex and chromosphere at each end as a function of time corresponding to Figure 3.1, showing an early peak at the footpoints.

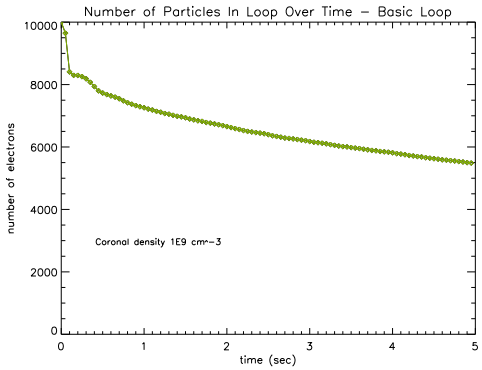

Figure 3.16: Plot of the number of particles in the loop as a function of time corresponding to Figure 3.1.

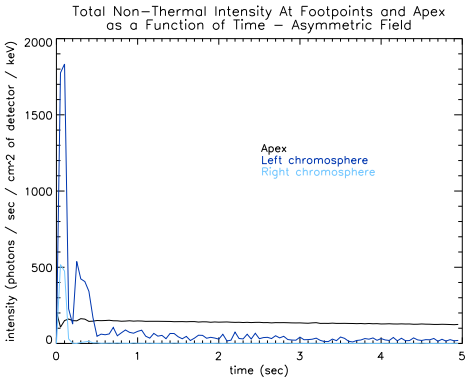

Figure 3.17: Plot of the intensities from the loop apex and chromosphere at each end as a function of time corresponding to Figure 3.5, showing an early peak at the left footpoint.

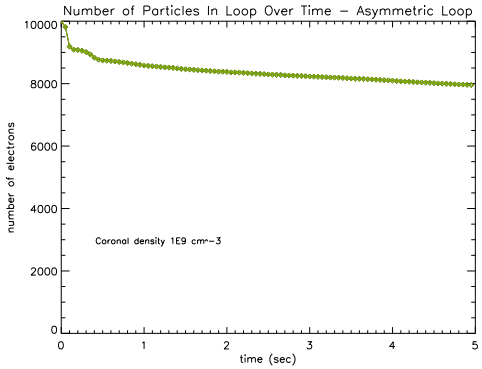

Figure 3.18: Plot of the number of particles in the loop as a function of time corresponding to Figure 3.5.

with the intensity peak at the footpoints and supports the theory that a small number of particles being lost very early in the simulations cause these peaks.

With increased coronal density, the early footpoint peak is lower than the intensity at the apex - the small number of particles still reach the footpoint early on, but the apex dominates as a result of the increased density (Figures 3.19 and 3.20).

In Figure 3.20 we are seeing three distinct phases of particles loss - the first 0.15 seconds shows a sudden loss as particles with initial pitch angles within the loss cone escape from the loop; up to approximately 1.8 seconds we are seeing only losses of particles which are scattered into the loss cone through Coulomb collisions; after this point, particles are also lost because they run out of energy. The energy loss time for particles in this increased density of 10^{10} cm^{-3} is within the timescale of the simulation - approximately 1.8 seconds corresponds to the

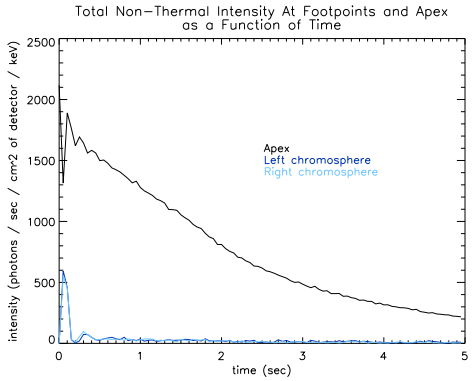

Figure 3.19: Plot of the intensities from the loop apex and chromosphere at each end as a function of time corresponding to Figure 3.7, showing the decrease in looptop intensity as particles are lost.

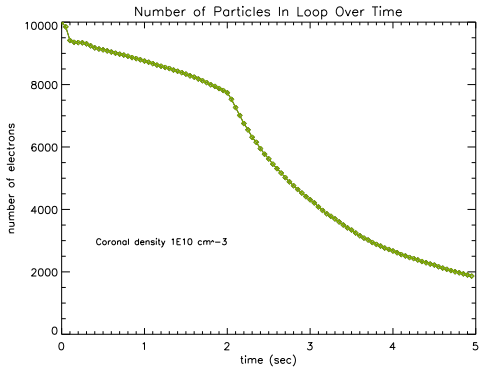

Figure 3.20: Plot of the number of particles in the loop as a function of time corresponding to Figure 3.7.

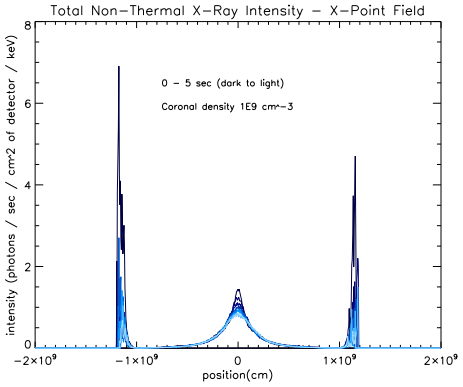

Figure 3.21: Non-thermal X-ray emission from a loop with an X-point field configuration as depicted in Figure 2.13 over a time of 5 seconds (darkest to lightest plots). Emission is from the loop cross-sectional area, as seen by a detector at Earth at each position, assuming a loop apex area of 1×10^{18} cm^2. The density model is that described by Equation 2.17, with coronal density 10^9 cm^{-3}. All particles are injected at $t = 0$, with pitch angles chosen from a uniform distribution between 0° and 90° to the field line in both directions, and initial velocities chosen from a power law distribution between 1×10^{10} cms^{-1} and 2×10^{10} cms^{-1}.

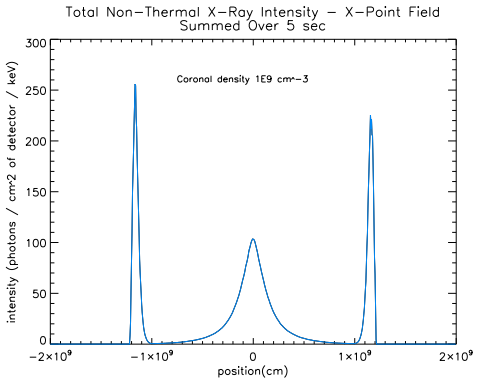

Figure 3.22: As Figure 3.21 but showing emission summed over 5 sec.

energy loss time for the particles with the lowest initial energies (1×10^{10} cms^{-1}).

3.2.2 X-Point Magnetic Loop Results

In Figures 3.21 and 3.22 we see the hard X-ray emission from a loop with an X-point magnetic field configuration (see Section 2.2.2). It has a density profile as described by Equation 2.17. We see a roughly similar X-ray distribution to that produced by the more basic magnetic field used in the previous section with

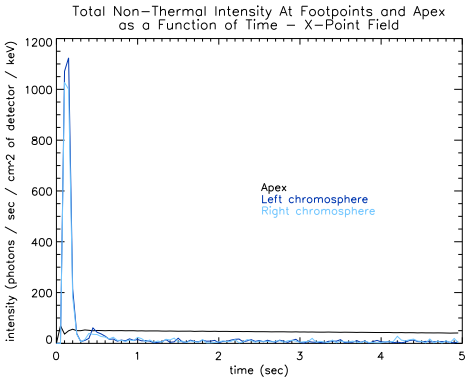

Figure 3.23: Plot of the intensities from the loop apex and chromosphere at each end as a function of time corresponding to Figure 3.21, showing an initial peak at the footpoints.

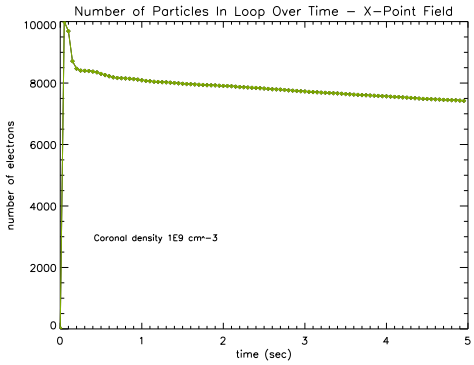

Figure 3.24: Plot of the number of particles in the loop corresponding to Figures 3.21 and 3.22 as a function of time.

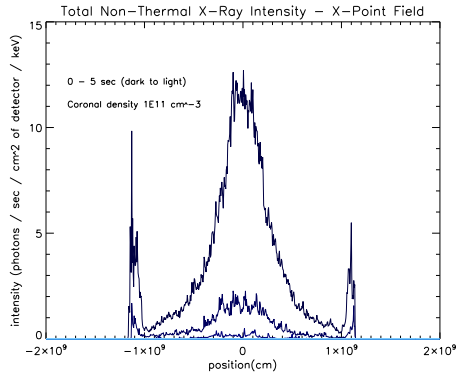

Figure 3.25: As Figure 3.21 but with a higher coronal density of 10^{11} cm^{-3}.

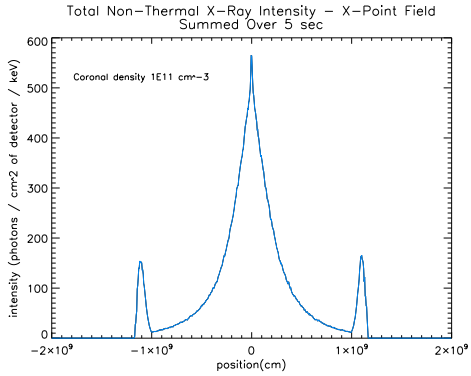

Figure 3.26: As Figure 3.25 but showing emission summed over 5 sec.

similar parameters (see Figures 3.3 and 3.4), because the magnetic field strength along the loop is similar (compare Figures 2.11 and 2.14) and all other parameters the same.

With this field configuration we see a maximum peak in the X-ray emission from the footpoints at the early time of approximately 0.15 seconds (see Figure 3.23), similar to those seen in the field models in the previous section. Again, this corresponds to those particles with initial pitch angles suitably parallel to the field to allow them to reach the footpoints early on, which we can see in Figure 3.24.

Increased Coronal Density

In Figures 3.25 and 3.26 we see the same model but with an increased coronal density of 10^{11} cm^{-3}. This increase in density leads to an increases the intensity and width of the central peak compared to the footpoints as well as a higher

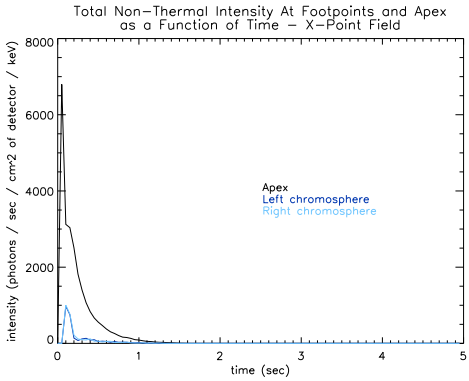

Figure 3.27: Plot of the intensities from the loop apex and chromosphere at each end as a function of time corresponding to Figure 3.25, showing the decay in emission as all particles are lost from the loop due to the high density.

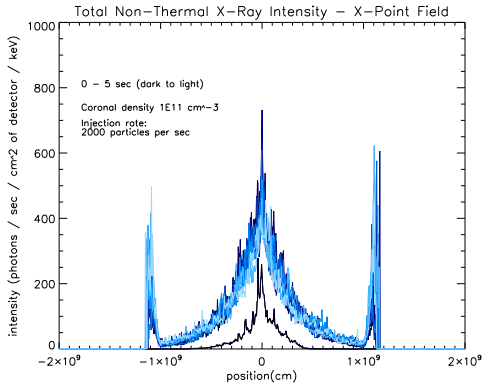

Figure 3.28: As Figure 3.25 but with continuous particle injection. Particle injection rate is 2000 particles per second.

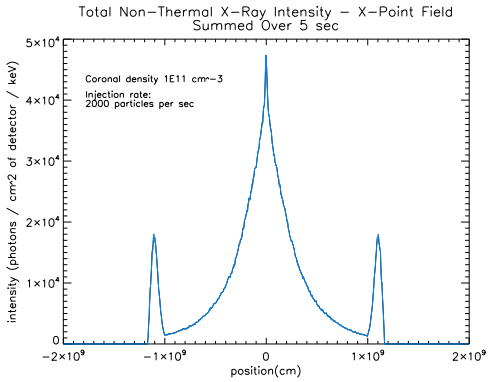

Figure 3.29: As Figure 3.28 but showing emission summed over 5 sec.

overall intensity. This is because the higher density causes the test particles to undergo more collisions throughout the loop than previously, resulting in higher coronal emission and fewer particles reaching the footpoints, and those that do having lower energies. In this situation, the early peak at the footpoints is dwarfed by the apex peak, which is consistently larger due to the higher density. In this model, all particles are lost from the loop by approximately 1.5 seconds because of the high density, causing the emission to drop to zero (see Figure 3.27).

Continuous Particle Injection

In Figures 3.28 and 3.29 we see the same X-point field configuration (with the high coronal density of 10^{11} cm^{-3}) but with continuous particle injection. Now the intensity does not decrease as much over time since injected particles replace

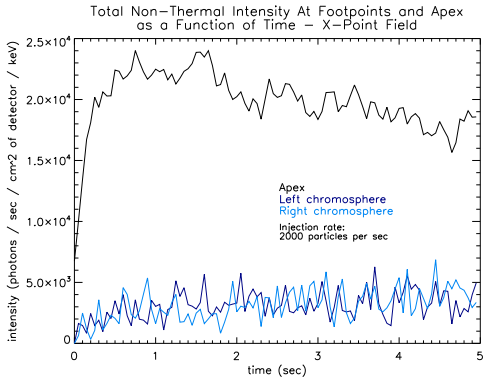

Figure 3.30: Plot of the intensities from the loop apex and chromosphere at each end as a function of time corresponding to Figure 3.28.

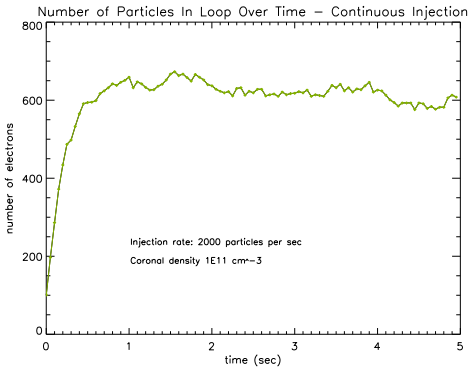

Figure 3.31: Plot of the number of particles in the loop corresponding to Figures 3.28 and 3.29 as a function of time.

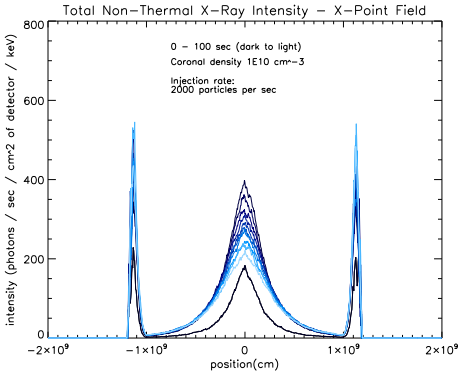

Figure 3.32: As Figure 3.28 but for a longer time interval of 100 sec and with a lower coronal density of 10^{10} cm^{-3}.

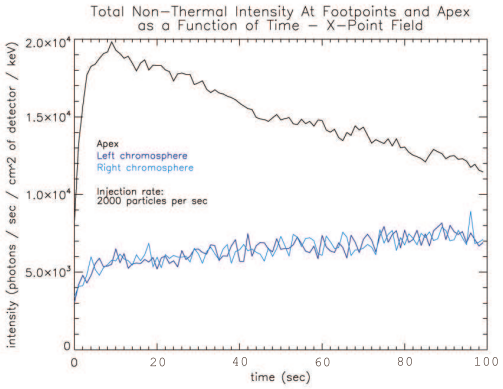

Figure 3.33: Plot of the non-thermal X-ray intensities from the loop apex and chromosphere at each end as a function of time corresponding to Figure 3.32.

those lost (Figure 3.30). This model reaches an almost steady-state situation after approximately 0.8 seconds (Figure 3.31), but with the X-point field configuration, the particle loss rate is very slightly higher than the injection rate compared to the equivalent basic field model (Figure 3.14), resulting in a very slight decrease in the number of particles (and hence overall intensity) after ∼0.8 sec.

Longer Time Interval Results

We now show results from a continuous injection model with coronal density 1×10^{10} cm^{-3}, run for a longer time of 100 sec. In Figure 3.32 we show the evolution of non-thermal X-ray emission from this simulation, and in Figure 3.33 we show the emission from the peak and footpoints as a function of time. We can see that in this situation, the emission peaks at the looptop at approximately 5 sec then decreases, whereas in the chromosphere the intensity continues to

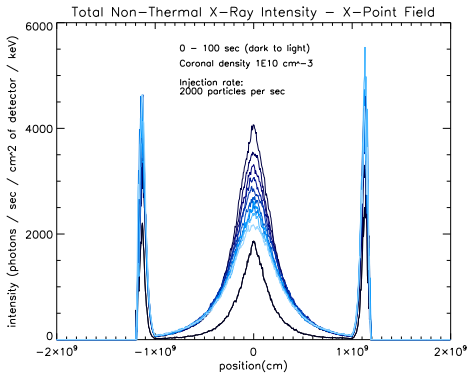

Figure 3.34: As Figure 3.32 but with a higher electron flux of 10^{37} electrons s^{-1} cm^{-2}.

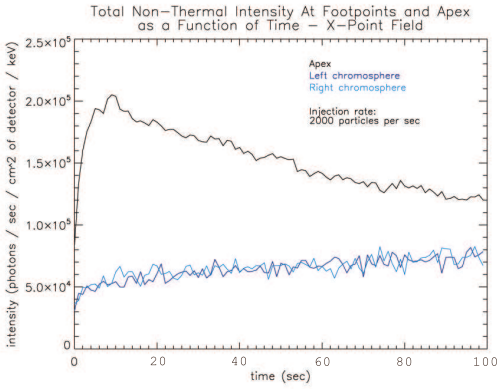

Figure 3.35: Plot of the non-thermal X-ray intensities from the loop apex and chromosphere at each end as a function of time corresponding to Figure 3.34.

increase steadily. This increase continues because as particles lose energy, they are scattered into the loss cone and propagate out of the magnetic bottle and into the high density regions of the chromosphere where they are stopped. As this loss progresses, there are fewer and fewer particles trapped in the loop and hence the looptop emission decreases (see Figure 4.29 for a plot of the number of particles in this simulation as a function of time).

If we increase the electron flux from 10^{36} to 10^{37} electrons s^{-1}, we see higher non-thermal X-ray emission, as would be expected - see Figures 3.34 and 3.35. Increasing the flux to represent a loop with a higher flux of particles alters the scaling factors we use (see Section 3.1.1).

3.2.3 Conclusions

Our results indicate that a strong looptop hard X-ray source is obtained when the injected electrons are high energy (non-relativistic) with uniformly distributed initial pitch angles, the electron flux is high (approaching the upper limits of calculated values) and the density is high, but not excessively so. The parameters in this situation are at the upper bounds of observed active region loops, and without these values, the footpoint emission will dominate. This concurs with observations, which indicate that strong looptop sources are not the norm, and are only observed in some flares. We would therefore conclude that these are flares with more extreme parameters such as described here.

3.3 Footpoint Emission

In this section we investigate the hard X-ray emission at loop footpoints as a function of footpoint area. We use these results to look for a correlation between hard X-ray intensity and footpoint size, which is complementary to work done by Schmahl et al. (2006) in which they investigate the relationship between footpoint area and emission intensity from RHESSI hard X-ray observations.

In these simulations we use a field model of the type shown in Figure 2.12. In this model, the field strength varies throughout the loop length and the density is as described in Equation 2.17 unless stated otherwise. We calculate the X-ray emission from the footpoints in asymmetric fields, holding the photospheric field strength constant at 1000 G at the stronger (right) footpoint and varying it at the weaker footpoint from 1000 G to 200 G. Varying the field in this way effectively creates different footpoint areas, since $A_{looptop}B_{looptop} = A_sB_s$ (see Section 3.1.1). Thus we are able to investigate the hard X-ray intensity as a function of footpoint area.

We define the footpoint intensity to be the intensity emitted by the chromosphere as a whole, a distance of 3000 km, since current observational capabilities in the X-ray regime are not able to resolve more detail than this. The following data are not time resolved.

In Figure 3.36 we show the emission from the whole loop for various weaker (left-hand) photospheric field strengths, assuming an apex loop area of 10^{18} cm^2, and in Figure 3.37 we show only the emission from the footpoints of the same loop. The colour coding indicates the changing field strength at the weaker footpoint. In this model, the coronal density is 10^9 cm^{-3}.

In Figure 3.38 we plot the chromospheric intensity overall all photon energies as a function of loop area. This graph uses data from the weaker field footpoint only - emission at the stronger field footpoint remains almost constant because the field strength is fixed there. The small amount of variation in intensity at the stronger footpoint is a result of the change in the weaker footpoint strength affecting the number of particles in the simulation over time by changing the trapping and precipitation rates, and hence affecting the number of particles that reach the stronger footpoint.

We can also plot the intensity in specific X-ray photon energy bands. We choose the bands 6-12 keV, 12-25 keV, 25-50 keV and 50-100 keV, to correspond with some of the bands frequently used in analysis of data from the RHESSI satel-

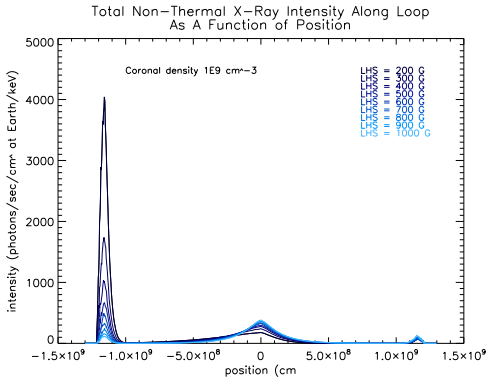

Figure 3.36: Non-thermal X-ray emission from a loop with field increasing across the loop length and density increasing across the chromosphere from a coronal value of 10^9 cm^{-3}. The magnetic field is as shown in Figure 2.11 but the right footpoint field strength is held constant at 1000 G and the left is varied from 200 G to 1000 G. The density model is that described by Equation 2.17, with a coronal density of 10^9 cm^{-3}. All particles are injected at $t = 0$, with pitch angles chosen from a uniform distribution between 0° and 90° to the field line in both directions, and initial velocities chosen from a power law distribution between 1×10^{10} cms^{-1} and 2×10^{10} cms^{-1}.

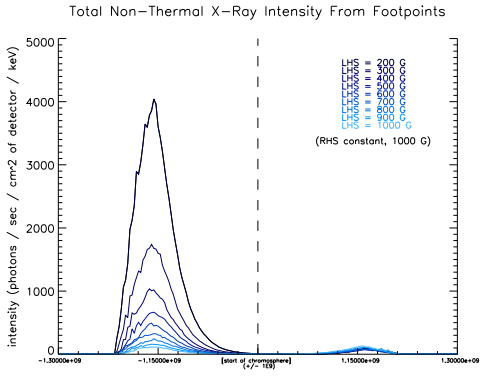

Figure 3.37: Emission from the chromospheric regions only for the loop shown in Figure 3.36.

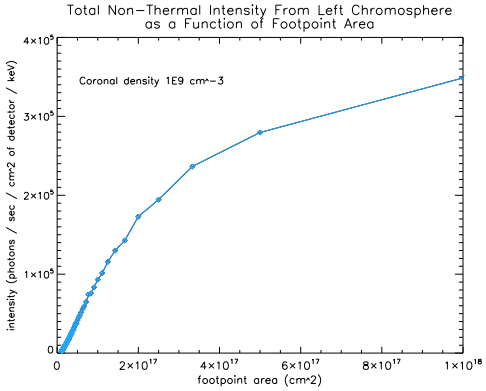

Figure 3.38: Overall emission (from all photon energies) from the weaker field chromospheric region of the loop depicted in Figure 3.36 as a function of area. Intensity is summed across the chromosphere (3000 km), and area refers to the footpoint area at the photosphere.

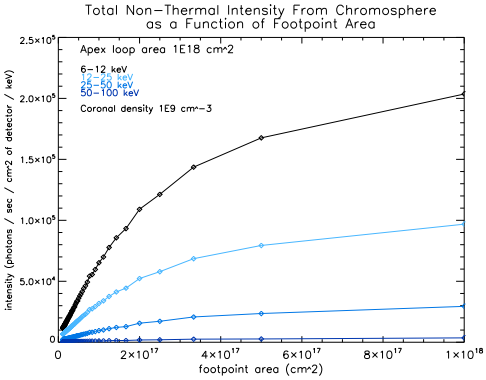

Figure 3.39: Emission from the weaker field chromospheric region of the loop depicted in Figure 3.36 in specific energy bands as a function of area. Intensity is summed across the chromosphere (3000 km), and area refers to the footpoint area at the photosphere.

lite. In Figure 3.39 we show the intensity across the weaker field chromosphere in each of these bands as a function of footpoint area. We can see from this plot that the highest intensities are always in the lower photon energy bands, indicating that emission from the much more abundant lower energy electrons dominates, although high energy electrons also produce a large amount of emission at low photon energies since the intensity is proportional to the inverse of the photon

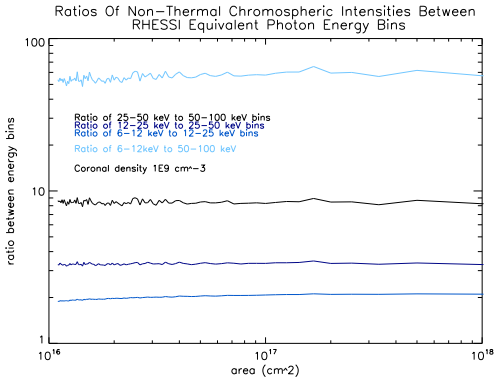

Figure 3.40: Log-log plot of the ratios between counts in photon energy bins corresponding to Figure 3.39.

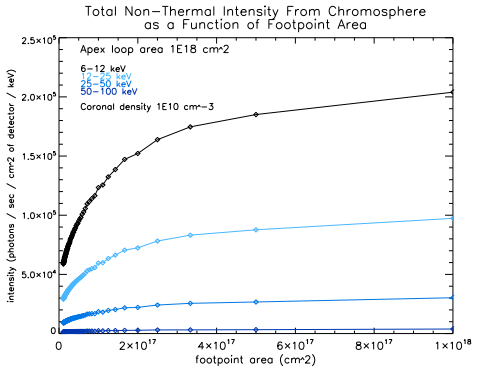

Figure 3.41: Emission from the weaker field chromospheric region in specific energy bands as a function of area of a loop equivalent to that shown in Figure 3.36 but with increased coronal density of 10^{10} cm^{-3}. Intensity is summed across the chromosphere (3000 km), and area refers to the footpoint area at the photosphere.

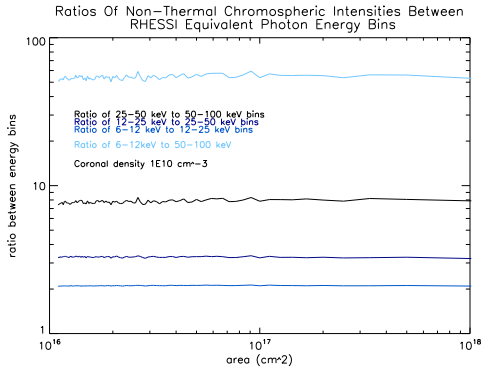

Figure 3.42: Log-log plot of the ratios between counts in photon energy bins corresponding to Figure 3.41.

energy (see Equation 3.3). If we plot the ratios between these energy bands in a log-log plot (Figure 3.40), we see that the relationship between intensity and footpoint area is consistant for each band - there is no change in the dominant emission band (and hence dominant emitting electrons) as foopoint area changes, indicating that at these energies, the energy-dependant effect of collisional scattering of electrons into the loss-cone is negligible.

In Figure 3.41 we show the chromospheric intensities as a function of loop area as above but with an increased coronal density of 10^{10} cm^{-3}. In Figure 3.42 we see the corresponding ratios between the energy bands in a log-log plot. With increased density, emission at the footpoints decreases - particles undergo more collisions higher in the loop, with fewer reaching the footpoints, and those that

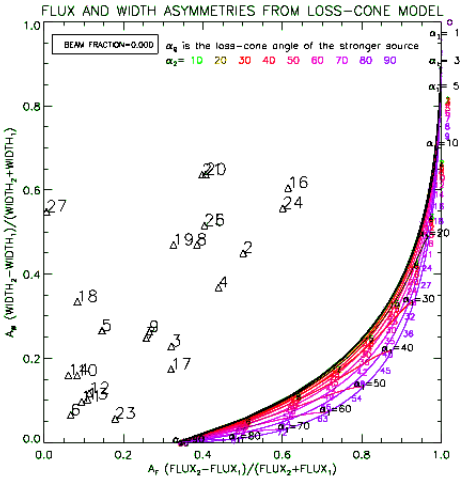

Figure 3.43: Figure of footpoint width and intensity asymmetries with scattering timescales $\gg$ mirroring timescales (no scattering effects) from Schmahl et al. (2006). Solid lines are theoretical lines of constant loss cone angle, square data points are observations.

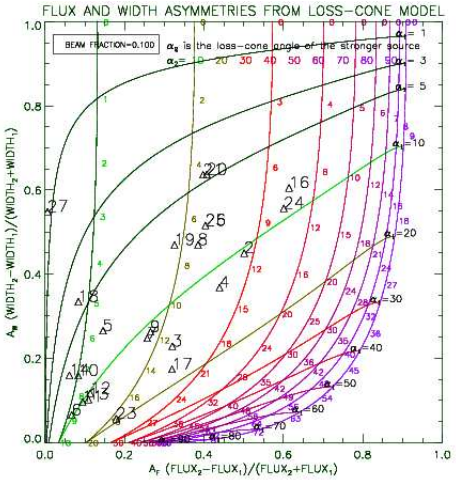

Figure 3.44: Figure of footpoint width and intensity asymmetries with scattering timescales $\ll$ mirroring timescales (strong scattering) from Schmahl et al. (2006). Solid lines are theoretical lines of constant loss cone angle, square data points are observations.

do have lower energies since it has taken them longer to get that far along the loop. This is reflected in the lower intensities seen from the chromosphere as a function of area, but despite the lower overall intensities, the same relationships hold true - the dominant emission is seen in lower energy bands, and the ratio between each energy band is largely independent of area.

Schmahl et al. (2006) found from observations that larger footpoints produce brighter X-ray emission. They modelled the relationship between footpoint pair widths and hard X-ray intensities, and found that their analytical model without scattering did not match observations, but when strong scattering was included the relationship between footpoint pair widths and intensities corroborated the observed data (Figures 3.43 and 3.44). Our simulations confirm that larger footpoints produce higher hard X-ray intensities (e.g. Figures 3.39 and 3.41), and we can also plot the footpoint width and intensity asymmetries in the same way as Schmahl et al. (2006) - Figure 3.45. The quantity"flux" in Schmahl et al. (2006) corresponds to our quantity "intensity", both being measured in photons sec^{-1} cm^{-2} (when summed over photon energy).

Schmahl et al. (2006) used analytical models to create the theoretical curves shown in Figures 3.43 and 3.44. In Figure 3.43 they show the observed asymmetries (square data points), and their theoretical asymmetries (solid curves) where the scattering timescale is much larger than the mirroring timescale, which effectively represents the case where pitch angle scattering is insignificant. In Figure

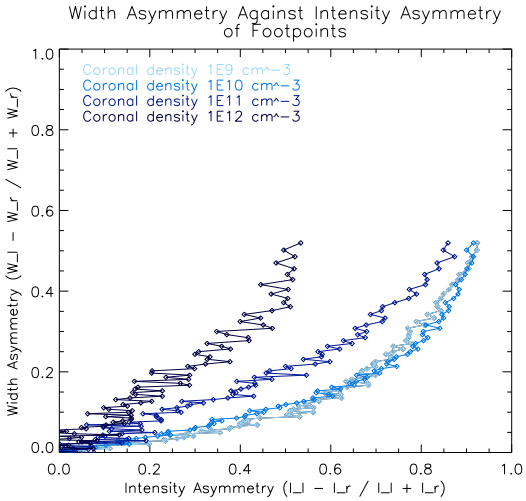

Figure 3.45: Plot of the asymmetries of footpoint widths and intensities in loops with varying coronal densities.

3.44 they include strong pitch angle scattering, where the scattering timescale is much less than the mirroring timescale and scattering plays a key role. Our simulations are midway between these two regimes, in that they include scattering, but not to the same degree as the strong scattering model in Figure 3.44. Furthermore, our simulations also include energy loss (which of course must accompany the pitch angle) with the scattering, which their models do not.

In Figure 3.45 we show results from our simulations using the field model as described previously in this section, with four different coronal densities. We can see that with the lowest coronal density our data more closely matches the model from Schmahl et al. (2006) with insignificant scattering and does not approach the observational data, but as the coronal density increases, it approaches the observed data, and begins to move into the regime of strong pitch angle scattering. Our highest density model (10^{12} cm^{-3}) is the closest match to the observed footpoint-intensity values as depicted by square data points in Figures 3.43 and 3.44, and shows a noisier distribution of points than the analytical results produced by Schmahl et al. (2006). This is because our data includes particle energy loss through pitch angle scattering, which the analytical model does not.

3.3.1 Conclusions

As our data begins to approach the observational data, we can conclude that the model we are using is a reasonable representation of non-thermal X-ray emission from a magnetic loop. It also shows that the higher coronal density of 10^{12}

cm^{-3} better describes the observed data used by Schmahl et al. (2006), however, choosing a density this high means the particles are more rapidly stopped through collisions and very few reach the chromosphere to produce footpoint emission (see, for example, Figures 3.7 and 3.8, and 3.11 and 3.12). This would indicate that a large amount of pitch angle scattering is required to match the observed data, but that some mechanism other than Coulomb collisions must be required, since with Coulomb collisions alone, very little footpoint emission would be seen at such high coronal densities.

Chapter 4

Collisional Heating of Magnetic Loops

In this chapter, we consider the heating of a loop by electrons accelerated in a flare, calculating the temperature evolution as a function of time and position, and it's dependence on the parameters of the beam and the ambient plasma. This study is motivated by observations of magnetic loops heated to high temperatures in active regions which show temperatures as high as 10 to 20 MK in the corona in the early stages of flares, cooling to several MK, as observed in extreme ultraviolet by the TRACE and Hinode satellites, which in turn results in thermal X-ray emission from the heated plasma.

4.1 Theory

As a beam of fast electrons passes through a cold background plasma, the electrons undergo Coulomb collisions with the particles in the plasma. In doing so, they lose energy, which is transferred to the volume of background plasma though which the electron passed. These small gains in energy accumulate and lead to an overall increase in the temperature of the background plasma. At the same time, the background plasma loses energy through radiative and conductive cooling.

In terms of losses, there is also line emission from ionised iron at a peak of approximately 6.7 keV, which becomes stronger as temperature increases. We do not directly simulate line emission here, but the relative abundancies of impurities in the ionised hydrogen plasma are included in the radiative loss function (Equation 4.4).

4.1.1 Heating and Radiative Cooling

Heating Through Collisional Energy Deposition

We consider the background plasma to be fully ionised hydrogen and treat the particles in it as stationary compared to the beam electrons (a cold plasma approximation). In each collision the test particle (electron) transfers energy to the background plasma - given that $E = \frac{3}{2}nkT$, we assume that this is immediately redistributed amongst the plasma, leading to a temperature increase, since the thermal collisional timescales are short under coronal conditions. We do not calculate the energy deposited during every collision because of the nature of our simulations (it would take too long), instead we calculate the energy lost by the test particle over a short time interval, which is approximately equivalent to the energy deposited into the background plasma through collisions over this time (a small percentage is also lost in other forms of emission such as radio waves).

The energy deposited by one particle must be scaled up to represent the energy deposited by the number of particles in a realistic loop. To do this, we multiply the energy deposited by one particle, ΔE, by a scaling factor, f.

We assume a realistic loop to have a flux of 10^{36} electrons per second (Holman et al. (2003)) and a maximum cross-sectional area, A_0, of 10^{18} cm^2 (Fletcher (2007), private communication) at the apex, thus the actual loop flux, F, can be written as:

$$F = 10^{18} A_0 \qquad \text{electrons s}^{-1} \tag{4.1}$$

Let the number of electrons in the simulation be denoted by P, and the length of time between calculations of energy deposition be τ. Thus the simulated flux is $\frac{P}{\tau}$. Then:

$$10^{18} A_0 = \frac{fP}{\tau}$$

$$\text{i.e.} \qquad f = \frac{10^{18} A_0 \tau}{P} \tag{4.2}$$

However, we must also multiply by an additional factor $\frac{A_s}{A_0}$, which arises because, as the field strength increases along the loop, the area decreases (since we assume B has no radial dependence - see Section 2.2.1). This factor compensates for the difference in area between the loop apex and position s. Thus the scaling factor applied to the energy deposited is:

$$f = \frac{10^{18} \tau A_0 (\frac{A_s}{A_0})}{P} \tag{4.3}$$

The energy deposited is spread out over the number of position bins through which the particle depositing the energy has passed in the time interval elapsed between calculations of temperature deposition.

Radiative Losses

At the same time as it is being heated, the plasma is also losing heat via radiation. The radiative loss rate is described by[Aschwanden (2004)]:

$$\begin{aligned} E_R &= n_e n_p \, \alpha_{FIP} \, \Psi(T) \\ &\simeq n_e^2 \Psi(T) \quad \text{ergs cm}^{-3} \text{ s}^{-1} \end{aligned} \tag{4.4}$$

for optically thin plasmas, where T is the current temperature, $\Psi(T)$ is the radiative loss function and α_{FIP} is a correction factor for abundance enhancements in the corona compared to the chromosphere due to the FIP (First Ionisation Potential) effect.

The energy lost by the plasma, E_R, must be scaled so that it is in the same units as the energy deposited in order to calculate the net change in energy. To do this, we first multiply E_R by the volume of one position bin, V (the bin width multiplied by the area of the loop at that point), and the time elapsed between calculations, τ, to get the energy lost per bin per calculation timestep. This is an approximation required by the nature of the simulations, whereas in reality the energy loss is a collective effect determined by the temperature. Since we are making this energy loss calculation for each particle that runs through the simulation, we must divide by the number of particles in the simulation in order to compare with the energy deposited by one particle. Hence the scaling factor applied to the energy radiatively lost during the passage of one particle through the volume V is:

$$\frac{10^{18} \tau V}{P} \tag{4.5}$$

We use approximations for the radiative loss function from Rosner et al. (1978). For the most common temperature ranges we expect to see, these are:

$$\begin{aligned} \Psi(T) &\simeq 10^{-21.94} && (10^{5.75} < T < 10^{6.3} K) \\ \Psi(T) &\simeq 10^{-17.73} \, T^{-2/3} && (10^{6.3} < T < 10^{7} K) \end{aligned} \tag{4.6}$$

We note that there is a small discontinuity at the intersection of these two approximations (see Figure 4.1) but this has no significant effect on the results. We also continue to use the latter approximation for temperatures greater than 10^7

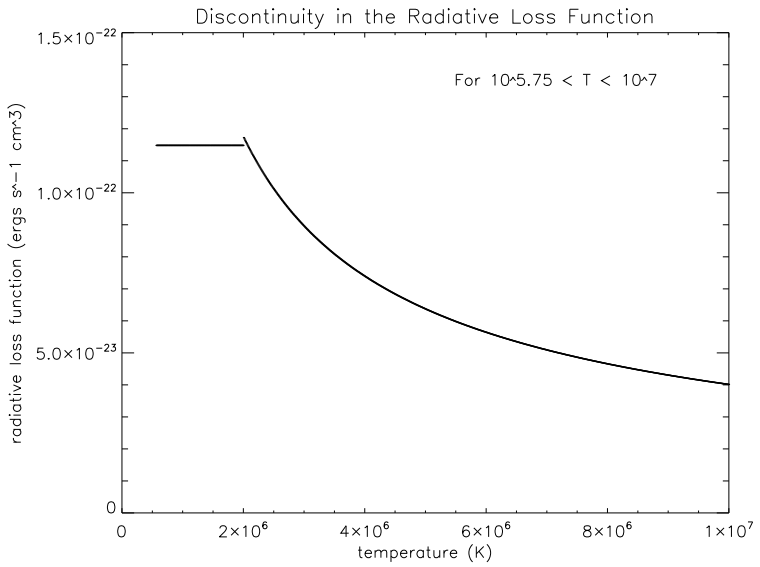

Figure 4.1: Plot of the radiative loss function approximations as described by Equations 4.6, showing the discontinuity between the two temperature regimes.

K, which is an acceptable approximation since we see very little increase beyond this level in any of our simulations.

Combining the energy deposited with the radiative losses, we can calculate the net change in energy of the plasma in volume V, which can be expressed as a change in temperature:

$$\Delta T = \frac{2\Delta E_{(}TOT)}{3nkV} \tag{4.7}$$

where ΔE is the net change in energy in one position bin of volume V. k is the Boltzmann constant, and n is the number density of the background plasma. This change is added to each position bin through which the particle passed in the time interval τ.

4.1.2 Conductive Cooling

Heat conduction results in the flow of heat along the temperature gradient, i.e. the transfer of heat from hotter to cooler regions, which results in a smoothing out of the temperature distribution. The conductive flux is essentially a transfer of energy along the direction of the magnetic field (flow perpendicular to the direction of the magnetic field is negligible, since thermal conduction is via electrons which are constrained to move along the magnetic field, and is thus discounted

here) and is described by[Rosner et al. (1978)]:

$$F_c(s,T) = -\kappa T^{5/2}\frac{dT}{ds} \qquad \text{ergs cm}^{-2}\ \text{s}^{-1} \tag{4.8}$$

where κ is the Spitzer conductivity ($\simeq 10^{-6}$ ergs s^{-1} cm^{-1} K$^{-\frac{7}{2}}$). The energy balance equation states that:

$$\frac{\partial \bar{u}}{\partial t} + \text{div}F_c = 0 \tag{4.9}$$

where $\bar{u} = \frac{3}{2}nkT$ (the energy density). Since we are treating this as essentially a 1D problem, divF_c becomes $\frac{\partial F_c}{\partial s}$ and thus the 1D flux conservation equation is:

$$\frac{\partial \bar{u}}{\partial t} = -\frac{\partial F(\bar{u})}{\partial s} \tag{4.10}$$

where $F(\bar{u}) = -D\frac{\partial \bar{u}}{\partial s}$ (D, the diffusion coefficient, is dependant on $\bar{u}$ (the temperature) in our model), and κ (the Spitzer conductivity) is the diffusivity. Thus, combining Equations 4.8 and 4.10 we can write:

$$\frac{\partial T}{\partial t} = \frac{\partial^2[D(T)\,T]}{\partial^2 s} \tag{4.11}$$

where $D(T) = \frac{\kappa T^{5/2}}{nk}$. Differencing this, we obtain a formula for the new temperature as a result of conductive cooling:

$$\begin{aligned} T_s^{t+1} = \quad & T_s^t + \frac{\Delta t}{(\Delta s)^2} \quad \times \\ & \left(\left[\frac{1}{2}D(T_{s+1}^t) + \frac{1}{2}D(T_s^t) \right] [T_{s+1}^t - T_s^t] - \left[\frac{1}{2}D(T_s^t) + \frac{1}{2}D(T_{s-1}^t) \right] [T_s^t - T_{s-1}^t] \right) \end{aligned} \tag{4.12}$$

where the index ^{t} indicates time and the index $_s$ indicates position.

This is an explicit finite differencing scheme, where the new temperature is calculated using only the temperatures at the current time, as opposed to an implicit scheme where temperatures at the new times are used in a backwards-time method. The explicit scheme is numerically much more straightforward than an implicit method, but less stable in certain situations. We were not able to implement an implicit scheme because of the difficulty of translating the method into code with a variable diffusion coefficient (one dependent on temperature, as ours is).

The stability criterion for the explicit method is:

$$\Delta t \leq \frac{(\Delta s)^2}{2D_{s+1/2}} \tag{4.13}$$

where $D_{s+1/2} = \frac{1}{2}[D(T^t_{s+1}) + D(T^t_s)]$. To maintain stability we must choose a suitably small Δt within the conduction routine - this can occasionally cause a problem by resulting in very long run-times for the simulations (see Section 4.1.4).

4.1.3 Saturated Heat Flux

Conductive cooling depends on the temperature gradient, with faster cooling occurring in areas of steeper temperature gradient. However, when the gradient and temperature reach a critical point, the the conditions for classical heat transfer break down and the plasma becomes "flux saturated". Under classical conditions, heat conduction occurs through electron-electron Coulomb collisions, where the mean free path for collisions is significantly less that the temperature scale height. However, at suitably high temperatures with large temperature gradients, the temperature scale height can become significantly smaller than the mean free path, at which point heat is no longer transferred diffusively via Coulomb collisions, but convectively by free streaming electrons. In this situation, the heat flux approaches a value which is determined by the electron thermal velocity.

The expression for saturated heat flux is[Brown et al. (1979)]:

$$\begin{aligned} F_S(s) &= \frac{3}{2} nkTv_s \\ &= \frac{1}{2} nm_e v_e^2 v_s \end{aligned} \tag{4.14}$$

where v_s is the maximum streaming velocity of the plasma, v_e is the electron velocity and other symbols are as before. According to numerical simulations by Manheimer & Klein (1975), $v_s = \frac{1}{6} v_e$. Inserting this and substituting $v_e = \sqrt{\frac{3kT}{m_e}}$, we have:

$$F_S(s) = \frac{1}{12} \frac{n(3kT)^{3/2}}{\sqrt{m_e}} \tag{4.15}$$

Saturated heat flux occurs when the mean free path for electron-electron collisions is larger than the temperature scale height, i.e.:

$$\lambda_{ee} > \frac{T}{\bigtriangledown T} \tag{4.16}$$

where T is the temperature at a specific postion, and $\bigtriangledown T = \frac{dT}{ds}$. The mean free path is given by[Spitzer (1962)]:

$$\lambda_{ee} \simeq 10^4 \frac{T^2}{n} \tag{4.17}$$

(in cgs units), therefore for saturated heat flux to apply we have the condition:

$$\frac{n\Delta s}{t\Delta T} \lesssim 10^4 \tag{4.18}$$

To apply saturated heat flux in place of classical heat conduction, we combine the equation for saturated heat flux with the flux conservation equation, giving:

$$\frac{\partial T}{\partial t} = -\frac{1}{12}\ \frac{n(3k)^{\frac{3}{2}}}{\sqrt{m}}\ \frac{\partial}{\partial s}(T^{\frac{3}{2}}) \tag{4.19}$$

Approximating the partial derivatives we get an expression for the change in temperature at a given position where saturated heat flux applies:

$$T_{t+1} \simeq \left(-\frac{1}{12}\ \frac{n(3k)^{\frac{3}{2}}}{\sqrt{m}}\ \frac{\Delta t}{\Delta s}\right) T_t^{\frac{3}{2}} + T_t \tag{4.20}$$

With our method of simulations and the models we are implementing, we find that the resultant temperature gradients are generally not large enough to result in saturated heat flux, with the exception of simulations with long timescales and increased electron flux.

4.1.4 Computational Restrictions & Limitations

General Limitations

Our simulations are limited by both the spatial resolution of the temperature arrays, and the temporal resolution of calculations of both heat deposition / radiative losses, and conductive losses calculations. The spatial resolution of the temperature distribution is determined by computer memory capacity, and results in a certain amount of artificial structure to the temperature distribution. Our programs record the loop temperature in bins of width 5×10^6 cm, the full loop length being divided into 800 segments for recording purposes. The energy deposited by a particle is calculated every 10 timesteps (0.0005 sec) to reduce the program runtime. If the particle travels less than one bin in the interval 0.0005 sec, the energy is assumed to be deposited over one whole bin. If the particle travels through several bins, the energy change per bin is calculated and the resulting temperature change is recorded into each of the bins through which it passed.

The conductive flux routine is applied to the current temperature distribution every 250 to 1000 timesteps (every 0.0125 to 0.5 sec) depending on the simulation, partly because it is a very time consuming process and would dramatically

slow the simulations were it to be calculated every timestep, and partly because this time interval allows a temperature distribution with less statistical noise to develop (noise produced by the artificial way we deposit temperature increases into a discreet number of bins in position).

Stability Problems With Finite Differencing

The stability criterion for the explicit finite differencing method in the conductive flux routine (Equation 4.13) places limits on the sizes of our timesteps (Δt) and position bins (Δs) within the cooling routine when very large temperature gradients are encountered. We maintain stability by choosing a suitably small Δt, while still ensuring the conduction routine runs for the correct length of time (the time between calculations of conduction - see above). The inclusion of saturated heat flux removes the need for a stability criterion when it applies, since it is the primary heat transfer mechanism for very large temperature gradients.

The explicit finite differencing method of applying conduction is also very sensitive to large gradients in temperature, and there are rare occasions where the gradient is sufficient to prevent the use of the classical conduction routine because of the small timestep required for stability, while at the same time not being large enough to result in saturated heat flux. To prevent this situation arising, we artificially reduce large and sudden spikes in temperature within the main simulation to twice the average surrounding loop temperature. These large spikes (several times larger than the average loop temperature at that position and time) are generally caused by large angle particle deflections, which in turn result in a large temperature increase over a small volume. These temperature spikes happen very infrequently (since large angle deflections are uncommon) but removing them will introduce a small artificial decrease in the overall temperature. This is not a significant problem, however, because in a real situation without stability limitations, conduction would remove these spikes very rapidly and their effect would be small. These spikes occur only a handful of times out of hundreds of thousands of iterations, and are therefore statistically insignificant in the final results.

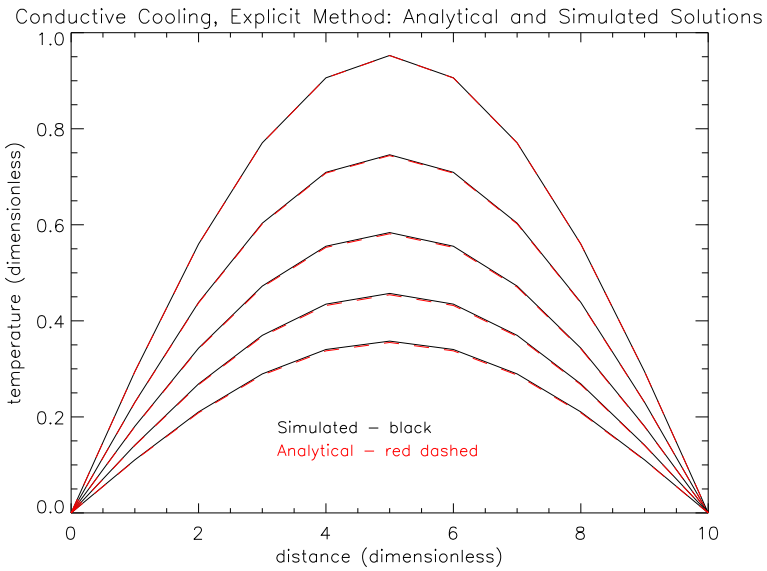

Figure 4.2: Plot of a comparison of the analytical (red) and simulated (black) solutions to the explicit conductive cooling routine, with a basic dimensionless sinusoidal initial distribution, run for 1 sec of cooling time.

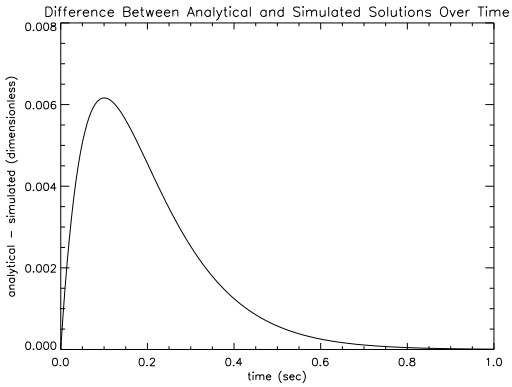

Figure 4.3: Plot of the maximum difference between the analytical and simulated solution as a function of time.

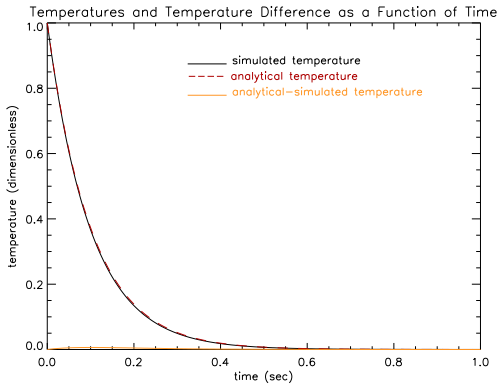

Figure 4.4: Plot of maximum analytical and simulated temperatures, and temperature difference (analytical-simulated).

4.2 Testing The Conductive Cooling Routine

4.2.1 Testing Against Theory

In Figure 4.2 we apply the conductive cooling routine with explicit finite differencing, as described in Section 4.1.2 above, to a basic sinusoidal distribution over a time of 1 sec. In this particular situation we use a constant diffusion coefficient, D, to allow comparison with the analytical solution (which does not include diffusion). The analytical solution is calculated (for a sinusoidal initial distribution)

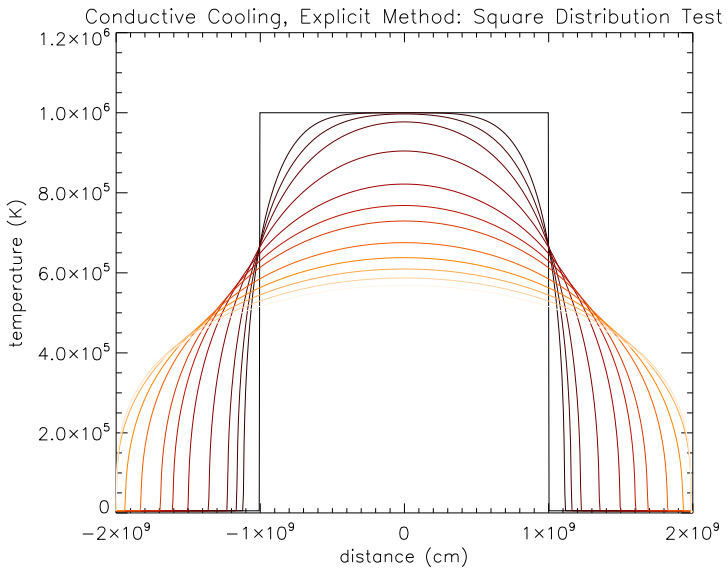

Figure 4.5: Test of the conductive cooling routine applied to a square initial temperature distribution over 700 sec. Lighter line colour indicates later times. Note that this test model is not designed to represent a loop (i.e. there are no field or density variations) and hence has no restriction on the flow of temperature at the edges.

using the following equation[Cheney & Kincaid (2004)]:

$$T = e^{-\pi^2 t} sin(\pi s) \tag{4.21}$$

where T is temperature, t is the time elapsed and s is position. We can see from Figure 4.2 that the simulated and analytical solutions are a close match, although the simulated results, using an explicit finite differencing routine, initially show a faster rate of cooling than predicated by the analytical solution, since it is not an exact solution, merely an approximation. However, if we plot the difference between the analytical and simulated solutions as a function of time (Figure 4.3) we can see that they converge after approximately 1 sec. Figure 4.4 shows that this convergence does not simply correspond to decreasing temperature, and in fact the point of maximum difference is located at a time of approximately 0.1 sec.

4.2.2 Sample Results

In Figure 4.5 we apply the cooling routine to a square temperature distribution over 700 sec, which demonstrates how effectively conduction smooths out steep temperature gradients (the edges of the square distribution). In Figure 4.6 we apply the routine to a basic gaussian temperature distribution, which cools as

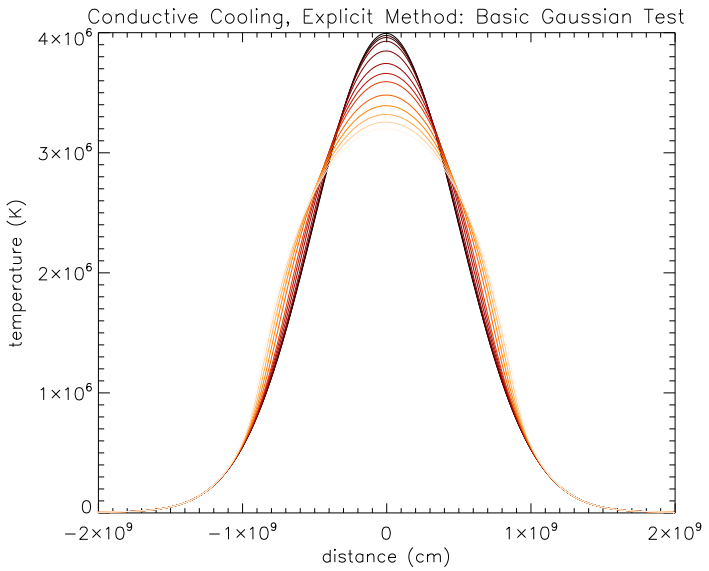

Figure 4.6: Test of the conductive cooling routine applied to a basic gaussian temperature distribution over 210 sec. Lighter colour indicates later time.

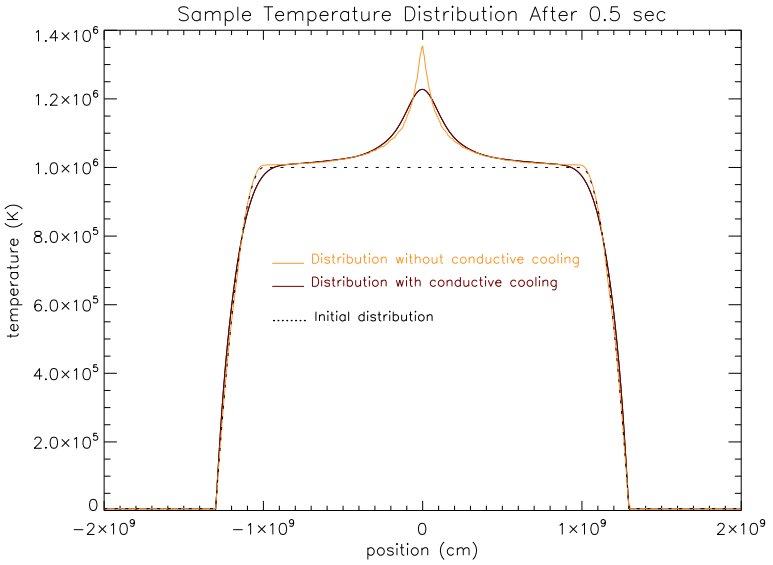

Figure 4.7: Plot of the temperature distribution from a simulation with an X-point field model after 0.5 seconds, showing the effect of conductive cooling on the distribution.

we would expect, since conduction has the largest effect on steep temperature gradients - the peak is smoothed out, the side temperature gradients are decreased and the areas of lowest temperature gradient (i.e. the edges) remain largely unchanged.

In Figure 4.7 we show a temperature distribution from one of our simulations

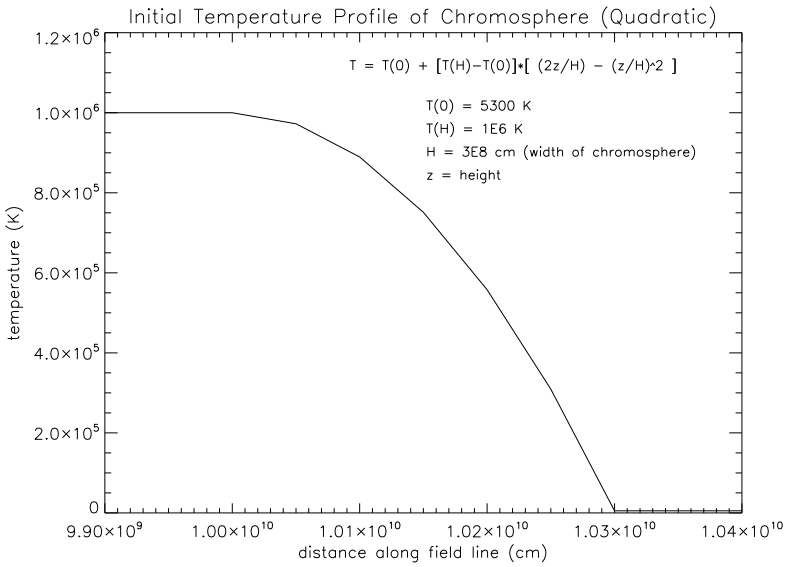

Figure 4.8: Initial quadratic temperature profile of the chromosphere. The profile at the opposite end is equivalent but mirrored.

using an X-point magnetic field model (Figure 2.13). The density is as described by Equation 2.17, with a coronal value of 10^9 cm^{-3}. We show the temperature distribution along the loop after 0.5 seconds. The yellow line shows the distribution with no conductive cooling applied, whereas the darker red line shows the distribution which results when conduction is applied every 0.05 seconds, as is the case in most of our simulations. The black dotted line indicates the initial temperature distribution of the loop. The effect of conduction is most noticeable in the chromosphere and at the looptop where temperature gradients are largest. The temperature gradients produced by our simulations are not high enough to result in saturated heat flux except in certain models with increased electron flux (Figures 4.19 and 4.30).

4.3 Basic Magnetic Loop Results

We initialise our loop models with a temperature distribution that is constant (10^6 K) throughout the loop length in the corona, decreasing quadratically across the chromosphere at either end, and constant (5300 K) outside this (to represent the photosphere). In the event that cooling causes the loop temperature to drop below background levels, we force the temperature to remain at the background photospheric level at that point indefinitely, or until it undergoes further heating, since in a real loop the temperature would not drop below the background level

but reach equilibrium. In reality, it is unlikely that chromospheric and coronal sections of a loop would drop to such low temperatures, since other heating mechanisms are present besides Coulomb collisions (e.g. plasma shockwaves). The full initial temperature distribution can be seen in Figure 4.7 (the black dotted line) and the quadratic profile of the chromosphere can be seen in Figure 4.8. The quadratic temperature profile we use for the chromosphere is of the form in Goodman (1998) and is described by:

$$T(z) = T(0) + [T(H) - T(0)] \left[2 \left(\frac{z}{H} \right) - \left(\frac{z}{H} \right)^2 \right] \tag{4.22}$$

where z is height (within the chromosphere), H is the maximum height (the top) of the chromosphere, $T(H)$ is the temperature at the top (the coronal temperature), $T(0)$ is the temperature at the base (the photospheric temperature) and $T(z)$ is the temperature at a given height within the chromosphere. In our 1D loop model, z is equivalent to s, the distance along the loop.

The maximum temperatures we see in the following results are lower than observations for reasons discussed in Section 4.1.4.

Constant Coronal Magnetic Field

In Figure 4.9 we see the temperature distribution along a loop where the magnetic field converges only across the chromosphere at each end. The test particles are injected all at $t = 0$ sec with a power law velocity distribution between 1×10^{10} cms^{-1} and 2×10^{10} cms^{-1} (approximately 28.4 keV to 113.7 keV) and with a uniform distribution of pitch angles between 0° and 90° to the field line, in both directions. At early times we see a central peak in temperature, but as time progresses the energy is distributed along the loop by conduction, and the temperature continues to increase as trapped particles deposit energy. Conduction effectively prevents peaks in temperature in the higher density chromospheric regions because of the large temperature gradients there. In the five seconds which the simulation covers, approximately 45% of the test particles escaped the magnetic bottle and were stopped primarily in the chromosphere due to the increased density - the majority remain trapped in the loop.

Variable Magnetic Field

In Figure 4.10 we use a symmetric magnetic field which varies across the entire length of the loop (as opposed to only across the chromosphere as previously),

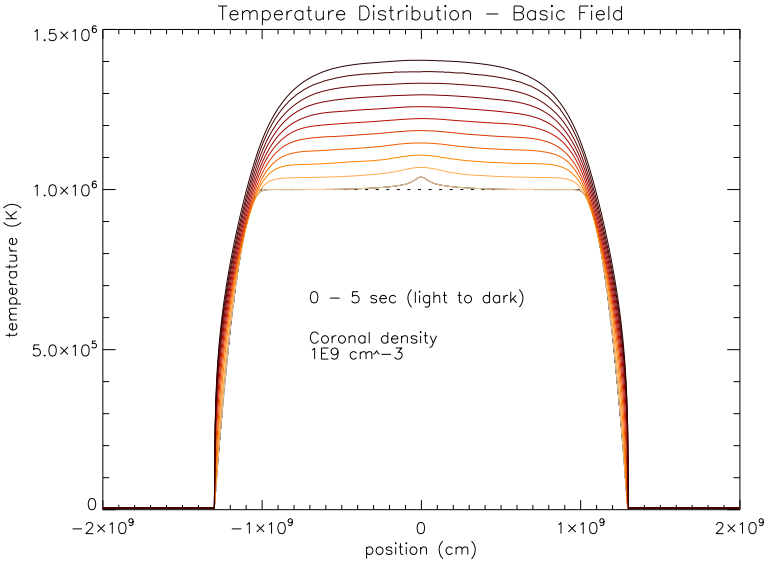

Figure 4.9: Temperature evolution over 5 sec for a loop of length 1.3×10^9 cm from apex to footpoint, with a magnetic field as shown in Figure 2.10. Includes heat loss through radiation, conduction and saturated heat flux. Density is as described by Equation 2.17 with a coronal density of 10^9 cm^{-3}. All test particles injected at $t = 0$ sec, with a power law distribution between 1×10^{10} and 2×10^{10} cms^{-1}, and uniform pitch angle distribution between 0° and 90° to the field line in both directions.

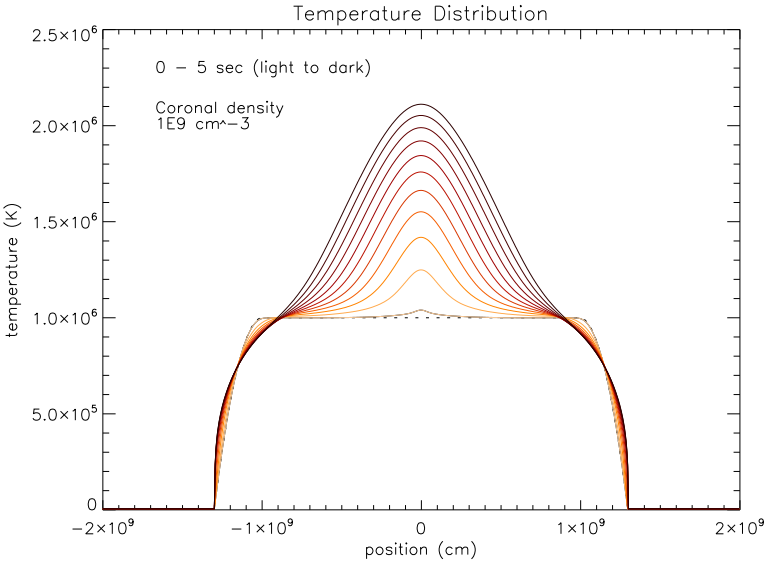

Figure 4.10: As Figure 4.9 but with a magnetic field which varies along the loop length from 100 G at the apex to 1000 G at the footpoints, as shown in Figure 2.11.

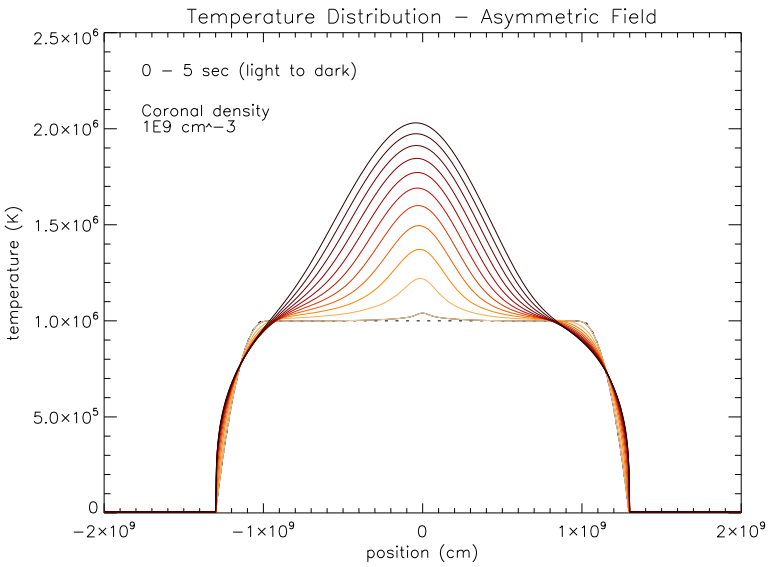

Figure 4.11: As Figure 4.9 but with an asymmetric magnetic field which varies along the loop length, as shown in Figure 2.12. Field strength is 500 G at the left footpoint, 1000 G at the right footpoint and 100 G at the apex).

with all other parameters as before. In this situation, there is a more pronounced magnetic bottle, and fewer particles are able to reach the chromosphere. Conductive cooling smooths out any temperature increases we would otherwise see at the footpoints, due to the large temperature gradient across the chromosphere. In this model approximately 13% of particles were lost over the 5 sec in total as a results of scattering pushing particles into the loss cone and hence allowing them to escape the magnetic bottle.

In both this model and that shown in Figure 4.9, the heat loss rate through radiation and conduction (primarily the latter) is large enough to prevent any significant increase in temperature. A higher temperature may arise from increasing the density of the loop (but consequently causing particles to quickly be scattered out of the loss cone or run out of energy), increasing the energies of the particles (which would then be relativistic), or by continuous injection of particles (rather than all at $t = 0$ sec) with longer simulations, allowing the temperature to build up over a longer period of time.

In Figure 4.11 we use an asymmetric magnetic field which varies throughout the loop length. The coronal density at the loop apex is 100 G, the left footpoint is 500 G and the right footpoint is 1000 G. This results in an asymmetric magnetic bottle, with electrons able to propagate further towards the footpoint on the left hand side where the field is weaker. We can see the effect of this in the peak being

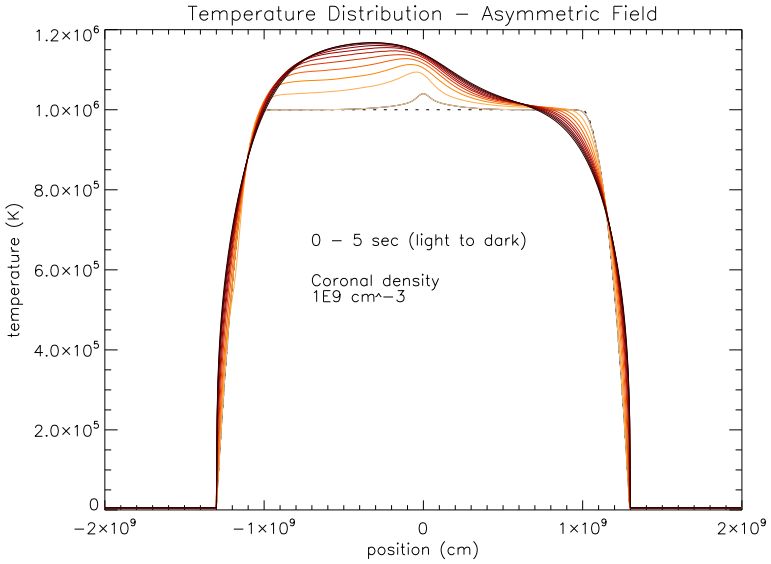

Figure 4.12: As Figure 4.11 but with a more pronounced asymmetric field, with a strength of 100 G at the apex, 100 G at the left footpoint (i.e. no convergence) and 1000 G at the right footpoint.

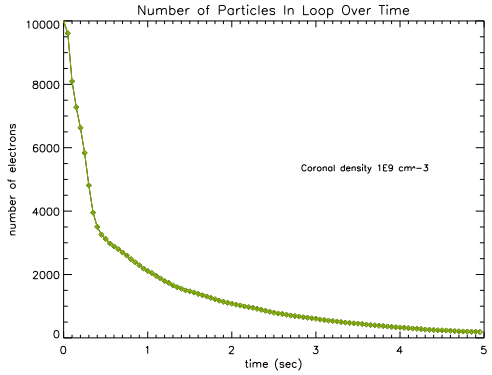

Figure 4.13: Plot of the number of particles left in the simulation which produced Figure 4.12 as a function of time. (See Section 3.2.1 and Figure 3.20 for explanation of the pattern seen here.)

offset to the left slightly. In Figure 4.12 we have a more pronounced asymmetric loop - in this case, the left hand footpoint is at 100 G, the same as the corona, meaning there is no field convergence at all at that end. The right footpoint is at 1000 G as before. In this situation, those particles that are injected in the positive direction are mirrored near the right hand chromosphere whereupon they move back along the loop and escape at the left hand side, where no mirroring occurs. Particles injected in the negative direction pass straight out of the loop into the photosphere where they are immediately stopped by the high density there. As

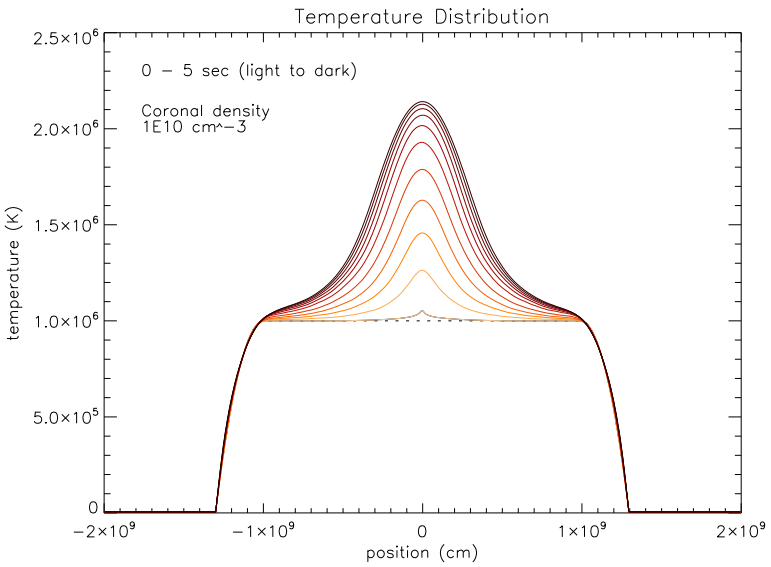

Figure 4.14: As Figure 4.10 but with an increased coronal density of 10^{10} cm^{-3}.

a result, in this model we see higher energy deposition along the left leg of the loop. However, although the density increases markedly across the chromosphere and the majority of particles deposit most of their energy there, we still find that conduction is able to remove any peaks in temperature we would otherwise expect to see there. In this model, 98% of particles are stopped within 5 sec - in Figure 4.13 we can see the number of particles left in the simulation over time.

Increased Coronal Density

In Figure 4.14 we return to a symmetric loop, as in Figure 4.10, but with an increased coronal density of 10^{10} cm^{-3}. This results in slightly higher temperatures, however the higher particle loss rate (after 5 seconds, approximately 82% of particles have been lost) means that the rate of temperature increase slows, and would eventually stop if we were to run the simulation for a longer time period. Conduction and radiation would then gradually cool the loop in the absence of any mechanism to increase the temperature.

Continuous Particle Injection

To compensate for the loss of particles over time, we can inject particles continuously rather than all at $t = 0$ sec - we show results from simulations with continuous particle injection in Figures 4.15 and 4.16. In Figure 4.15 particles are

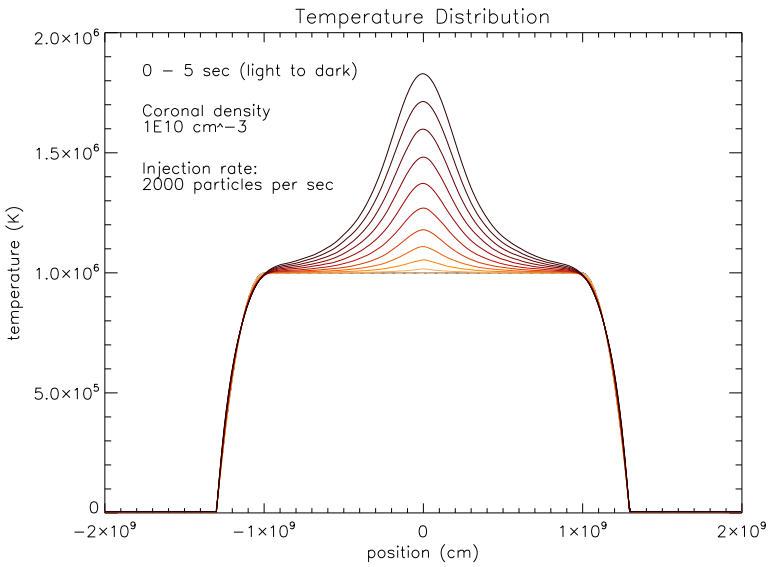

Figure 4.15: As Figure 4.14 but with continuous particle injection. Particles were injected at a rate of 2000 particles per second.

injected over the full 5 seconds with an injection rate of 2000 particles per second and all other parameters as in Figure 4.14. This results in fewer particles in the simulation at early times, but at later times the number of particles remains high, since more are continuously being injected to replace those lost. Figure 4.17 shows the number of particles in the simulation over time. Although we do not see higher overall temperature here with continuous injection, the temperature would eventually become higher than in the instantaneous injection model if we simulated a longer period of time - as we can see, the temperature continues to increase steadily over time for the 5 sec length of this simulation as new particles replace those that are lost, although we would expect a steady-state situation to be reached eventually between energy deposition and energy losses.

In Figure 4.16 we see the same continuous injection model but with an even higher coronal density of 10^{11} cm^{-3}. Figure 4.18 shows the corresponding plot of the number of particles in the loop over time. The overall temperature is lower than in the lower density model. There are several explanations for this: one is that even with continuous injection the majority of particles are lost very quickly as a result of the high coronal density (we can see the relatively low level of particles in the loop at a given time in Figure 4.18) so there are fewer particles in the loop at any one time. Another aspect is that an increased density means that energy deposited is spread out through a larger number of background parti-

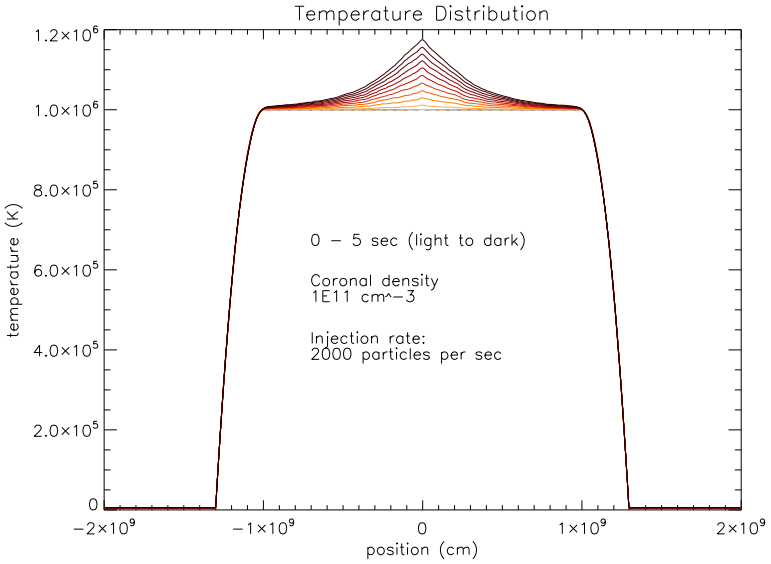

Figure 4.16: As Figure 4.15 but with an increased coronal density of 10^{11} cm^{-3}.

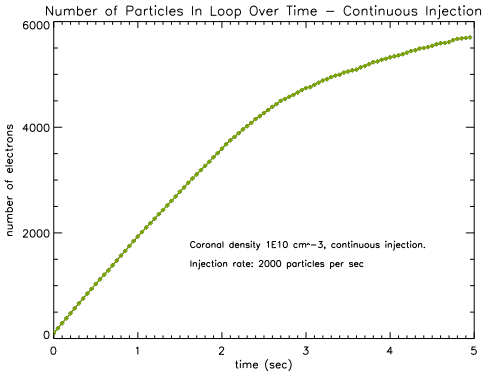

Figure 4.17: Plot of the number of particles in the simulation which produced Figure 4.15 as a function of time.

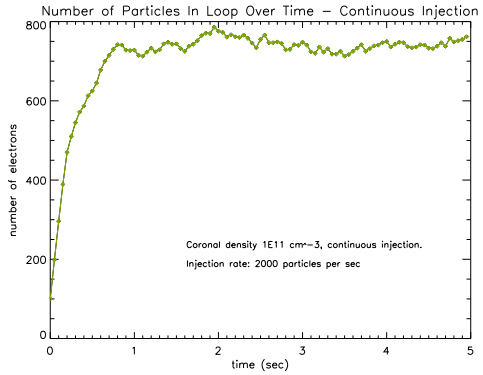

Figure 4.18: Plot of the number of particles in the simulation which produced Figure 4.16 as a function of time.

cles,resulting in a lower thermal energy per particle. In addition, radiative losses, which are proportional to the density squared, are much higher in comparison to the energy deposited.

Figure 4.18 also shows that at this higher density, the number of particles in the simulation reaches a steady-state situation after approximately 1.5 sec, something we did not see occur within the 5 second run with a coronal density of 10^{10} cm^{-3}. Again, if this simulation was run for a much longer time, we would expect the temperature change to reach a steady-state, but for the length of time shown, conduction is not sufficient to completely overwhelm the rate of temperature increase in this model.

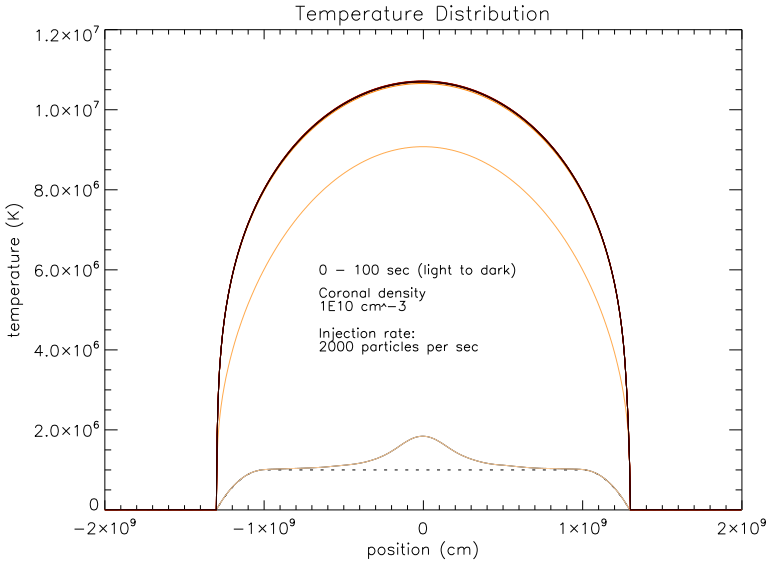

Figure 4.19: As Figure 4.15 but simulating a longer time period of 100 sec and with an increased flux of 10^{37} electrons s^{-1}.

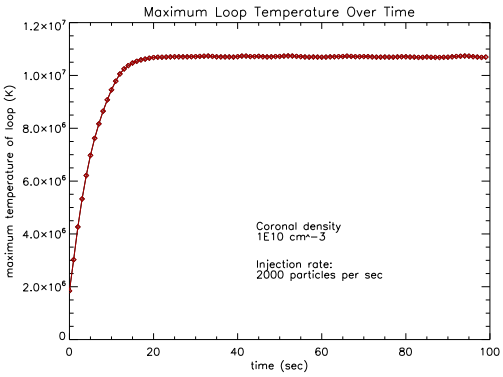

Figure 4.20: Maximum temperature in the simulation (i.e. the looptop temperature) as a function of time for the loop shown in Figure 4.19.

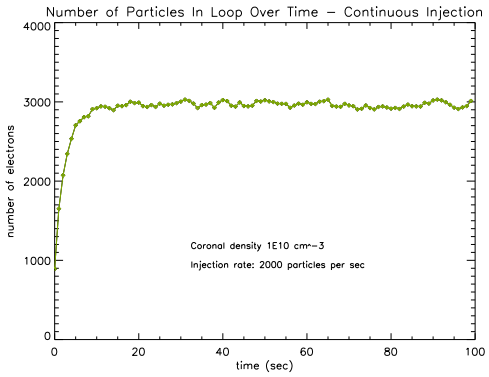

Figure 4.21: Plot of the number of particles in the simulation which produced Figure 4.19) as a function of time.

Longer Time Interval Results

The temperatures observed in all the previous models do not rise much higher than 2×10^6 K. However, if we increase the length of time which we are simulating and the assumed flux of electrons which we use to scale up to represent a realistic loop (see Section 4.1.1) we achieve much higher temperatures, over 10^7 K (a reasonable minimum temperature for thermal X-ray emission; Chapter 5). In Figure 4.19 we show the temperature evolution over 100 sec from a continuous injection model with coronal density 1×10^{10} cm^{-3} and an increased assumed electron flux of 10^{37} electrons s^{-1} (as opposed to 10^{36} as before). In this situation,

unlike previously, saturated heat flux does occur, but approximately 60 times less frequently than conductive heat flux, and does not produce any visible effects in the final temperature distribution. This is only one of two simulations where we see saturated heat flux (see also Figure 4.30). Figure 4.20 shows the evolution of the maximum temperature of the loop (located at the apex) as a function of time. After approximately 15 sec the number of particles present in the simulation (Figure 4.21) and hence the temperature reaches a steady-state, where the rate of increase is matched by the losses (radiative, conductive heat flux and saturated heat flux).

4.4 X-Point Magnetic Loop Results

In Figure 4.22 we see the temperature distribution along a loop with a symmetric X-point magnetic field configuration (see Section 2.2.2). This has a density profile as described by Equation 2.17 with a coronal density of 10^9 cm^{-3} and an initial temperature profile as described at the beginning of Section 4.3. Particles are all injected at $t = 0$ sec, with a power law distribution between 1×10^{10} and 2×10^{10} cms^{-1}, and uniform pitch angle distribution between 0° and 90° to the field line in both directions.

The temperature profile we see here is comparable to that seen in the equivalent basic loop model as seen in Figure 4.10, since the parameters are similar in both models, the only difference being the form of the magnetic field (to compare the fields, see Figures 2.11 and 2.14).

Increased Coronal Density

In Figure 4.23 we have the same situation as in Figure 4.22 but with an increased coronal density of 10^{10} cm^{-3}. This higher density results in higher temperatures, but it also means that particles are scattered out of the magnetic bottle and stopped more quickly. Over this 5 second run, approximately 88% of particles were lost, compared to only approximately 27% in the model with a coronal density of 10^9 cm^{-3}. In this situation, we see the rate of temperature increase slow as particles are lost. We also note that the chromospheric regions do not cool below the initial temperature level as they do in the lower density model, because the higher density here allows for a temperature increase large enough to counteract conduction to an extent, although not enough to allow peaks of temperature to develop at the footpoints.

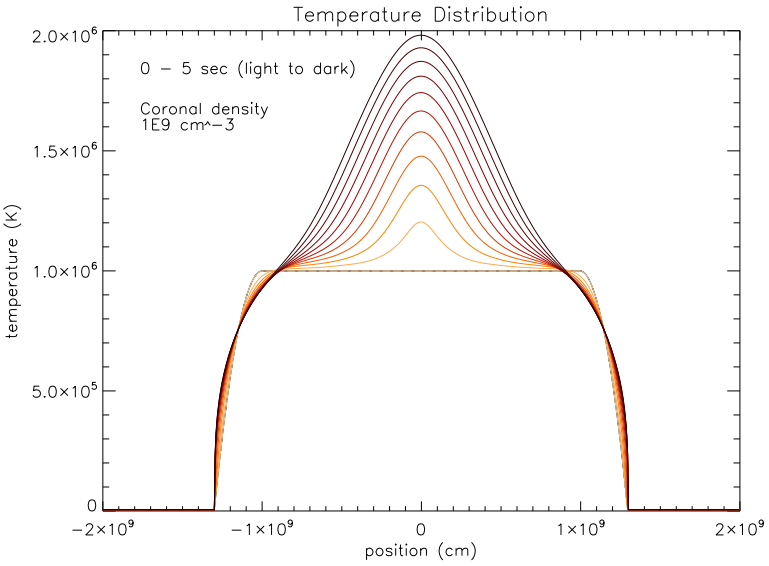

Figure 4.22: Temperature evolution over 5 sec for a loop with a symmetric X-point magnetic field configuration (as shown in Figure 2.14) and length 1.3×10^9 cm from apex to footpoint. Includes heat loss through radiation, conduction and saturated heat flux. Density is of the form described in Equation 2.17 with coronal density 10^9 cm^{-3}. All test particles injected at $t = 0$ sec, with a power law distribution between 1×10^{10} and 2×10^{10} cms^{-1}, and uniform pitch angle distribution between 0 and 90° to the field line in both directions.

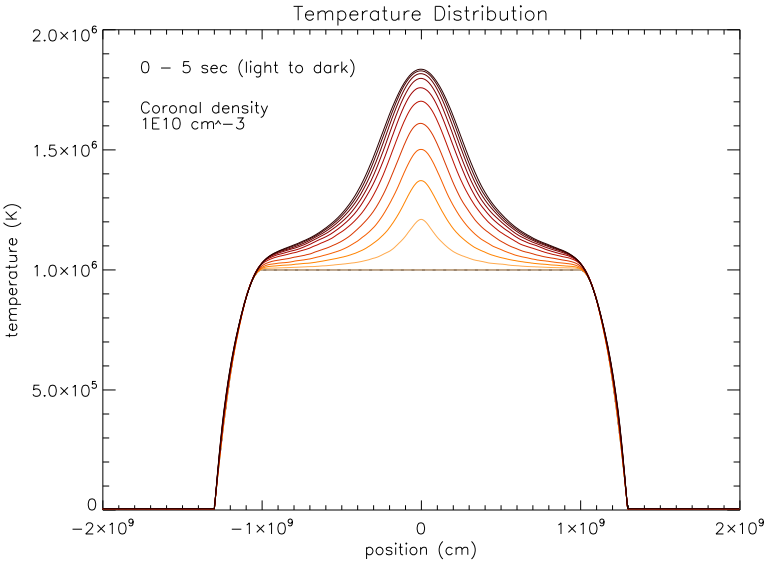

Figure 4.23: As Figure 4.22 but with an increased coronal density of 10^{10} cm^{-3}.

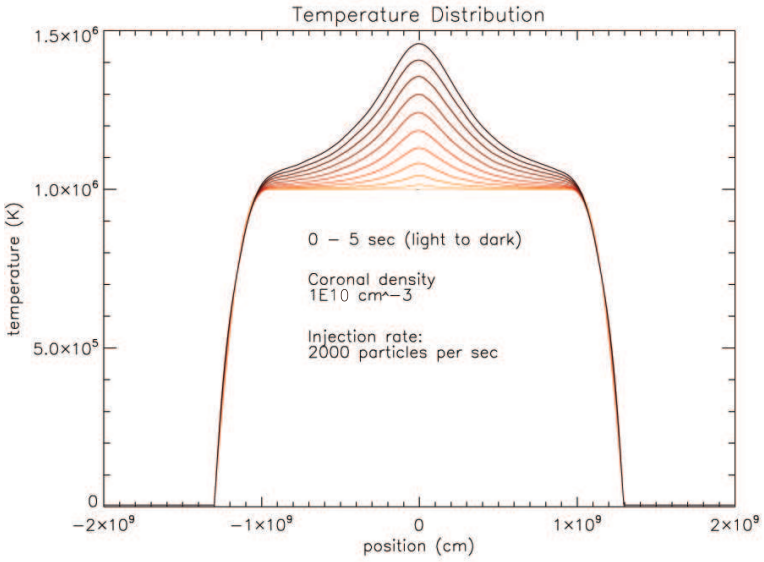

Figure 4.24: As Figure 4.23 but with continuous particle injection. Particles are injected at a rate of 2000 particles per second.

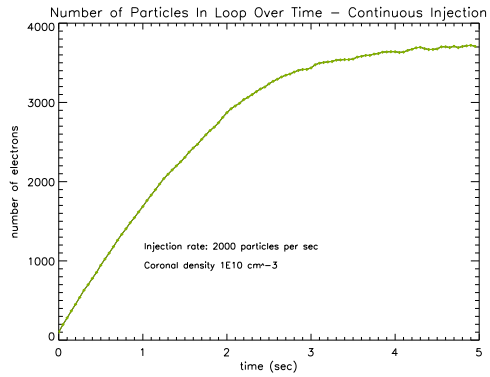

Figure 4.25: Plot of the number of particles in the simulation which produced Figure 4.24 as a function of time.

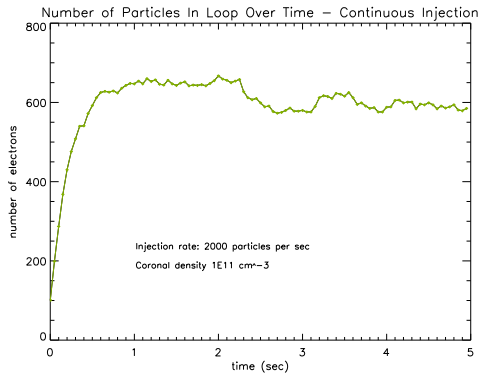

Figure 4.26: Plot of the number of particles as a function of time in a simulation equivalent to that shown in Figure 4.24 but with an increased coronal density 10^{11} cm^{-3}.

Continuous Particle Injection

Figure 4.24 has the same parameters as Figure 4.23 but with continuous particle injection, with an injection rate of 2000 particles per second. We see a slower increase in temperature initially because there are fewer particles in the simulation at any given time than when all are injected at $t = 0$ and the overall temperature is also lower because of this. The particle loss rate in the X-point model is higher than in the basic field models - compare Figure 4.17 (basic field) and Figure 4.25 (X-point field). The latter has a much lower peak number of particles at any given time.

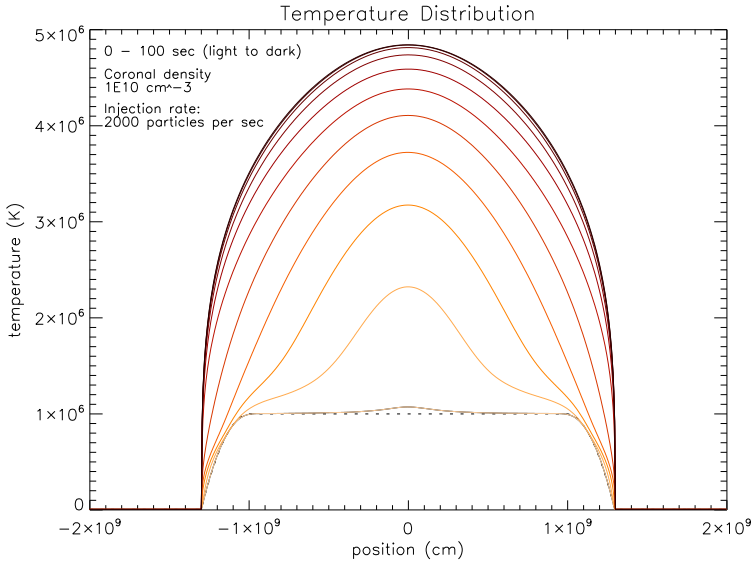

Figure 4.27: As Figure 4.24 but showing the temperature evolution over a longer time interval of 100 sec.

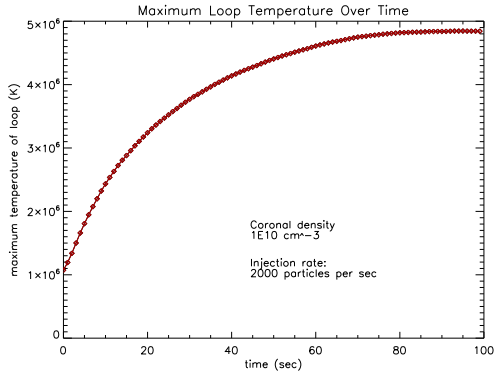

Figure 4.28: Maximum temperature in the loop (i.e. the looptop temperature) as a function of time for the loop shown in Figure 4.27.

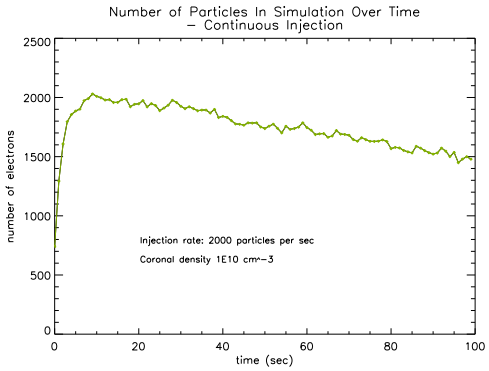

Figure 4.29: Plot of the number of particles in the simulation which produced Figure 4.27 as a function of time.

If we increase the density further (to 10^{11} cm^{-3} in the corona) the rate of particle loss in this X-point field geometry is slightly larger than the injection rate (see Figure 4.26). With higher density, energy deposited must be distributed between more background particles and radiative losses are also much higher, and this, combined with a lower number of particles in the loop at a given time, will eventually allow cooling to exceed the heating rate in this model.

Longer Time Interval Results

If we use a continuous injection model to simulate a longer time interval, we see higher loop temperatures as expected, since energy continues to be deposited as long as particles are present in the loop. In Figure 4.27 we show the temperature evolution over 100 sec for a loop with all parameters as previously (i.e. Figure 4.24), except the length of time simulated. We can see that the temperature does reach a higher level, but it does not increase above 10^7 K, a reasonable minimum temperature for thermal X-ray emission (see Chapter 5). In Figure 4.28, we plot the maximum temperature in the loop (which is located at the apex) as a function of time - the rate of temperature increase slows as the number of particles present in the simulation decreases (particle loss rates are higher than injection rates in this model, Figure 4.29) and conduction gradually cools the loop.

We increase the flux of particles in the loop to 10^{37} electrons s^{-1} (from 10^{36} previously) than in previous simulations. We show results with this increased flux in Figure 4.30. Here, we see a higher maximum temperature, but it is not high enough to produce thermal X-ray emission (see Chapter 5). Figure 4.31 shows the maximum temperature (the loop apex temperature) as a function of time. With this higher flux, we see that the temperature increases more quickly initially, but after reaching a looptop peak at approximately 20 sec it begins to decrease slowly as conductive cooling dominates over temperature deposition, in contrast to the basic field model equivalent where a steady-state is reached (Figure 4.19). This is because the particle loss rate in the X-point field configuration is larger than in the basic field model (compare Figures 4.32 and 4.21) and hence the temperature decreases as the number of particles drops and conduction and radiation cool the loop.

In this model saturated heat flux also has an effect, although it is small in comparison to conductive heat flux - the condition for conductive heat flux occurs approximately 160 times more frequently than that for saturated heat flux. This is one of only two simulations we have run where saturated heat flux occurs, the other being a similar simulation using our more basic field model (see Figure 4.19).

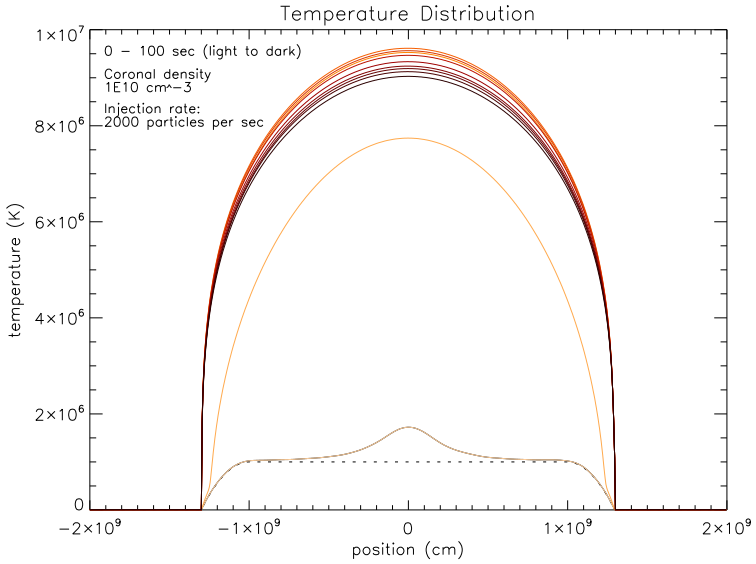

Figure 4.30: As Figure 4.27 but with an increased flux of 10^{37} electrons s^{-1}.

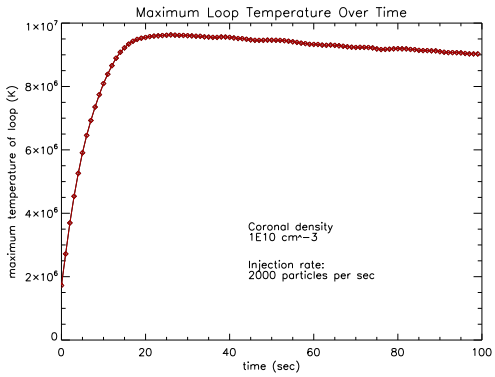

Figure 4.31: Maximum temperature in the simulation (i.e. the looptop temperature) as a function of time for the loop shown in Figure 4.30.

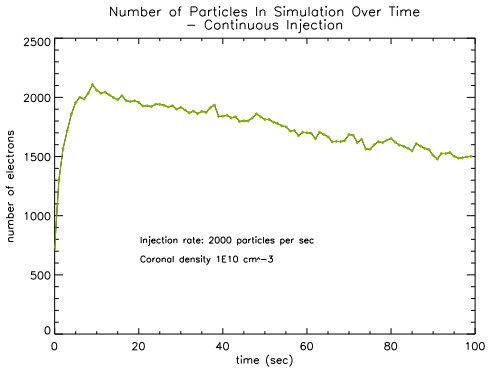

Figure 4.32: Plot of the number of particles in the simulation which produced Figure 4.30 as a function of time.

4.5 Conclusion

In conclusion, it would appear that to achieve temperatures approaching and exceeding 10^7 K using our models, several conditions must be met: the electron flux must be high; the coronal density must not be too large (approximately 10^{10} cm^{-3}); there must be continuous particle injection; and the length of time simulated must be large, of the order 20 sec or more. However, even when all these conditions are met, the maximum temperatures produced do not exceed $\sim 1.1 \times 10^7$ K. It is apparent that there must be more phenomena contributing to loop temperature increase than Coulomb collisions between background particles

and fast moving beam particles alone. For future work, it would be beneficial to combine these test particle simulations with hydrodynamic simulations in order to incorporate effects such as plasma shocks (which would increase temperature) and chromospheric evaporation (which would decrease temperature), which both contribute to changes in loop temperature. In particular, hydrodynamic simulations would allow us to model bulk plasma flows which occur over tens of seconds, timescales which we have considered with our test particle simulations. These bulk flows would change the temperature distributions we see in Figures 4.19, 4.27 and 4.30.

Chapter 5

Thermal & Non-Thermal X-Ray Spectra

In Chapter 3, we looked at hard X-ray emission ($\sim$ 20 - 100 keV) which is produced via non-thermal bremsstrahlung emission from fast (non-relativistic) electrons moving along the magnetic field lines. Soft X-ray emission has also been observed ($\sim$ 1 - 20 keV) and has a more thermal spectrum consistant with emission from a hot plasma. In this chapter, we look at the thermal bremsstrahlung X-ray emission produced by the beam-heated plasma (see Chapter 4), and attempt to combine this with hard X-ray emission (see Chapter 3) from the same beam to produce X-ray spectra similar to those seen with the RHESSI satellite.

5.1 Theory

5.1.1 Thermal X-Ray Emission

Thermal bremsstrahlung X-ray emission is produced as thermal electrons in a hot gas lose energy, primarily through Coulomb collisions with other electrons. Since the interaction is primarily a mutual exchange of energy between electrons of similar energies, these electrons do not lose energy through collisions as fast as the non-thermal electrons do in collisions with the much colder ambient plasma, therefore thermal emission is more efficient than non-thermal in terms of bremsstrahlung yield per electron. Soft X-rays are generally accepted as being in the energy range 1 - 20 keV, emitted from hot plasmas with Maxwellian temperatures from approximately 1×10^7 K to 3×10^7 K.

Electrons in a hot plasma have a Maxwellian velocity distribution described

by(Tandberg-Hanssen & Emslie (1988)):

$$f(v) = 4\pi \left(\frac{m}{2\pi nkT}\right)^{3/2} nv^2 e^{(-\frac{mv^2}{2kT})} \tag{5.1}$$

where m is the mass of an electron, n is the number density of the hot plasma, T is the temperature of the plasma, and v is the velocity of an electron in the plasma. This corresponds to an energy distribution of:

$$\begin{aligned} f(E) &= f(v)\frac{dv}{dE} \\ &= \frac{2n_e}{\sqrt{\pi}(kT)^{\frac{3}{2}}} \sqrt{E}\ e^{(-\frac{E}{kT})} \end{aligned} \tag{5.2}$$

(in electrons per cubic centimetre per erg) where E is the energy of an electron corresponding to v. The bremsstrahlung emission from a volume V resulting from the electrons' interactions with ambient protons (also of number density n) is given by[Tandberg-Hanssen & Emslie (1988)]:

$$I(\epsilon) = nV \int_{\epsilon}^{\infty} f(E)v(E)\sigma_B(\epsilon, E)\ dE \tag{5.3}$$

where $\sigma_B(\epsilon, E)$ is the electron-proton cross-section - we use the Bethe-Heilter cross-section (Equation 3.2). Other cross sections could be used in further work, but due to time limitations we restrict ourselves to this one only, as used in Brown (1971). In order to calculate the intensity as seen by a detector at Earth, we must also divide by $4\pi R^2$ where R is 1AU. Inserting these and approximating the integral with a sum gives:

$$I(\epsilon) = \frac{4}{3}\sqrt{2m}\ \frac{n^2c^2}{(k\pi)^{3/2}}\ \left(\frac{r_0}{R}\right)^2\ \frac{1}{137}\ \frac{V}{T^{3/2}}\ \frac{1}{\epsilon}\sum_{E=\epsilon}^{\infty} e^{(-\frac{E}{kT})} ln\left[\frac{1+\sqrt{1-\frac{\epsilon}{E}}}{1-\sqrt{1-\frac{\epsilon}{E}}}\right]\Delta E \tag{5.4}$$

(photons per second per square centimetre of detector at Earth per unit ϵ) where r_0 is the classical electron radius.

5.1.2 X-Ray Spectra

We create X-ray spectra by summing over time the intensity observed for each photon energy, resulting in a plot of intensity against photon energy. In observed spectrum there are two distinct emission regimes - the power law non-thermal emission and the steeper thermal emission curve. In Figure 5.1 we see the spectra observed by RHESSI from the August 20th 2002 flare, a flare with a weak

Figure 5.1: RHESSI X-ray photon spectrum from the August 20th 2002 flare. The solid line indicates the albedo corrected photon spectrum and the crosses indicate the observed photon spectrum. The horizontal widths of the crosses represent energy bands and the vertical widths represent show $\pm 1\sigma$ statistical plus systematic uncertainties. The dotted and dashed line shows the best fit to the non-thermal component (a thin-target fit) and the dotted line shows the best fit to the thermal component (an isothermal fit). This event shows a relatively low energy thermal component. [Kašparová et al. (2005), Figure 2]

thermal component, over a period of 2 seconds. In it, we can see the steep thermal emission curve from approximately 8-20 keV, and then the shallower power law non-thermal emission from approximately 20 - 100 keV. A similar spectrum observed from the July 23rd 2002 flare, a flare with a stronger thermal component, can be seen in the top panel of Figure 1.7.

5.2 Results

Given that soft bremsstrahlung X-rays in the range $\sim$ 1 - 20 keV originate from plasmas of temperatures of the order 1×10^7 to 3×10^7 K, almost all loop configurations we show in Chapter 4 will not give rise to significant thermal emission in the RHESSI energy range, since with the parameters we have used, and given our model, most simulations do not produce peak temperature much over 2×10^6 K. However, when we run simulations with continuous particle injection for 100 sec, we do see temperature increases approaching and exceeding 1×10^7 K. However, only the simulation with a basic field model and increased electron flux produces

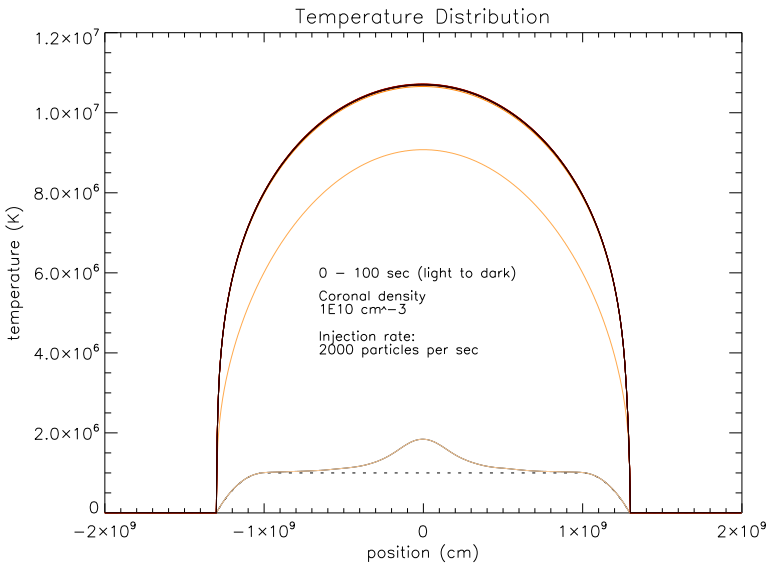

Figure 5.2: Temperature evolution over 100 sec in a loop with a flux of 10^{37} electrons s^{-1}. The density profile is described by Equation 2.17 with a coronal density of 10^{10} cm^{-3} and the magnetic field as shown in Figure 2.11. All particles were injected at $t = 0$ sec in a power law distribution between 1×10^{10} cms^{-1} and 2×10^{10} cms^{-1}, with initial pitch angles from 0 to 90° to the field line in both directions.

temperatures high enough, therefore this is the one we shall consider here.

This model uses a symmetric magnetic field as shown in Figure 2.11, which varies throughout the loop length, with a minimum (coronal) value at the loop apex of 100 G and maximum (photospheric) values at the footpoints of 1000 G. The density of the loop is described by Equation 2.17, varying across the chromosphere from 10^{10} cm^{-3} in the corona to 10^{16} cm^{-3} in the photosphere. The change in volume (as a result of changing loop area) along the loop is incorporated into the scaling factor (see Section 3.1.1). When scaling up values in our simulations to produce dimensional results and represent realistic loop parameters, we assume a flux of 10^{37} electrons s^{-1} (as opposed to the lower value of 10^{36} used in the majority of our simulations) (see Sections 3.1.1 and 4.1.1). This higher flux results in temperatures large enough to produce thermal X-ray emission at a low level. Particles are injected continuously at a rate of 2000 particles per second, with initial pitch angles chosen randomly from a uniform distribution between 0° and 90° to the field line in both directions, and with a power-law initial energy distribution between 1×10^{10} cms^{-1} and 2×10^{10} cms^{-1}.

In Figure 5.2 we show the evolution of the temperature distribution from this model over 100 sec. In Figures 5.3 and 5.4 we show the non-thermal and

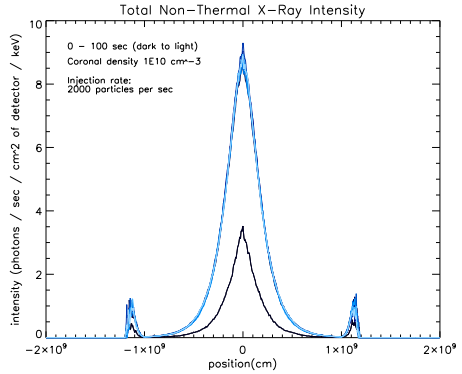

Figure 5.3: Non-thermal X-ray emission (summed over photon energy) over 100 sec from a loop with a symmetric magnetic field varying from 100 G (coronal) to 1000 G (photospheric), a coronal density of 10^{10} cm^{-3} and an increased electron flux of 10^{37} electrons s^{-1} cm^{-2}.

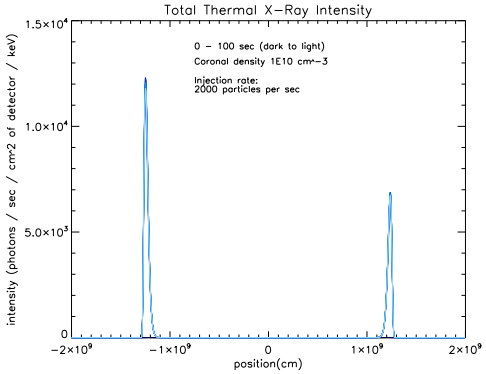

Figure 5.4: Thermal X-ray emission (summed over photon energy) over 100 sec corresponding to the temperature distributions shown in Figure 5.2.

thermal X-ray emission from this model over the same time interval. The overall thermal emission is located primarily at the footpoints where the density is higher, despite the lower temperatures there. However, if we plot the thermal emission as a function of photon energy rather than time (Figure 5.5), we see that footpoint emission only dominates at low photon energies. From 17 keV and above, the thermal emission from the looptop dominates over the footpoints. However the overall thermal emission drops very quickly with increasing photon energy, so the intensities we see at these relatively higher photon energies is very small in comparison with the footpoint emission seen at lower photon energies.

In Figure 5.6 we show the evolution of the total thermal emission over all photon energies at the footpoints and looptop as a function of time. The looptop emission is very small compared to the footpoint emission (of the order 3300 times smaller) and therefore is not visible in this plot, and we can also see that the thermal emission is negligible for about the first 8 seconds, while the temperature is still too low to produce it, and then increases sharply to a steady-state as the temperature increases correspondingly (see Figure 4.20).

The reason for the asymmetry in thermal emission between the footpoints is that it is strongly dependent on density, loop cross-sectional area and temperature - this difference in thermal emission is produced by a small difference in temperature (at an equivalent point in the chromosphere, the percentage difference in temperature between the left and right chromosphere is only 1.2%) across each chromospheric region, which is amplified in the calculation of intensity using Equation 5.4 as the density increases and loop area decreases across the chromo-

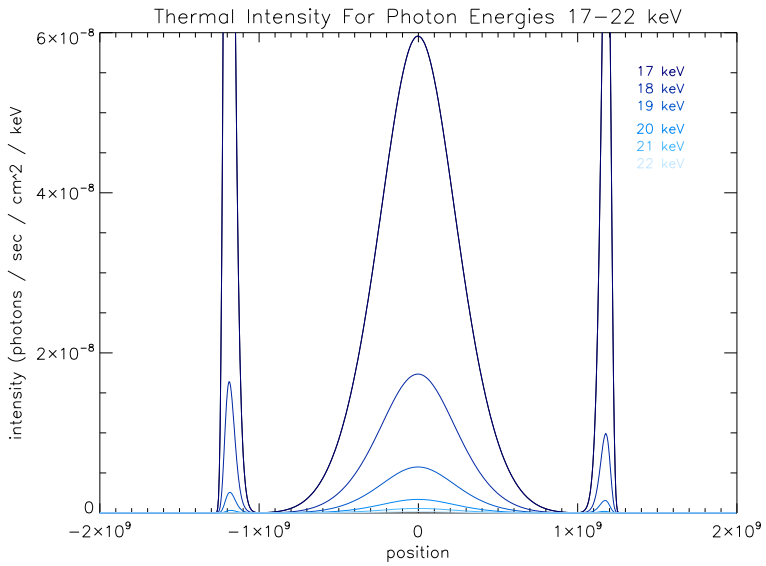

Figure 5.5: Thermal emission (averaged over 100 sec) for various photon energies resulting from the temperature distribution shown in Figure 5.2.

sphere. Furthermore, because temperature increase is cumulative, this difference in temperature between the two chromospheric regions propagates through all the later distributions from the point at which it first appears. The small temperature asymmetry develops because in this model, the temperature increases before losses are calculated are very high, resulting in frequent occurrences of saturated heat flux. In sections of the loop where saturated heat flux applies, the temperature decrease is small, but in adjacent areas where conduction applies, the change is large, and the distribution also becomes smoothed out. We show this in Figure 5.7 for a distribution after 1 sec created with the current simulation parameters - it shows the distribution before conduction / saturated heat flux is calculated, and the distribution after. We can see the rough areas with very little temperature change where saturated heat flux applies, and the smoothed areas with lower temperature gradients where conduction is able to smooth out the distribution. These two very different sections of the distribution then result in a skewed distribution for the next calculations of cooling, and hence an asymmetric final temperature distribution. This pronounced peak where saturated heat flux applies is not seen in later distributions (see Figure 4.19) because over time, the temperature across the rest of the loop (away from the apex) continues to increase and the temperature gradients gradually become less, allowing conduction to dominate and smooth the peak.

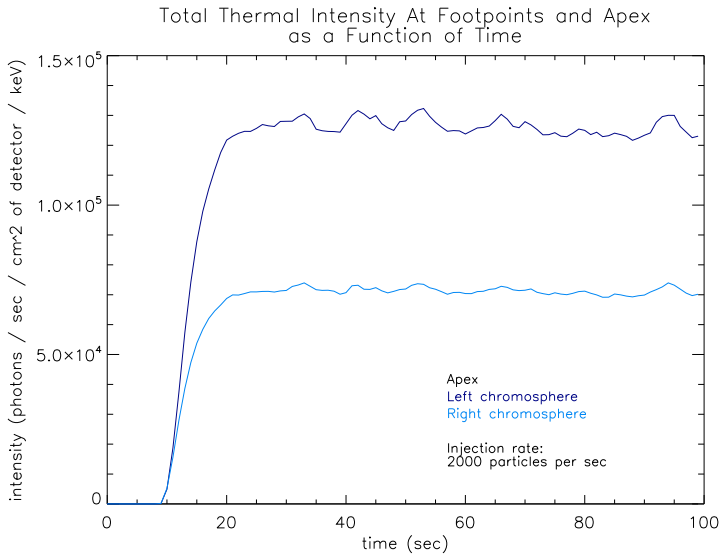

Figure 5.6: Plot of the thermal X-ray intensity at the loop apex and footpoints as a function of time corresponding to Figure 5.4. The emission from the apex is sufficiently small in comparison to the footpoints that it is not visible at this scale.

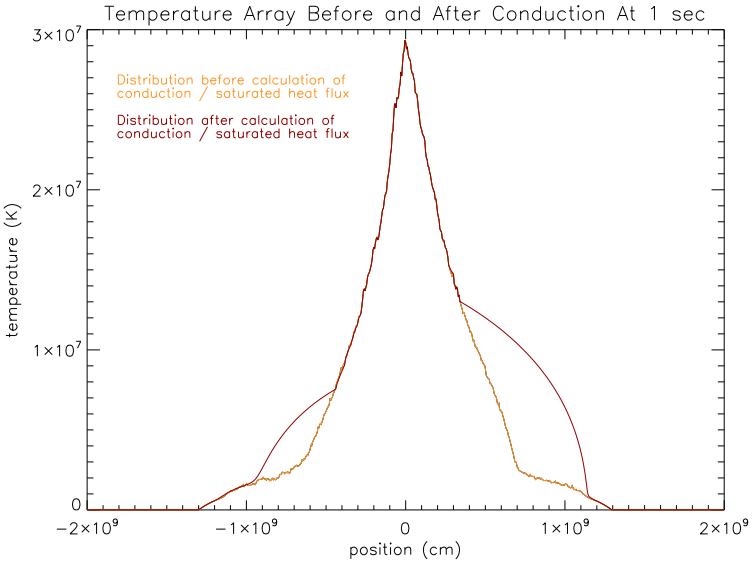

Figure 5.7: Plot of a temperature distribution after 1 sec, before and after the calculation of conduction and saturated heat flux.

In Figures 5.8 and 5.9 we show the non-thermal and thermal X-ray spectra respectively, summed over time, and in Figure 5.10 we show the combined thermal and non-thermal spectrum produced, in a form suitable for comparison with observed spectra (e.g. Figures 1.7 and 5.1).

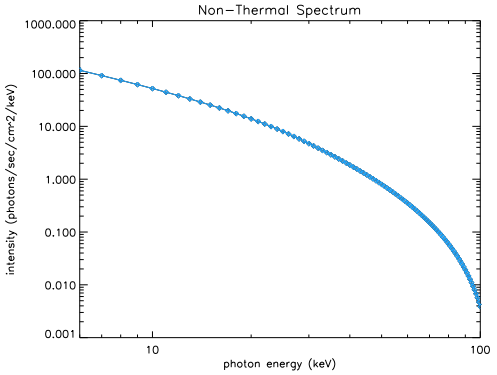

Figure 5.8: Non-thermal X-ray spectrum (summed over time) from a loop with a symmetric magnetic field varying from 100 G (coronal) to 1000 G (photospheric), a coronal density of 10^{10} cm^{-3} and an increased electron flux of 10^{37} electrons s^{-1} cm^{-2}.

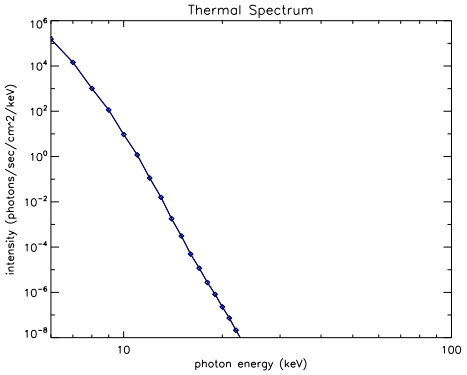

Figure 5.9: Thermal X-ray spectrum (summed over time) corresponding to the temperature distributions shown in Figure 5.2.

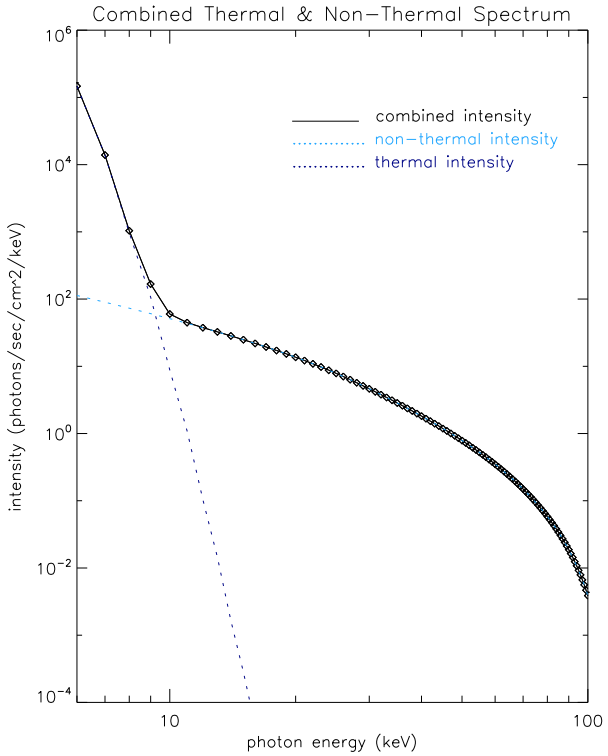

Figure 5.10: Combined thermal and non-thermal X-ray spectrum (over 100 sec) from a loop with a symmetric magnetic field varying from 100 G (coronal) to 1000 G (photospheric), a coronal density of 10^{10} cm^{-3} and an electron flux of 10^{37} electrons s^{-1} cm^{-2}.

We can see that in the observed data (Figures 1.7 and 5.1), the point where the thermal and non-thermal curves intersect is at approximately 20-30 keV in the former and 10-12 keV in the latter - in our results, this point of interception

is at approximately 10 keV, corresponding to Figure 5.1, the weak thermal component event. We can see from Figures 1.7 and 5.1, that the non-thermal part of the spectrum in observations, when extrapolated back, intercepts the y-axis at an intensity of a little over over 100 photons s^{-1} cm^{-2} keV^{-1}, which corresponds with our simulated results, showing that the non-thermal emission produced by our model is representative of a real loop situation. We can also see that the thermal emission from our simulations is of a similar intensity (only slightly lower) to the thermal emission seen in Figure 5.1, an event with a weak thermal component. This is because of the relatively low temperatures produced by our simulations. The thermal X-ray emission we obtain is primarily at low photon energies and originates from the upper chromosphere where the density is high and the temperature is of the order 6 - 7 MK. However, temperatures of this magnitude have been observed at loop footpoints (in the chromospheric regions) (e.g Fletcher & Hudson (2001)). Higher coronal temperatures would result in more emission at higher photon energies and would, if suitably large, allow the looptop source to dominate.

Our results, from the simulations that produced the highest temperatures, appear to concur with observations of events with weak thermal components. It is more common for events to show a higher thermal component (loop temperatures observed are generally higher than we have been able to produce), and thus we must conclude that there are more physical mechanisms contributing to loop heating than those which we include in our model (which considers only collisions between the non-thermal beam electrons and the background particles). Other possible heating mechanisms include chromospheric ablation, resistive heating, inductive heating and shock heating (see Section 1.3.2), all of which would require further development of our existing simulations, including the incorporation of hydrodynamic modelling techniques.

Chapter 6

Radio Emission - Type III Radio Bursts

Radio bursts from the Sun have been observed by various radio observatories from as far back as the 1950s. Type III radio emission is generated when beams of fast electrons propagate through a background plasma and develop a "bump-in-tail" instability (see below), producing Langmuir waves which in turn convert to electromagnetic radiation at radio frequencies. This radio emission is produced in sudden bursts and is often associated with flares and hard X-ray emission. Reverse-drift Type III bursts are so named because of the distinct pattern they produce in radio emission maps (such as Figure 6.1 - steep negative gradient lines) where the frequency of the radio emission increases as time progresses, a reverse of the more commonly observed emission where frequency decreases with time.

6.1 Theory

6.1.1 Production of Radio Bursts

During a solar flare, charged particles (e.g. fast electrons) are accelerated onto magnetic field lines in the solar atmosphere, along which they propagate through the ambient coronal plasma. As they pass through the plasma, they lose energy via Coulomb collisions. The particle energy loss rate is higher for small v ($\frac{dE}{dt} \propto \frac{1}{v}$) and this fact, combined with the velocity dispersion effect, results in a positive slope in the beam velocity space. If the particle distribution initially has a negative slope in velocity space, higher energy (faster) particles propagate along the loop faster than the lower energy particles and result in a "bump" in a plot of the distribution of the electrons which will have a positive slope - this is known

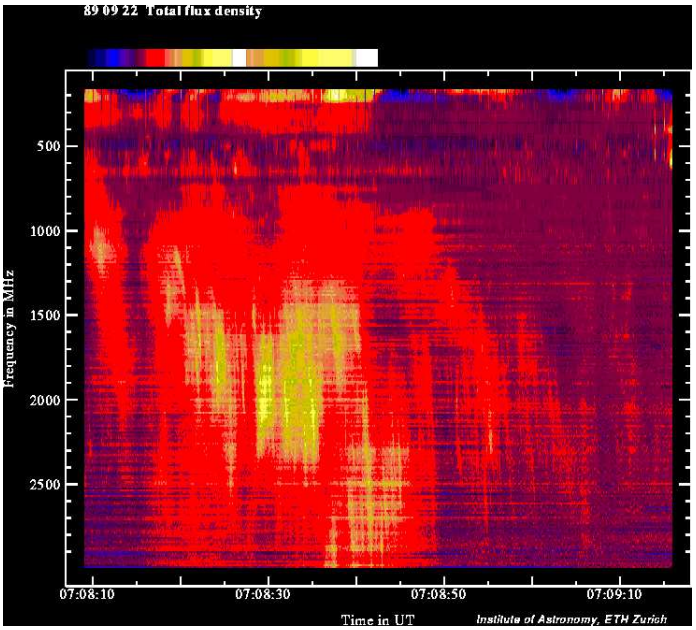

Figure 6.1: Reverse-drift Type-III radio bursts - lines with steep negative gradient and hence increasing frequency with time - for an event on 22nd Sept 1989, from the Phoenix radio spectrometer of ETH Zurich. [ETH Zurich]

as the "bump-in-tail" instability, and makes the electron beam unstable. The unstable beam undergoes Landau resonance, which generates Langmuir waves. These waves can undergo various non-linear wave-wave interactions such as coupling with ion-acoustic waves to produce secondary Langmuir waves, which also interact to provide electromagnetic transverse waves. These interactions produce emission at the electron plasma frequency.

The drift velocity of a Type III burst is related to the initial velocity of the electron beam which produced the bump-in-tail instability. The drift velocity, measured in GHz s^{-1}, is given by:

$$\frac{\mathrm{d}\omega_p}{\mathrm{d}t} = \frac{\mathrm{d}}{\mathrm{d}t}\sqrt{\frac{4\pi e^2 n(s)}{m_e}} \tag{6.1}$$

where ω_p is the plasma frequency and $n(s)$ is the density function. For $s = v_0 t$ (with v_0 the initial velocity of a beam electron) and density function $n(s) = n_0 \mathrm{e}^{\left(\frac{-s}{L}\right)}$ (n_0 being the coronal density and L the density scale height), Equation 6.1 can be written as:

$$\frac{\mathrm{d}\omega_p}{\mathrm{d}t} = \sqrt{\frac{4\pi e^2}{m_e}}\frac{1}{2\sqrt{n(s)}}\frac{-n_0}{L}\mathrm{e}^{\left(\frac{-s}{L}\right)}v_0 \tag{6.2}$$

which relates the drift rate, $\frac{\mathrm{d}\omega_p}{\mathrm{d}t}$ to the initial beam velocity, v_0.

In the following simulations, we use a beam with initial electron velocities ranging from 1×10^{10} cms^{-1} to 1.5×10^{10} cms^{-1}, which can produce Type III bursts with drift rates matching observations (Kontar (2001)). In order to investigate the development of radio emission from such a beam, we choose a point in velocity space at which to look for the first development of a positive slope (the bump-in-tail instability). This positive slope is caused by the beam particles slowing down through collisions and velocity dispersion, and hence the velocity at which this slope appears will be low compared to the particles' initial velocities. In this work, we choose a parallel velocity of $v_s = 2.839 \times 10^9$ cms^{-1} - other velocities of a similar magnitude would also be suitable.

6.1.2 Simulations

Our simulations allow us to record the energy (i.e. velocity), distribution function of a beam of fast electrons by modelling their movements along a magnetic field line in a step-wise manner, including scattering from the ambient plasma, as described in Chapter 2. The distribution function is effectively a histogram of the velocity distribution of the electron beam, which we can plot at various positions along the loop. Such graphs allow us to see where a positive slope in velocity space develops in relation to the required minimum velocity for Type III radio emission (see Section 6.1.1) and hence at what distance along the field line (i.e. at what position in the corona) this emission can first be generated.

We record the velocity distribution of the electrons at a number of positions along the field line. In order to record velocity distributions at specific positions, we approximate each position with a bin of width 10^5 cm, which is small in comparison to the loop length. Use of larger bin widths would mean we were not looking at a velocity distribution at a specific position, however, too small a bin width and there are not enough particles present to make a velocity histogram. We find 10^5 cm to be a suitable compromise between the two extremes.

6.2 Results

In the following results, we show the development of the electron velocity distribution as a function of time and position. We inject the beam electrons in a single burst at $t = 0$ sec at the looptop, with velocities chosen randomly from a

power law distribution between 1×10^{10} cms^{-1} and 1.5×10^{10} cms^{-1}, and pitch angles chosen from a uniform distribution between 0° and 90° to the field in both directions. We look only at the right hand side of the loop, from the apex to the footpoint. For generation of plasma waves and hence Type III radio bursts, we consider the component of velocity of the electrons in the direction of the field line, v_s ($= vcos\theta$, where θ is the pitch angle).

In Figures 6.2 and 6.3, we use a variable density model as described by Equation 2.17, with a coronal value of 10^{10} cm^{-3} and a photospheric value of 10^{16} cm^{-3}, and a field model as shown in Figure 2.11, which varies from 100 G at the loop apex to 1000 G at the photosphere.

Figure 6.2 shows the electron velocity distribution at various positions (indicated by colour) at time $t = 0.05$ sec. Numerical noise produces the oscillations at higher velocities, since fewer particles are at those energies. The vertical dotted line indicates the velocity (energy) corresponding to a wavelength of 10 cm, which is the lower limit on wavelength for Type III radio bursts. We are looking for the time at which a positive slope in the velocity distribution first appears at this energy - this shows us at which position and time the conditions resulting in the production of Type III radio bursts develop. The distributions at a number of positions at 0.05 sec are shown - we can how the distribution differs at different positions. We see higher energy particles at positions further along the loop since faster particles have propagated further in the time elapsed.

Figure 6.3 shows the velocity distribution of electrons at one position at a number of times (indicated by colour). Here, we can easily see where the positive slope first appears at that position - at $\sim t = 0.3$ sec. This shows the development of the distribution over time as the higher energy particles slow down and low energy particles are lost. The pattern of the distribution moves left in velocity space as the particles collectively lose energy, and a positive slope develops at low energies as slower particles are lost.

Using the above data, we can find when the positive slope in velocity space first develops at each position along the loop, and thus show the progression along the loop of the point at which Type III bursts can develop.

Figure 6.4 has a constant magnetic field (100 G) and a constant density (10^9 cm^{-3}) throughout the loop. In this situation, all particles flow directly to the end of the loop with no impediment other than Coulomb collisions with the ambient plasma. We can see that in this case, the development of the positive slope in velocity space (and hence the production of Type III radio bursts) progresses

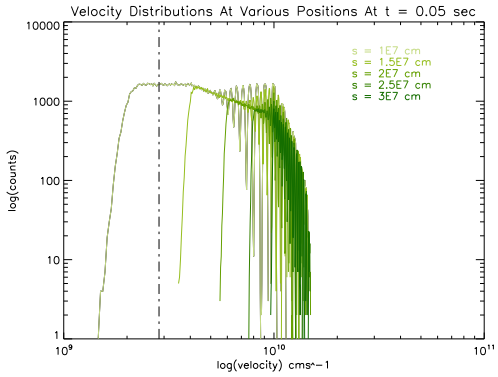

Figure 6.2: Log-log plot of electron velocity distributions for various positions at time t = 0.05 sec. The vertical dotted line indicates the velocity at which we look for a positive slope in velocity space such that Type III radio emission can develop. Density is as described in Equation 2.17, with a coronal density of 10^{10} cm^{-3}), and the field model is as shown in Figure 2.11, varying from 100 G in the corona to 1000 G at the footpoints. All particles are injected at $t = 0$ sec, with initial pitch angles chosen randomly from a uniform distribution between 0° and 180° to the field line, and a power law velocity distribution between 1×10^{10} cms^{-1} and 1.5×10^{10} cms^{-1}.

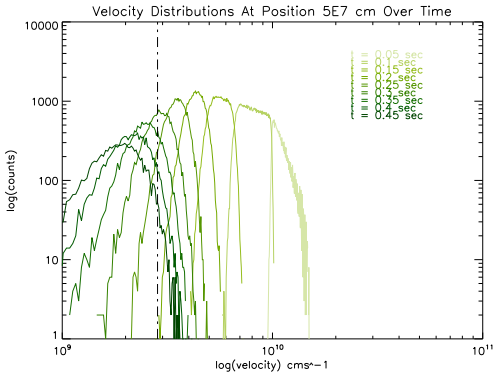

Figure 6.3: Log-log plot of electron velocity distributions for various times at position s = 5 × 10^7 cm. All parameters as in Figure 6.2.

linearly along the length of the loop with time.

In Figure 6.5 we keep a constant magnetic field (100 G) but introduce a variable density model, which is described by Equation 2.17 and increases across the chromosphere from 10^9 - 10^{16} cm^{-3}. In this situation, particles are stopped in the chromosphere by the increasing density. This changes the energy distribution of electrons in the chromosphere. With increased density, there are more collisions and hence more particles are stopped, particularly those at lower energies. Furthermore, a larger number of particles undergo large angle scatterings as a result of the increasing density, causing them to propagate back along the loop - this causes the development of the positive slope in the velocity distribution to propagate more slowly in both the lower corona and chromosphere (compare to Figure 6.6 where we show the same simulation but considering only particles travelling in the positive direction, which shows no slowing of the development of the positive slope in the corona). This results is two points where a positive slope develops concurrently - in the high corona and in the chromosphere. It is the particles with the fastest initial energies that are causing this secondary point of development in the chromopshere - at 0.1 sec, for example, where we see a positive slope at both $\sim 3.7 \times 10^8$ cm and $\sim 1.14 \times 10^9$ cm, the lowest energy particles ($v_i = 1 \times 10^{10}$ cms^{-1}) will have just reached the start of the chromosphere at 1×10^9 cm, and

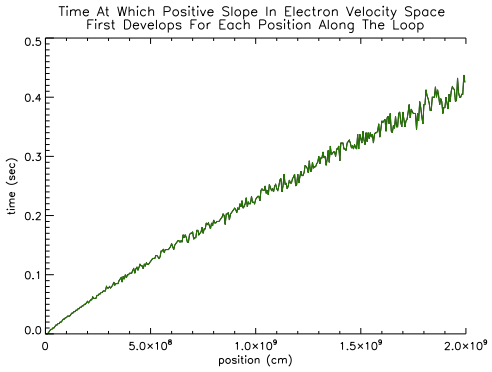

Figure 6.4: Plot of the development of a positive slope in velocity space along a loop as a function of time. Magnetic field and density are both constant everywhere, at 100 G and 10^9 cm^{-3} respectively. All particles are injected at $t = 0$ sec, with initial pitch angles chosen randomly from a uniform distribution between 0° and 180° to the field line, and a power law velocity distribution between 1×10^{10} cms^{-1} and 1.5×10^{10} cms^{-1}.

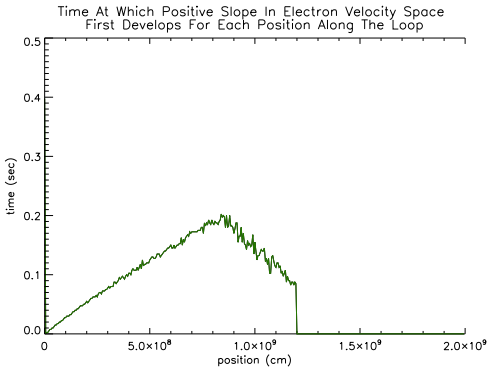

Figure 6.5: As Figure 6.4 but with density varying across the chromosphere (1×10^9 cm to 1.3×10^9 cm) from 10^9 - 10^{16} cm^{-3} according to Equation 2.17.

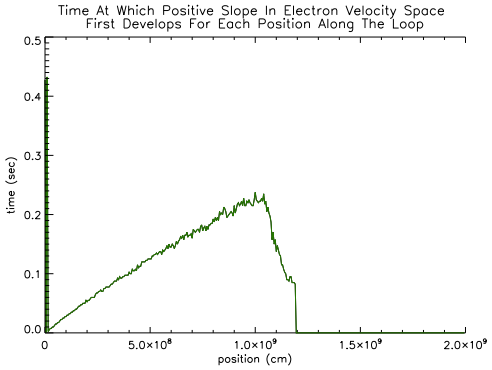

Figure 6.6: As Figure 6.5 but considering only particles travelling in the positive direction.

the highest energy particles ($v_i = 1.5 \times 10^{10}$ cms^{-1}) will have reached well into the chromosphere. In higher regions of the chromosphere, the density is only a few times larger than in the corona, and Type III emission could still originate in this medium - a coronal density of 1×10^9 cm^{-3} results in a wave frequency of ~ 1783 MHz, and a coronal density of 3×10^9 cm^{-3} results in a frequency of ~ 3089 MHz, from the equation for the plasma frequency ($\omega_p = \sqrt{\frac{4\pi n_e e^2}{m_e}}$), which is at the upper limits of Type III emission frequencies.

In Figure 6.7, we introduce a magnetic field which varies from 100 G at the loop apex to 1000 G at the footpoint, as shown in Figure 2.11, and we keep the density model as previously. Now, the majority of particles are reflected by the increasing magnetic field before reaching the chromosphere. In this situation, the

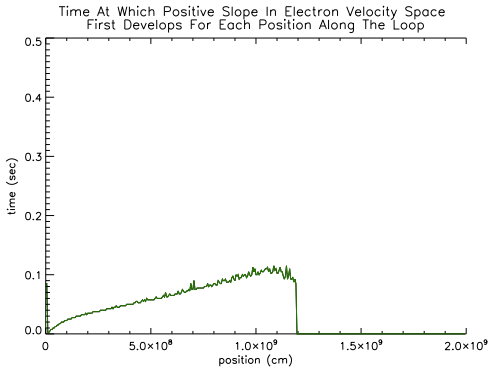

Figure 6.7: As Figure 6.5 but with a magnetic field varying across the loop from 100 G at the apex to 1000 G at the footpoint, as shown in Figure 2.11.

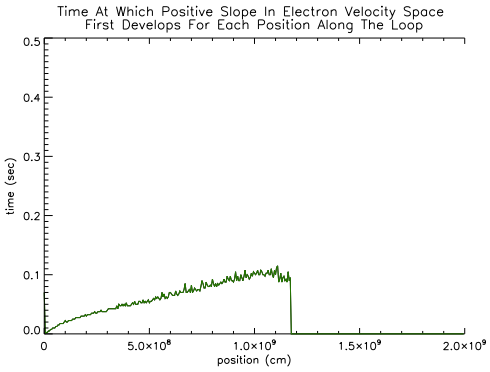

Figure 6.8: As Figure 6.7 but with an increased coronal density of 10^{10} cm^{-3}.

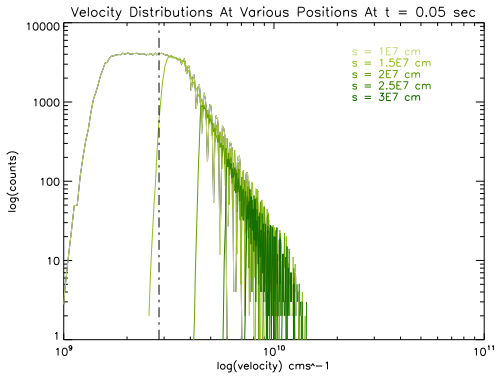

Figure 6.9: As Figure 6.2 but with a velocity distribution between 5×10^9 cms^{-1} and 2×10^{10} cms^{-1}.

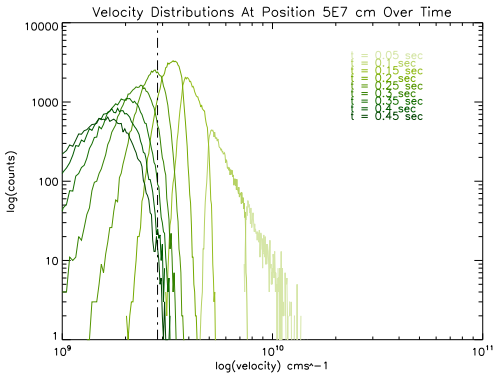

Figure 6.10: As Figure 6.3 but with a velocity distribution between 5×10^9 cms^{-1} and 2×10^{10} cms^{-1}.

condition for production of Type III bursts occurs earlier at each position along the loop than with a constant magnetic field.

Figure 6.8 has the same field and density configuration as previously, but with an increased coronal density of 10^{10} cm^{-3}. This increase in density results in an increase in the number of particles lost, and it causes some particles to be mirrored nearer the looptop than previously. These effects are quite small however, and have little effect on the production of Type III bursts, as we can see from the similarity of Figures 6.7 and 6.8.

In all the above results, the initial velocity (i.e. energy) distribution of the injected particles is a power law ranging from 1×10^{10} cms^{-1} to 1.5×10^{10} cms^{-1}. This is quite a small range of initial energies (approximately 28.4 keV to 64.0 keV). In Figures 6.9, 6.10 and 6.11 we show results with an increased range of initial velocities - 5×10^9 cms^{-1} to 2×10^{10} cms^{-1} ($\sim$ 7.1 keV to 113.7 keV) and other parameters as in Figures 6.2, 6.3 and 6.8.

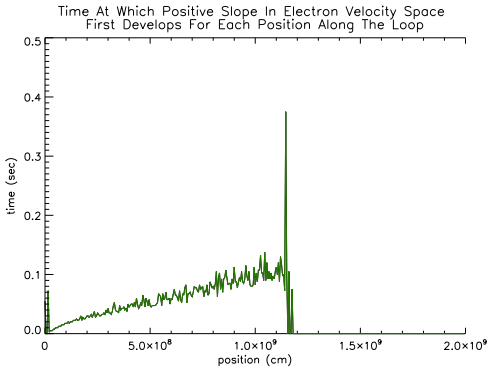

Figure 6.11: As Figure6.8 but with a velocity distribution between 5×10^9 cms^{-1} and 2×10^{10} cms^{-1}.

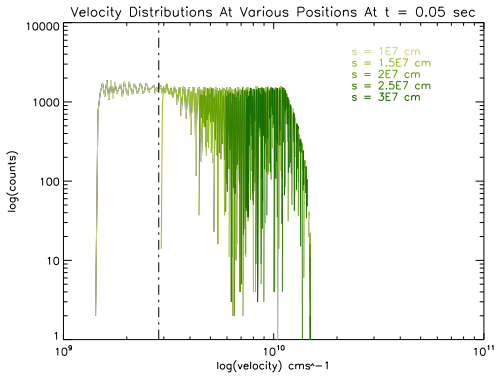

Figure 6.12: As Figure 6.2 but with a higher velocity distribution between 1.5×10^{10} cms^{-1} and 2×10^{10} cms^{-1}.

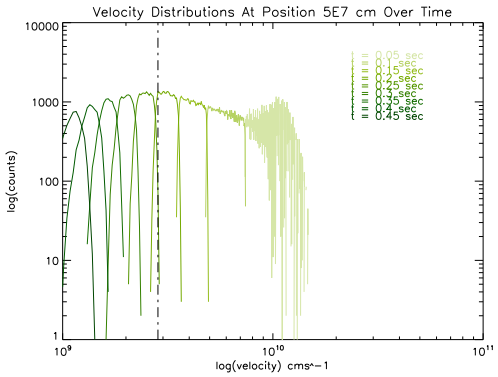

Figure 6.13: As Figure 6.3 but with a higher velocity distribution between 1.5×10^{10} cms^{-1} and 2×10^{10} cms^{-1}.

We can see the difference the larger range of initial velocities has in the velocity distributions as functions of position and time (compare Figures 6.2 and 6.9, and Figures 6.3 and 6.10), however we see little difference between Figure 6.8 and Figure 6.11 other than increased noise because of the wider range of velocities. This shows that this wider range of injected particle velocities does not significantly effect the propagation along the loop of the point where the positive slope (and hence Type III bursts) first develops. This is because the smaller range is centred exactly in the middle of this larger range.

We now show results with an initial velocity distribution shifted upwards in range, so the average particle velocity is higher. We choose the range 1.5×10^{10} cms^{-1} to 2×10^{10} cms^{-1} ($\sim$ 64.0 keV to 113.7 keV). In Figures 6.12, 6.13 and 6.14 we show results with this shifted initial velocity range. In Figure 6.14 we see the propagation of the point where a positive slope in velocity space first develops.

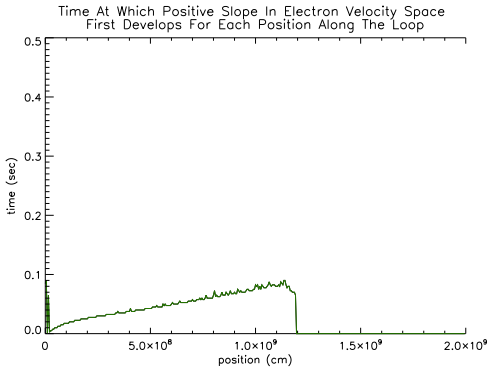

Figure 6.14: As Figure 6.8 but with a higher velocity distribution between 1.5×10^{10} cms^{-1} and 2×10^{10} cms^{-1}.

Because all the particles are at higher energies, the loss rate is lower, and there are less low energy particles to contribute to the positive slope. The converging field and density also have less effect on high energy particles - we can see that in the chromospheric region, where the density increases exponentially, there is little effect on the development of the positive slope as a function of time and position, unlike in earlier models with lower initial particle velocities.

In coronal regions of a loop with constant magnetic field, the location where the beam velocity distribution first becomes positive moves along the loop at a velocity of approximately 4.3×10^9 cms^{-1}. With the addition of a converging magnetic field, this increases to approximately 1×10^{10} cms^{-1} as particles' parallel velocities decrease and some are reflected by the field. In chromospheric regions however, the increasing density causes the point of development of the positive slope to progress more and more slowly along the loop until there are too few particles reaching each position to allow any further development. Shifting the initial velocity distribution such that particles are at higher overall energies to begin with slightly increases the speed along the loop of this point to 1.25×10^{10} cms^{-1}.

In models with a low-energy cut-off of in particle energy of ~ 25 keV or larger (i.e. the models with initial particle energies between 1×10^{10} cms^{-1} and 1.5×10^{10} cms^{-1}, and between 1.5×10^{10} cms^{-1} and 2×10^{10} cms^{-1}), the speed of propagation along the loop of the point where a positive slope first develops is slower than the slowest initial particle velocity, which means that the speed of the point of development of reverse-drift Type III bursts can be used to place a lower limit on the initial beam velocity distribution and hence the injected particle energies.

It also indicates that we would expect reverse-drift Type III radio emission to be delayed with respect to hard X-ray emission, since the beam is propagating faster than the point where a positive slope in velocity space develops. This, however, is not an absolute conclusion, since the development of Type III emission depends strongly on the density of the background plasma, which in our simulations is assumed to be constant in the corona.

In the model with with the widest range of initial particle velocities, 5×10^9 cms^{-1} to 2×10^{10} cms^{-1} ($\sim$ 7.1 keV to 113.0 keV), the point of development of the positive slope travels at approximately 1×10^{10} cms^{-1}, which is this time within the range of initial particle velocities. This is because a large number of the particles in this distribution have very low initial energies (approaching thermal energy levels) and hence are stopped or scattered out of the loop very quickly, leaving mostly high energy particles as in previous higher energy distributions with a low-energy cut-off.

The results we present show the significance of scattering in the development of the positive slope, as well as the effect of velocity dispersion. For example, in Figure 6.10 and similar figures, the broadening of the particle velocity distribution is primarily a result of scattering. Particles undergoing Coulomb collisions lose energy with each collision, and this creates more low energy particles (and hence a positive slope in the velocity distribution) more quickly than velocity dispersion alone would.

Chapter 7

Conclusions & Further Work

In the preceding work, we have examined the effects of a non-relativistic beam of fast electrons propagating along a magnetic field and interacting with the background plasma. The magnetic field represents a magnetic loop in the solar atmosphere. Using stochastic test particle simulations we have modelled the evolution of the electron distribution function over time. Simulations include Coulomb collisions between the beam electrons and the background plasma particles, and use various magnetic field and density models. We have looked at the non-thermal X-ray emission produced by the beam electrons as a function of time, position and X-ray photon energy, investigating the positions in the loop at which non-thermal X-ray emission is produced to find out if these locations concur with observations. We have looked at the heating of the background plasma as a result of collisions between the beam electrons and background particles, including radiative losses, conductive losses and saturated heat flux, showing the evolution of the loop temperature over time. We have investigated thermal X-ray emission produced by this hot plasma, but in most cases the temperatures produced by our simulations have not been high enough to result in this type of emission at RHESSI wavelengths. We then combined the non-thermal and thermal X-ray emission (where high enough) to show the resultant X-ray spectrum in a form comparable to observations produced by the RHESSI satellite in order to compare results from our simulations with the observed data. As an addendum, we have also used our simulations to investigate the production of reverse-drift Type III radio bursts by looking at the development of a positive slope in velocity space of the electrons' energy distribution, which shows us the position and time at which conditions for the generation of reverse-drift Type III bursts first develop.

Our simulations use various field and density model combinations, starting

with basic fields with constant field strength and density in the corona and increasing across the chromosphere to the photosphere, then moving on to models where the field converges gradually throughout the length of the loop (both symmetrically and asymmetrically), a class of field model which includes an X-point field configuration, a topology believed to be representative of magnetic reconnection regions where it is thought particle acceleration occurs. Results from simulations with magnetic fields which converge throughout the loop length, particularly the X-point field model, are most representative of realistic loop parameters. Our density model has constant density throughout the corona and increases exponentially across the chromosphere to reach photospheric values - we use coronal densities from 10^9 cm^{-3} to 10^{12} cm^{-2} and a photospheric density of 10^{16} cm^{-3}.

We consider two types of particle injection onto the loop - instantaneous injection, where all particles are injected at $t = 0$ sec, and continuous injection, where particles are injected at a steady rate of 2000 particles per second for the length of the simulation. We always inject particles at the same position (at the loop apex). Particles are injected with a range of pitch angles with respect to the magnetic field, from 0° to 90°, in both the positive and negative directions. The initial energy (i.e. velocity) distribution of the particles is of a power-law form, ranging from 1×10^{10} cms^{-1} to 2×10^{10} cms^{-1} (non-relativistic).

Our results show non-thermal X-ray emission ranging from approximately 10 to 100 photons sec^{-1} cm^{-2} keV^{-1} depending on the loop model used and, more significantly, the coronal density (Chapter 3). When summed over time and postion to produce X-ray spectra (Chapter 5), these values are of the same order of magnitude as observed by the RHESSI satellite for various flares such as those on the 20th and 23rd July 2002, showing a few hundred to a few thousand photons sec^{-1} cm^{-2} keV^{-1} at the lowest energies, to a few photons sec^{-1} cm^{-2} keV^{-1} at the highest energies. Our results with the more realistic magnetic field models where field strength increases across the loop length show that non-thermal hard X-ray emission is seen at the looptop as well as the footpoints. For higher coronal density models, the looptop peak is larger than the footpoints, and for lower coronal densities, the reverse is generally true. From simulations of a longer time period (100 sec) and with continuous particle injection, we see that the emission from the looptop peaks early then gradually decreases over time, whereas the footpoint emission continues to increase gradually as particles lose energy and precipitate to the footpoints where they are stopped by the increasing

density. We have only presented one simulation covering this larger time period in our study of non-thermal X-ray emission - given more time, it would be useful to study more long timescale simulations with various parameters.

In investigating the temperature increase of the background plasma resulting from Coulomb collisions between the beam electrons and ambient particles, we see lower temperatures than expected from observations. The majority of our results show temperatures not much higher than 2×10^6 K, many less than that. Increasing the density does not result in higher temperatures because particles are lost from the loop more quickly, the energy deposited must be distributed between more particles and the radiative losses are much higher, being proportional to the density squared. Our results show that, when considering only temperature increases from Coulomb collisions, conductive cooling is very efficient at keeping the loop temperature relatively low. When we run longer simulations, for 100 sec, and increase the electron flux in the loop we do see higher temperatures, approaching and slightly exceeding 10^7 K when the coronal density is set to 10^{10} cm^{-3}, but they do not increase any higher than this, even with continuous particle injection. In these situations, the number of particles in the loop reaches a steady-state for a non-X-point field configuration, and actually starts to decrease in the X-point model where particle loss rate is slightly higher. In such situations, the rate of conductive cooling is equivalent (or higher in the case of an X-point field) to the rate of temperature increase, resulting in an unchanging or slightly decreasing temperature profile over time respectively. To increase the temperature further we would need to increase the electron flux further, which pushes us into what would be fairly extreme loop conditions. These results indicate that there are more mechanisms acting to heat the plasma in the loop then Coulomb collisions alone, for example chromospheric evaporation and plasma shocks. To simulate these we would need to combine out simulations with hydrodynamic techniques which allow modelling of bulk plasma motions.

Because the temperature results from our simulations are very low, we do not see thermal X-ray emission from the majority of models we present - this requires temperatures in the range $\sim 1 \times 10^7$ K to 2×10^8 K. The one model which does exceed 10^7 K is the non-X-point field model with a simulation length of 100 sec and an increased electron flux of 10^{37} electrons s^{-1} through the same loop area of 10^{18} cm^2. In this model, we see temperatures approaching 1.06×10^7 K, which results in thermal emission of approximately 2×10^5 photons sec^{-1} cm^{-2} keV^{-1} at 6 keV to 1×10^{-8} photons sec^{-1} cm^{-2} keV^{-1} at about 22 keV. These values are not

as high as observations - they are at the low end of thermal emission. Data from observations shows that our results appear to model the emission from events with weak thermal components, however the majority of events show stronger thermal emission as a result of higher loop temperatures.

In our work on radio emission, we have shown that the evolution of the energy distribution of a beam of fast electrons develops a positive slope in velocity space as the electrons propagate along the magnetic loop. This is produced by a combination of velocity dispersion and the difference in energy loss rates for particles of different energies (the loss rate is higher for lower energy particles). The positions along the loop at which this positive slope appears as time progresses indicates at what point in the loop conditions for the production of reverse-drift Type III radio bursts develop as a function of time, and hence we can gain an insight into the first point of origin of this emission in a loop. As we would expect, increased density slows the propagation of the point where a positive slope develops, since it slows the propagation of the particles though the collisional medium of the background plasma. This can result in two concurrent points in a loop where the slope becomes positive and Type III emission could occur, since the density increases across the chromosphere but is constant in the corona in our models. Results also show that the electron beam propagates faster along the loop than the point of development of the positive slope in velocity space, indicating that the progression of the point of origin of Type III bursts could be used to place a lower limit on the energy of the distribution of electrons which caused them to develop.

In all the work presented here, we use variations on the same model to produce results. To develop this work further, it would be beneficial to first run more simulations with a wider variety of parameters using the existing model, for example with different injection profiles, injection locations, densities and magnetic field configurations. It would be particularly beneficial to run simulations for longer periods of time, since this gives a more complete picture of the processes at work by allowing steady-state situations to develop, and with increased electron flux per unit area, which results in higher temperatures more in line with observations.

We also propose developing time evolving magnetic field models, and extending the simulations to 2D and 3D configurations. When magnetic field lines reform in an X-point configuration, the resultant field line contracts downwards due to magnetic tension, and the particles which were accelerated onto that field line move with it. It would be interesting to model continuous particle injec-

tion onto a series of contracting field lines to observe the emission and heating in two dimensions over time, in particular the effect the contracting field line has on the trapped particles. 3D field configurations could be developed, using information on the field configuration in flaring regions extrapolated from, for example, magnetogram observations by the SOHO satellite. However, field configurations would have to be approximated by a suitably simple mathematical description to allow the simulations to model the movements of particles along them - complex models would result in unfeasibly long computational timescales for the simulations, since the derivative of the field must be calculated numerically for the majority of cases (such as in our X-point field model), and this is a time consuming process.

Moving on to more complex developments, we would recommend extending the model whilst still considering only test particle stochastic simulations, for example by developing particle-in-cell simulations, allowing approximation of bulk plasma effects while still using a test particle model. It would also be useful to investigate the effect of including another diffusion co-efficient, for example, one which would approximate the effects of wave-particle scattering in addition to particle-particle Coulomb scattering. Beyond this, it would be be a more significant project to combine these test particle stochastic simulations with hydrodynamic simulations, which would allow us to model both single particle interaction effects and large scale wave and plasma effects, such as chromospheric ablation and the formation and development of shock waves in the plasma which would, for example, lead to a more complete model of loop heating, an area where our model falls short. It would also allow more detailed study of the development of wave instabilities and Langmuir waves, and hence radio emission.

Bibliography

Aschwanden, M. J. 2002, Particle Acceleration and Kinematics in Solar Flares (Particle Acceleration and Kinematics in Solar Flares, A Synthesis of Recent Observations and Theoretical Concepts, by Markus J. Aschwanden, Lockheed Martin, Advanced technology Center, palo Alto, California, U.S.A. Reprinted from SPACE SCIENCE REVIEWS, Volume 101, Nos. 1-2 Kluwer Academic Publishers, Dordrecht)

Aschwanden, M. J. 2004, Physics of the Solar Corona. An Introduction (Physics of the Solar Corona)

Aschwanden, M. J., Benz, A. O., Dennis, B. R., & Schwartz, R. A. 1995, Astrophysical Journal, 455, 347

Aschwanden, M. J., Benz, A. O., & Schwartz, R. A. 1993, Astrophysical Journal, 417, 790

Bai, T. & Ramaty, R. 1976, Solar Physics, 49, 343

Bai, T. & Ramaty, R. 1979, Astrophysical Journal, 227, 1072

Baumjohann, W. & Treumann, R. A. 1996, Basic space plasma physics (London: Imperial College Press, —c1996)

Benz, A. O. 2002, Plasma Astrophysics: Kinetic Processes in Solar and Stellar Coronae (Kluwer Academic Publishers)

Bornmann, P. L. 1999, in The many faces of the sun: a summary of the results from NASA's Solar Maximum Mission., ed. K. T. Strong, J. L. R. Saba, B. M. Haisch, & J. T. Schmelz, 301–+

Brodrick, D., Tingay, S., & Wieringa, M. 2005, Journal of Geophysical Research (Space Physics), 110, 9

Brown, J. C. 1971, Solar Physics, 18, 485

Brown, J. C. 1973, Solar Physics, 31, 143

Brown, J. C., Emslie, A. G., & Kontar, E. P. 2003, Astrophysical Journal, Letters, 595, L115

Brown, J. C. & Mallik, P. C. V. 2007, ArXiv e-prints, 706

Brown, J. C., S., S. D., & B., M. D. 1979, Astrophysical Journal, 228, 592

Cargill, P. J., Goodrich, C. C., & Vlahos, L. 1988, Astronomy and Astrophysics, 189, 254

Cargill, P. J. & Priest, E. R. 1983, Astrophysical Journal, 266, 383

Carrington, R. C. 1859, Monthly Notices of the Royal Astronomical Society, 20, 13

Chen, F. F. 1984, Introduction to Plasma Physics and Controlled Fusion (Plenum Press)

Cheney, E. W. & Kincaid, D. 2004, Numerical Mathematics and Computing (Thomson, Brooks/Cole)

Christensen-Dalsgaard, J., Gough, D. O., & Thompson, M. J. 1991, Astrophysical Journal, 378, 413

Domingo, V., Fleck, B., & Poland, A. I. 1995, Space Science Reviews, 72, 81

Dulk, G. A. & McLean, D. J. 1978, Solar Physics, 57, 279

Emslie, A. G. 1978, Astrophysical Journal, 224, 241

Emslie, A. G., Dennis, B. R., Holman, G. D., & Hudson, H. S. 2005, Journal of Geophysical Research (Space Physics), 110, 11103

Fisher, G. H., Canfield, R. C., & McClymont, A. N. 1985, Astrophysical Journal, 289, 425

Fletcher, L. 1995, Astronomy and Astrophysics, 303, L9

Fletcher, L. 1997, Astronomy and Astrophysics, 326, 1259

Fletcher, L. 1999, in ESA Special Publication, Vol. 448, Magnetic Fields and Solar Processes, ed. A. Wilson & et al., 693–+

Fletcher, L. & Hudson, H. 2001, Solar Physics, 204, 69

Fletcher, L. & Martens, P. C. H. 1998, Astrophysical Journal, 505, 418

Fletcher, L. & Petkaki, P. 1997, Solar Physics, 172, 267

Fontenla, J. M., Avrett, E. H., & Loeser, R. 1990, Astrophysical Journal, 355, 700

Gabriel, A. H. 1976, Royal Society of London Philosophical Transactions Series A, 281, 339

Gardiner, C. W. 1985, Handbook of Stochastic Methods (Berlin : Springer, c1985)

Gary, G. A. 2001, Solar Physics, 203, 71

Goodman, M. L. 1998, Astrophysical Journal, 503, 938

Hamilton, R. J. & Petrosian, V. 1992, Astrophysical Journal, 398, 350

Handy, B. N., Acton, L. W., Kankelborg, C. C., et al. 1999, Solar Physics, 187, 229

Hey, J. S., Parsons, S. J., & Phillips, J. W. 1948, Monthly Notices of the Royal Astronomical Society, 108, 354

Holman, G. D. 1995, Astrophysical Journal, 452, 451

Holman, G. D. 1996, in Bulletin of the American Astronomical Society, Vol. 28, Bulletin of the American Astronomical Society, 939–+

Holman, G. D., Kundu, M. R., & Kane, S. 1989, in Bulletin of the American Astronomical Society, Vol. 21, Bulletin of the American Astronomical Society, 864–+

Holman, G. D., Sui, L., Schwartz, R. A., & Emslie, A. G. 2003, Astrophysical Journal, Letters, 595, L97

Huba, J. D. 1994, Revised NRL Plasma Formulary (Naval Research Laboratory, Washington DC)

Hurford, G. J., Schmahl, E. J., Schwartz, R. A., et al. 2002, Solar Physics, 210, 61

Ichimoto, K. & Solar-B Team. 2005, Journal of Korean Astronomical Society, 38, 307

Kašparová, J., Karlický, M., Kontar, E. P., Schwartz, R. A., & Dennis, B. R. 2005, Solar Physics, 232, 63

Kel'ner, S. & Skrynnikov, Y. I. 1985, Soviet Astronomy, 29, 445

Kontar, E. P. 2001, Solar Physics, 202, 131

Kovalev, V. A. & Korolev, O. S. 1981, Soviet Astronomy, 25, 215

Lin, R. P., Dennis, B. R., Hurford, G. J., et al. 2002, Solar Physics, 210, 3

Lin, R. P., Levedahl, W. K., Lotko, W., Gurnett, D. A., & Scarf, F. L. 1986, Astrophysical Journal, 308, 954

Lin, R. P., Potter, D. W., Gurnett, D. A., & Scarf, F. L. 1981, Astrophysical Journal, 251, 364

Litvinenko, Y. E. 1996, Astrophysical Journal, 462, 997

Lu, E. T. & Petrosian, V. 1988, Astrophysical Journal, 327, 405

MacKinnon, A. L. & Brown, J. C. 1990, Astronomy and Astrophysics, 232, 544

MacKinnon, A. L. & Craig, I. J. D. 1991, Astronomy and Astrophysics, 251, 693

Manheimer, W. M. & Klein, H. H. 1975, Physics of Fluids, 18, 1299

Masuda, e. a. 1994, Nature, 371, 495

Masuda, S. 2002, in Multi-Wavelength Observations of Coronal Structure and Dynamics, ed. P. C. H. Martens & D. Cauffman, 351–+

Mathew, S. K., Lagg, A., Solanki, S. K., et al. 2003, Astronomy and Astrophysics, 410, 695

Melrose, D. B. 1986, Instabilities In Space & Laboratory Plasmas (Cambridge University Press)

Melrose, D. B. 1995, Astrophysical Journal, 451, 391

Miller, J. A. & Ramaty, R. 1992, in American Institute of Physics Conference Series, Vol. 264, Particle Acceleration in Cosmic Plasmas, ed. G. P. Zank & T. K. Gaisser, 223–228

Ogawara, Y., Takano, T., Kato, T., et al. 1991, Solar Physics, 136, 1

Parker, E. N. 1963, Astrophysical Journal, Supplement, 8, 177

Parks, G. K. 2004, Physics of Space Plasmas (Westview Press)

Petschek, H. E. 1964, in The Physics of Solar Flares, ed. W. N. Hess, 425–+

Piana, M., Massone, A. M., Kontar, E. P., et al. 2003, Astrophysical Journal, Letters, 595, L127

Priest, E. & Forbes, T. 2000, Magnetic Reconnection (Cambridge University Press)

Priest, E. R. & Forbes, T. G. 2002, Astronomy and Astrophysics Reviews, 10, 313

Rosner, R., Tucker, W. H., & Vaiana, G. S. 1978, Astrophysical Journal

Sakai, J.-I. 1992, Solar Physics, 140, 99

Sato, J. 2002, in Bulletin of the American Astronomical Society, Vol. 34, Bulletin of the American Astronomical Society, 757–+

Schmahl, E. J., Pernak, R., & Hurford, G. 2006, 37th American Astronomical Society Solar Physics Devision Meeting Proceedings

Schmelz, J. T. & Brown, J. C., eds. 1992, The Sun: A Laboratory for Astrophysics

Schwarzschild, M. 1959, Astrophysical Journal, 130, 345

Spitzer, L. 1962, The Physics of Fully Ionized Gases (Interscience Publishers, John Wiley & Sons, New York)

Sweet, P. A. 1958, in IAU Symposium, Vol. 6, Electromagnetic Phenomena in Cosmical Physics, ed. B. Lehnert, 123–+

Tandberg-Hanssen, E. & Emslie, G. 1988, The Physics of Solar Flares (Cambridge University Press)

Teriaca, L., Falchi, A., Cauzzi, G., et al. 2003, Astrophysical Journal, 588, 596

Tomczak, M. 2001, Astronomy and Astrophysics, 366, 294

Tsuneta, S. & Naito, T. 1998, Astrophysical Journal, Letters, 495, L67+

Voitenko, Y. M. 1996, Solar Physics, 168, 219

Warren, H. P. & Reeves, K. K. 2001, Astrophysical Journal, Letters, 554, L103

Zaitsev, V. V., Mityakov, M. A., & Rapoport, V. O. 1972, Solar Physics, 24, 444

Zirin, H. 1988, Astrophysics of the Sun (Cambridge University Press)

List of Figures